学位論文

Theoretical predictions of perovskite-type oxyhydrides
based on first-principles calculations

（第一原理計算に基づく
ペロブスカイト型酸水素化物の理論予測）

平成 28 年 12 月博士（理学）申請

東京大学大学院理学系研究科
物理学専攻

佐藤　暢哉

Abstract

Perovskite-type oxides have been widely studied as ferroelectric and piezoelectric compounds. They are expressed in a chemical formula ABO_3, where A and B are metallic atoms. The composition of the A-site and B-site atoms are generally limited for charge neutrality. The dielectric properties are usually controlled by substituting the A and B cations, while substitution for the oxygen anion is also performed. In recent years, substitution of the oxygen anion with the hydrogen anion H^- has become available. Such compounds containing both the oxygen anion and hydrogen anion are referred to as oxyhydrides. Since the valence orbital character of the hydrogen anion is different from that of the oxygen anion, oxyhydrides should exhibit a peculiar electronic structure.

In this thesis, we investigate unsynthesized perovskite-type oxyhydrides $ATiO_2H$ ($A =$ Li, Na, K, Rb, Cs) and their novel electronic structures and dielectric properties by first-principles calculations. We confirm their energetic stabilities in some possible synthesis reactions. Their electronic structures exhibit the two-dimensional states at the top of the valence band, which are formed by in-plane oxygen $2p$ orbital and hydrogen $1s$ orbital. We clarify from a comparison with the electronic structure of $KTiO_2F$ that the origin of the emergent at the valence band maximum (VBM) is low electron affinity of the hydrogen atom. The crystal structures, electronic structures, and dielectric properties for $ATiO_2H$ basically vary with the ionic radii of the A-site atoms.

Furthermore, we analyze the ^1H nuclear magnetic resonance (NMR) chemical shift of $KTiO_2H$. Although the ^1H NMR chemical shift is thought to reflect the charge state of the hydrogen atom, experimentally measured chemical shifts do not describe the difference of the charge state, which does not also for an oxyhydride. In order to examine the phenomenon of the chemical shift in oxyhydrides, we develop the microscopic decompositions of the NMR shielding tensor. We propose decompositions into contributions of Wannier orbitals, energy bands, bunches of bands, and spatial regions. The spatial decomposition overcomes the major problems occurring in other decomposition, and on top of this, we formulate the decomposition into atomic contributions by utilizing the Bader analysis.

Through the analysis for typical hydrides and hydroxides by this decomposition, we find that the shieldings for hydrides are consistent with the conventional view that it is dominated by the charge state of the hydrogen atom, while those for hydroxides are dominated by the contribution from the neighboring oxygen atoms. We also investigate the relation between the chemical shift and interatomic distances by applying the pressure. For the hydroxides, this relation is accidentally consistent with the previously suggested correlation based on the conventional view, although the different origin is proposed from our calculations. For the hydrides, however, the relation is not simple.

The atomic contributions in $KTiO_2H$ reveal that the primary contribution is from the hydrogen atom, which is the same feature as typical hydrides. Meanwhile, the neighboring titanium atoms also have sizable contributions. The pressure dependence exhibits an extreme change, which probably originates from the contribution of the titanium atom. Thus, the shielding of the oxyhydride shows the similar, but not identical feature to hydrides.

Acknowledgments

Contents

Acronyms

AE	all-electron
APW+lo	augmented plane wave + local orbital
BCS	Bardeen–Cooper–Schrieffer
DFPT	density-functional perturbation theory
DFT	density functional theory
DOS	density of states
GGA	generalized gradient approximation
GIPAW	gauge-including projector augmented-wave
LDA	local density approximation
MLWF	maximally-localized Wannier function
MPI	Message Passing Interface
NMR	nuclear magnetic resonance
PAW	projector augmented-wave
PBE	Perdew–Burke–Ernzerhof
PS	pseudo
TMS	tetramethylsilane
VASP	Vienna Ab initio Simulation Package
VBM	valence band maximum

Subscripts and superscripts

ci	clamped-ion
H	Hamiltonian gauge
IC	itinerant circulation
is	internal-strain
LC	local circulation

Chapter 1

Introduction

1.1 Perovskite-type oxides

Perovskite-type oxides are known well as ferroelectric and piezoelectric materials. Their chemical formulae are written as ABO_3, where A and B are metallic atoms. The composition of the A-site and B-site atoms are generally limited for charge neutrality. Since the nominal charge of the oxygen anion is -2, the sum of the nominal charges for A and B cations should be $+6$, e.g. (A^{2+}, B^{4+}), and (A^{3+}, B^{3+}).

The crystal structure of ABO_3 consists of corner-sharing BO_6 octahedra and interstitial A atoms as illustrated in Fig. 1.1. The $A-O$ and $B-O$ bonds are basically ionic. From the geometry of an ideal cubic perovskite-type structure, ionic radii should satisfy $r_A + r_O = \sqrt{2}(r_B + r_O)$, where r_A, r_B, and r_O are ionic radii of the A-site, B-site, and oxygen atoms, respectively. In this sense, the stability of the perovskite-type structure is indicated by

$$t = \frac{r_A + r_O}{\sqrt{2}(r_B + r_O)}, \tag{1.1}$$

which is called the tolerance factor [1]. The perovskite-type structure is generally stable if the tolerance factor is between 0.8 and 1 [2]. The electronic structure of ABO_3 is basically characterized by oxygen $2p$ orbitals in the valence band and d orbitals of the B-site atom in the conduction band.

Some of the perovskite-type oxides exhibit significant ferroelectricity and piezoelectricity. These properties are usually controlled by partially substituting the A-site and B-site atoms such as $(AA')BO_3$ and $A(BB')O_3$. Meanwhile, substitution of the oxygen atom has also been studied for such as $ATaO_2N$ ($A = $ Sr, Ba) [3], $KTiO_2F$ [4, 5], and $PbScO_2F$ [6]. Although the nominal charges of the nitrogen and fluorine anions are different from that of the oxygen anion, the charge neutrality is satisfied in these compounds with unconventional combinations of A and B cations.
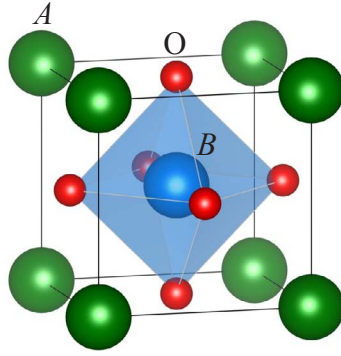
Figure 1.1: Typical crystal structure of the perovskite-type compound $A B O_3$.

1.1.1 Substitution with the fluorine atom in $BaTiO_3$

Substitution of the oxygen atom with the fluorine atom has been performed for perovskite-type oxide $BaTiO_3$ [5, 7]. Strictly speaking, the barium atom is simultaneously substituted with the potassium atom, namely, $x KTiO_2F–(1-x)BaTiO_3$ solid solution is formed. For this compound, the charge neutrality is still satisfied.

From the temperature dependence of its dielectric constant, the ferroelectric phase transition temperature is determined, which decreases with respect to the increasing concentration x. When the barium atom is substituted with an atom which has smaller ionic radius, the cell volume is reduced and the displacement of the titanium atom is suppressed, resulting in the lower transition temperature. However, in the case of substitution with the potassium atom, this explanation is not valid due to larger ionic radius of the potassium atom than that of the barium atom. For $x KTiO_2F–(1-x)BaTiO_3$, the decrease of the transition temperature is explained by the large electronegativity of the fluorine atom: the smaller covalency of the Ti−F bond than the Ti−O bond decreases the ferroelectricity.

1.2 Perovskite-type oxyhydrides

In recent years, substitution of the oxygen atom with the hydrogen atom has become available for perovskite-type oxides. Synthesized compounds are at first non-stoichiometric such as $ATiO_{3-x}H_x$ (A = Ca, Sr, Ba) [8, 9], and later, stoichiometric compounds such as $SrVO_2H$ [10] and $SrCrO_2H$ [11] have been successfully synthesized.

In these compounds, since the hydrogen atoms are at the (oxygen) anion site, they are presumably negatively charged and behave as anions H^-. Such compounds containing both the oxygen and hydrogen anions are called "oxyhydrides." Oxyhydrides have been synthesized and theoretically studied also for non-perovskite-type compounds [12, 13]. Recently, such substitution has been utilized to dope carriers to a

superconductor [14].

In stoichiometric perovskite-type oxyhydrides ABO_2H, the charge neutrality is satisfied similarly to the substitution with the nitrogen and fluorine atoms. The substitution with the hydrogen anion therefore extends the range of exploration for perovskite-type compounds with desirable dielectric properties. Under the constraint that ABO_2H satisfies the charge neutrality, unconventional combinations of A and B cations are realized, e.g. (A^+, B^{4+}) and (A^{2+}, B^{3+}). Although the same is true for substitution with the nitrogen and fluorine atoms, there is a feature unique to substitution with the hydrogen anion. The valence orbital of the hydrogen atom is $1s$, which is different from the $2p$ orbitals of the oxygen atom. Thus, replacement of the orbital character takes place with the substitution, which is markedly different from the case of the nitrogen and fluorine substitution. The replacement of the orbital character should drastically change the electronic structure, and thus, electronic properties also.

1.3 ^{1}H nuclear magnetic resonance

The position of the hydrogen atoms in the previously synthesized non-stoichiometric perovskite-type oxyhydrides has been determined by the neutron diffraction measurements to be the oxygen sites. The position and nominal charge of the hydrogen atom in perovskite-type oxyhydrides suggest that it is an anion. However, it is not verified that the hydrogen atom at the anion site is truly charged negatively. Important thing is that the hydrogen atom is a multivalent atom, which can form H^-, H^0, and H^+ in the condensed matter. In order to verify the charge state, it is necessary to measure it directly.

The ^{1}H nuclear magnetic resonance (^{1}H NMR) spectrum is thought to reflect the charge state of the hydrogen atom. The advantage of the ^{1}H nuclear magnetic resonance (NMR) measurement is that it needs a rather small amount of sample and only a laboratory-scale facility. In the ^{1}H NMR measurement, the external static magnetic field is applied, and consequently, the Zeeman splitting of the nuclear spin takes place in the ^{1}H nuclei. The energy difference between the splited levels is detected as a resonant frequency. Since the energy difference depends on the magnetic field induced at the ^{1}H nuclei as well as the external magnetic field, the resonant frequencies differ between atomic sites or local environments around the nuclei. The peak position, or the resonant point, in the NMR spectrum is called the chemical shift. The chemical shift δ is defined as

$$\delta = \frac{\nu - \nu_{\text{ref}}}{\nu_{\text{ref}}}, \tag{1.2}$$

where ν is the resonant frequency of the nucleus in the sample and ν_{ref} is the reference resonant frequency, and usually written in parts per million (ppm). For the ^{1}H NMR,

the reference is usually taken to be the resonant frequency of the hydrogen atom in $Si(CH_3)_4$ (tetramethylsilane, TMS). The chemical shift can be expressed equivalently by a shielding of the magnetic field. The shielding tensor σ is defined as

$$\sigma_{\alpha\beta} = -\frac{\partial B_\alpha^{\text{ind}}}{\partial B_\beta^{\text{ext}}}, \tag{1.3}$$

where B^{ext} is the external magnetic field and B^{ind} is the magnetic field induced at the nucleus, and then, the chemical shift can be written as

$$\delta = -(\sigma^{\text{iso}} - \sigma_{\text{ref}}^{\text{iso}}), \tag{1.4}$$

where σ^{iso} is the isotropic shielding defined as $\operatorname{tr}\sigma/3$ and $\sigma_{\text{ref}}^{\text{iso}}$ is the isotropic shielding for the reference. This relation shows that the weaker shielding results in the larger chemical shift.

According to the naive picture described below, the chemical shift seems to be positive for H^+ and negative for H^- due to the difference in the number of electrons. The electron induces the magnetic field shielding the external magnetic field at the nucleus, and accordingly, the shielding for H^- is stronger than that for H^+. Since the hydrogen atom in tetramethylsilane (TMS) is positively charged and its shielding is strong among H^+ in various compounds, the chemical shifts could be positive for H^+ and negative for H^-. In reality, however, the hydrogen chemical shifts for hydroxides, where the nominal charge is apparently $+1$, are actually positive in the range of 0–17 ppm [15], while those reported for hydrides, where the nominal charge is apparently -1, are not in the range of 3–9 ppm and not negative [16–18]. Therefore, the relation between the chemical shifts and the hydrogen charge state is not yet well established.

Through some previous studies, empirical correlations between the chemical shift and the atomic distances are suggested. In the case of the molecules, the ^{1}H NMR has been used to determine the position of the hydrogen atom, and there are well-known relations between the positions of the hydrogen atoms and ^{1}H NMR spectra [19]. For solids containing hydroxyls (OH), it has been found that the ^{1}H NMR spectrum is empirically related to the O⋯O distance [15, 20] and the H⋯O distance [15] in a hydrogen bond as shown in Fig. 1.2a. Similarly, for non-metallic hydrides, the correlation with the metal–hydrogen distance is found [21] as shown in Fig. 1.2b. However, the consistent microscopic understanding of the relation is lacking. With this background, prior to investigating the H charge state in oxyhydride, we need to reexamine microscopic mechanism of the NMR shielding phenomenon in typical hydrides and hydroxides.

1.4 Motivation and outline

In this study, we reveal that perovskite-type oxyhydrides are the notable compound group and there are compounds exhibiting novel electronic structures in not yet synthe-
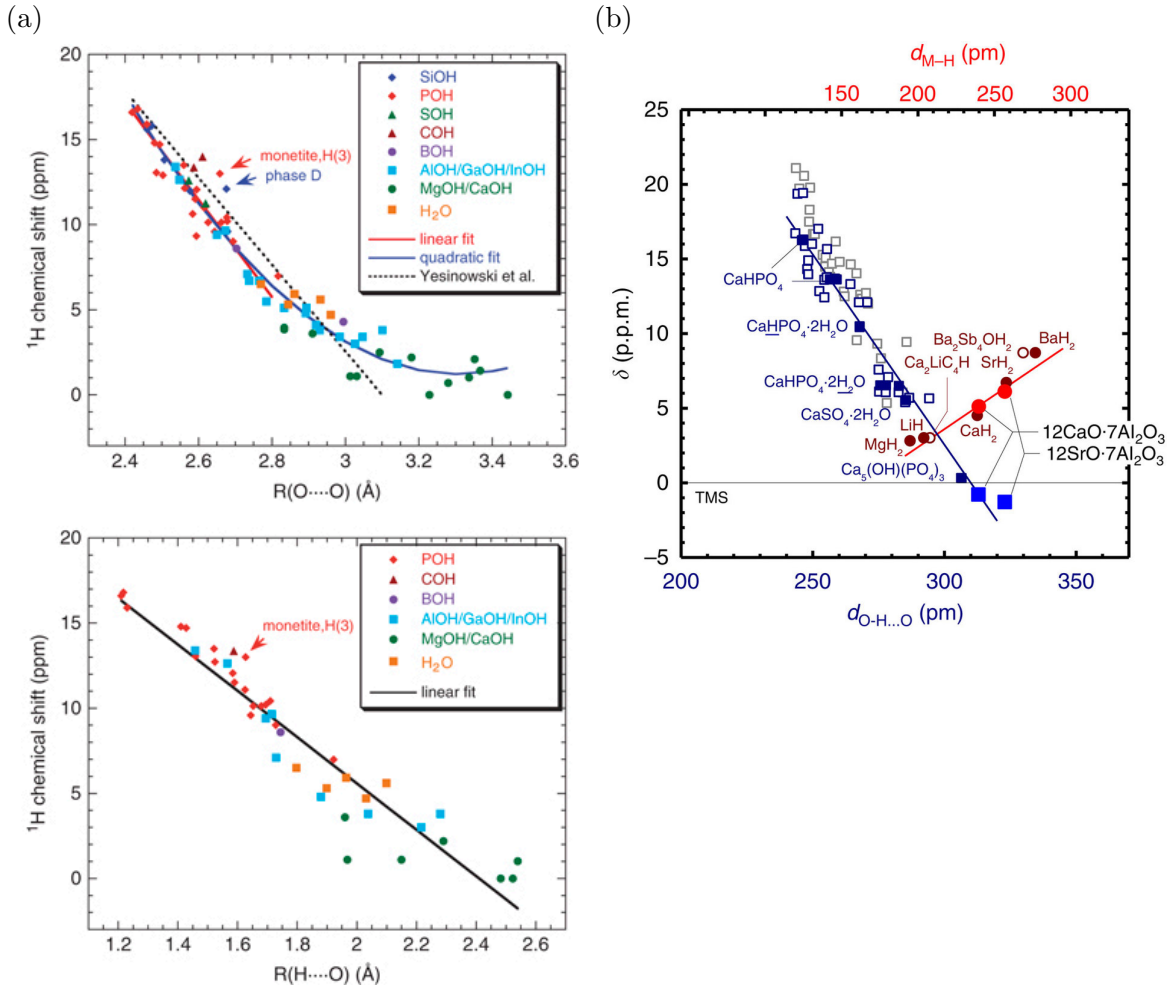
Figure 1.2: Empirical correlations between the ^{1}H NMR chemical shift δ and interatomic distances. (a) Empirical correlations with respect to the oxygen–oxygen distance $R(\mathrm{O}\cdots\mathrm{O})$ and hydrogen–oxygen distance $R(\mathrm{H}\cdots\mathrm{O})$ for (oxy)hydroxides, phosphates, silicates, sulfates, borates, and carbonates [15]. The red line and blue curve are obtained by the linear fitting for data in the range $R(\mathrm{O}\cdots\mathrm{O}) \leq 2.8\,\text{Å}$ and quadratic fitting for all data, respectively. The dashed line is the linear correlation reported in Ref. 20. (b) Empirical correlations with respect to the oxygen–oxygen distance $d_{\mathrm{O-H}\cdots\mathrm{O}}$ and metal–hydrogen distance $d_{M-\mathrm{H}}$ [21]. The blue filled squares, blue open squares, and gray open squares are data for CaO-based compounds, silicate glasses, and solid salts, respectively. The red filled circles are data for binary saline hydrides. The red line is obtained by the linear fitting for hydrides. The dashed line is the linear correlation reported in Ref. 20.

5

sized perovskite-type oxyhydrides. Since the (A^+, B^{4+}) or (A^{2+}, B^{3+}) cation combination in perovskite-type oxyhydrides $AB\mathrm{O}_2\mathrm{H}$ are generally impossible in perovskite-type oxides $AB\mathrm{O}_3$, the exploration of the new perovskite-type oxyhydrides can be regarded as the extension of materials to an unreachable area within oxides. Moreover, by the replacement of the orbital character accompanied by the substitution with the hydrogen atom, there should be perovskite-type oxyhydrides presenting exotic electronic properties. If one supposed that such perovskite-type oxyhydrides are synthesized, their crystal structures, or positions of the hydrogen atoms, should be confirmed. In order to determine the positions of the hydrogen atoms efficiently, the ${}^1\mathrm{H}$ NMR measurement might be useful thanks to its ease of experimenting. It is, however, not easy to determine the position by the chemical shift. To find a way to overcome the difficulty, it is helpful to analyze the chemical shift by decomposing it into physically meaningful contributions.

In order to demonstrate the novelty of perovskite-type oxyhydrides, we investigate alkali metal titanium oxyhydrides $A\mathrm{TiO}_2\mathrm{H}$ ($A = \mathrm{Li}$, Na, K, Rb, Cs). These compounds are not yet synthesized experimentally. Then, to analyze the chemical shift, we develop decomposition methods of the chemical shift. In Chap. 2, we explain the density functional theory and calculation methods based on it. In Chap. 3, we firstly show the results for $\mathrm{KTiO}_2\mathrm{H}$, especially focusing on its novel electronic structure, and comparison with $\mathrm{KTiO}_2\mathrm{F}$ is provided. Subsequently, in Chap. 4, we clarify how the crystal structures, electronic structures, and dielectric properties vary with changing A-site atoms. In Chap. 5, the decomposition methods of the chemical shift are provided. In Chap. 6, we apply these methods to typical hydroxides and hydrides to reveal microscopic mechanism of their shielding. Then, in Chap. 7, we analyze the chemical shift for $\mathrm{KTiO}_2\mathrm{H}$. Finally, we summarize and conclude this study in Chap. 8.

Chapter 2

Theoretical background

In this thesis, we calculate the dielectric properties and shielding tensor based on the density functional theory. We first review the density functional theory, and afterward, we explain the calculation of the dielectric properties and shielding tensor.

2.1 Density functional theory

The Density functional theory (DFT) gives a method to compute the electronic structure of the many-body system from first principles. The foundation of the DFT is the Hohenberg–Kohn theorem [22]. In this theorem, the following many-body Hamiltonian is considered:

$$\mathcal{H} = T + V_{\text{ee}} + V_{\text{en}}, \tag{2.1}$$

where T is the kinetic energy operator, V_{ee} is the electron-electron Coulomb interaction operator, and V_{en} is the electron-nucleus Coulomb interaction operator. The Hohenberg–Kohn theorem states two points. One is that the total energy E is a functional of the electron density $n(\boldsymbol{r})$ as

$$E[n] = F[n] + \langle \Psi[n] | V_{\text{en}} | \Psi[n] \rangle, \tag{2.2}$$

$$F[n] = \langle \Psi[n] | (T + V_{\text{ee}}) | \Psi[n] \rangle, \tag{2.3}$$

where $|\Psi[n]\rangle$ is the many-body wavefunction as a functional of the electron density. The other is the variational principle for the energy functional: $E[n]$ is minimized at the ground state electron density $n_0(\boldsymbol{r})$ and $E[n_0]$ is identical to the energy of the ground state E_0, namely,

$$E_0 = E[n_0] = \min_n E[n]. \tag{2.4}$$

For practical calculations, the Kohn–Sham approach [23] plays an essential role. Starting from the Hohenberg–Kohn theorem, $F[n]$ is divided as

$$F[n] = E_{\text{H}}[n] + T_s[n] + E_{\text{xc}}[n], \tag{2.5}$$

where $E_{\mathrm{H}}[n]$ is the Hartree energy functional defined as

$$E_{\mathrm{H}}[n] = \frac{1}{2} \int d^3r \int d^3r' \frac{n(\boldsymbol{r})n(\boldsymbol{r}')}{|\boldsymbol{r} - \boldsymbol{r}'|}, \tag{2.6}$$

$T_s[n]$ is the kinetic energy functional for non-interacting electrons of the identical electron density $n(\boldsymbol{r})$, and $E_{\mathrm{xc}}[n]$ is the exchange-correlation energy functional. The former two terms $E_{\mathrm{H}}[n]$ and $T_s[n]$ does not contain many-body interactions, and hence, the remaining term $E_{\mathrm{xc}}[n]$ contains all the effects of the many-body interaction. Thanks to the introduction of $T_s[n]$, the minimization of $E[n]$ is achieved by solving the one-body equation

$$\left[-\frac{1}{2}\boldsymbol{\nabla}^2 + v_{\mathrm{H}}(\boldsymbol{r}) + v_{\mathrm{xc}}(\boldsymbol{r}) + v_{\mathrm{ext}}(\boldsymbol{r}) \right] \psi_i(\boldsymbol{r}) = \varepsilon_i \psi_i(\boldsymbol{r}), \tag{2.7}$$

where $v_{\mathrm{H}}(\boldsymbol{r})$ and $v_{\mathrm{xc}}(\boldsymbol{r})$ are the Hartree and exchange-correlation potentials, respectively, defined as

$$v_{\mathrm{H}}(\boldsymbol{r}) = \int d^3r' \frac{n(\boldsymbol{r}')}{|\boldsymbol{r} - \boldsymbol{r}'|}, \tag{2.8}$$

$$v_{\mathrm{xc}}(\boldsymbol{r}) = \frac{\delta E_{\mathrm{xc}}[n]}{\delta n(\boldsymbol{r})}, \tag{2.9}$$

$v_{\mathrm{ext}}(\boldsymbol{r})$ is the nuclear Coulomb potential, and $\psi_i(\boldsymbol{r})$ satisfies

$$n(\boldsymbol{r}) = \sum_i^{\mathrm{occ.}} |\psi_i(\boldsymbol{r})|^2. \tag{2.10}$$

Equation (2.7) is called the Kohn–Sham equation.

In order to solve the Kohn–Sham equation, an explicit form of the exchange-correlation functional should be given. Since the exact form of this functional is not known, approximate functionals are used in practical calculations. The primary approximation is the local density approximation (LDA) [23], which gives the exchange-correlation potential $v_{\mathrm{xc}}(\boldsymbol{r})$ as a function of $n(\boldsymbol{r})$. An extended approximation is also used, which gives the exchange-correlation functional as a function of $n(\boldsymbol{r})$ and its gradient, referred to as the generalized gradient approximation (GGA) [24]. More extended functionals have been also developed.

2.1.1 Projector augmented-wave method

In some density functional calculations, the pseudopotential method is used. In this method, only valence electrons are explicitly treated, and they interact with ions composed of nuclear point charges and core electrons. Although the method gives reliable total energies and lattice parameters, for some physical quantities, it does not have sufficient accuracy. The problem is that the wavefunction is modified to be smooth

around nuclei. The projector augmented-wave (PAW) method [25, 26], which is reviewed in this section, is the method to reconstruct the original wavefunction from the modified smooth one.

We consider to transform the modified pseudo (PS) wavefunction $|\widetilde{\Psi}\rangle$ into the all-electron (AE) wavefunction $|\Psi\rangle$ as $|\Psi\rangle = \mathcal{T}|\widetilde{\Psi}\rangle$. The PS and AE wavefunctions are identical within the interstitial region apart from the atom sites and are different within augmentation regions around atoms:

$$\mathcal{T} = 1 + \sum_{s} \mathcal{T}_s, \tag{2.11}$$

where s is the label for atoms and $\mathcal{T}_s$ acts only within the augmentation region around the atom s. We introduce the AE partial wave $|\phi_{si}\rangle$ from the isolated atom, the PS partial wave $|\widetilde{\phi}_{si}\rangle$ from the relation $|\phi_{si}\rangle = \mathcal{T}|\widetilde{\phi}_{si}\rangle$, and the projector function $|\widetilde{p}_{si}\rangle$ so as to be dual to the PS partial wave. Within the augmentation region around the atom s, the PS and AE wavefunction can be expanded as

$$|\widetilde{\Psi}\rangle = \sum_{i} |\widetilde{\phi}_{si}\rangle \langle \widetilde{p}_{si}|\widetilde{\Psi}\rangle, \tag{2.12}$$

$$|\Psi\rangle = \sum_{i} |\phi_{si}\rangle \langle \widetilde{p}_{si}|\widetilde{\Psi}\rangle. \tag{2.13}$$

Hence, the AE wavefunction can be expressed within the augmentation region as

$$\begin{aligned}
|\Psi\rangle &= |\widetilde{\Psi}\rangle + |\Psi\rangle - |\widetilde{\Psi}\rangle \\
&= |\widetilde{\Psi}\rangle + \sum_{i} (|\phi_{si}\rangle - |\widetilde{\phi}_{si}\rangle) \langle \widetilde{p}_{si}|\widetilde{\Psi}\rangle \\
&= \left[1 + \sum_{i} (|\phi_{si}\rangle - |\widetilde{\phi}_{si}\rangle) \langle \widetilde{p}_{si}| \right] |\widetilde{\Psi}\rangle,
\end{aligned} \tag{2.14}$$

resulting in the PAW transformation

$$\mathcal{T} = 1 + \sum_{s} \sum_{i} (|\phi_{si}\rangle - |\widetilde{\phi}_{si}\rangle) \langle \widetilde{p}_{si}|. \tag{2.15}$$

The expectation value of an operator O with respect to the AE wavefunction can be evaluated as the expectation value of the operator $\mathcal{T}^\dagger O \mathcal{T}$ with respect to the PS wavefunction. If O is a local operator or a semilocal operator such as the kinetic energy term, $\widetilde{O} = \mathcal{T}^\dagger O \mathcal{T}$ can be expressed as

$$\widetilde{O} = O + \sum_{s} \sum_{ij} |\widetilde{p}_{si}\rangle \left(\langle \phi_{si}| O |\phi_{sj}\rangle - \langle \widetilde{\phi}_{si}| O |\widetilde{\phi}_{sj}\rangle \right) \langle \widetilde{p}_{sj}|. \tag{2.16}$$

2.2 Calculation of dielectric properties

The spontaneous electric polarization is the difference of the electric polarization for two crystal structures. The difference of electric polarization $\Delta \boldsymbol{P}$ can be expressed in the sum of the ionic contribution $\Delta \boldsymbol{P}_{\mathrm{ion}}$ and the electronic contribution $\Delta \boldsymbol{P}_{\mathrm{elec}}$ as

$$\Delta \boldsymbol{P} = \Delta \boldsymbol{P}_{\mathrm{ion}} + \Delta \boldsymbol{P}_{\mathrm{elec}}, \tag{2.17a}$$

$$\Delta \boldsymbol{P}_{\mathrm{ion}} = \frac{1}{\Omega} \sum_s Z_s \Delta \boldsymbol{r}_s, \tag{2.17b}$$

$$\Delta \boldsymbol{P}_{\mathrm{elec}} = \boldsymbol{P}_{\mathrm{elec}}^{(\lambda=1)} - \boldsymbol{P}_{\mathrm{elec}}^{(\lambda=0)}, \tag{2.17c}$$

where Ω is the volume of the cell, Z_s is the charge of the ion s, $\Delta \boldsymbol{r}_s$ is the displacement of the ion s, λ is the label of the crystal structure, $\boldsymbol{P}_{\mathrm{elec}}^{(\lambda)}$ is the electric polarization for the crystal structure λ. Although $\boldsymbol{P}_{\mathrm{elec}}^{(\lambda)}$ can be written as

$$\boldsymbol{P}_{\mathrm{elec}}^{(\lambda)} = \frac{1}{\Omega} \int d^3r \, \boldsymbol{r} \rho^{(\lambda)}(\boldsymbol{r}), \tag{2.18}$$

this expression is ill-defined because the absolute position is ill-defined with periodic boundary conditions. In the Berry phase method [27], this problem is overcome by rewriting $\boldsymbol{P}_{\mathrm{elec}}^{(\lambda)}$ in terms of the Berry connection as

$$\boldsymbol{P}_{\mathrm{elec}}^{(\lambda)} = \frac{2i}{(2\pi)^3} \sum_n^{\mathrm{occ.}} \int_{\mathrm{BZ}} d^3k \, \langle u_{n\boldsymbol{k}}^{(\lambda)} | \partial_{\boldsymbol{k}} u_{n\boldsymbol{k}}^{(\lambda)} \rangle, \tag{2.19}$$

where $|u_{n\boldsymbol{k}}^{(\lambda)}\rangle$ is the periodic part of the Bloch orbital. However, $\Delta \boldsymbol{P}_{\mathrm{elec}}$ evaluated in the Berry phase method has an arbitrariness originating from freedom of the phase factor for the wavefunction. If $e^{i\boldsymbol{k}\cdot\boldsymbol{R}_n} |u_{n\boldsymbol{k}}^{(1)}\rangle$ is chosen instead of $|u_{n\boldsymbol{k}}^{(1)}\rangle$, where $\boldsymbol{R}_n$ is the lattice vector, resulting $\Delta \boldsymbol{P}_{\mathrm{elec}}$ get an additional term $2\sum_n^{\mathrm{occ.}} \boldsymbol{R}_n/\Omega$. Therefore, in practical calculations, $\Delta \boldsymbol{P}_{\mathrm{elec}}$ can be evaluated only between structures with sufficiently small difference of the electric polarizations. If the difference between $\boldsymbol{P}_{\mathrm{elec}}^{(0)}$ and $\boldsymbol{P}_{\mathrm{elec}}^{(1)}$ is large, intermediate structures should be prepared so that every difference of the electric polarizations become small.

The Born effective charge tensor Z_s^* for the atom s is defined as

$$Z_{s,\alpha\beta}^* = \Omega \frac{\partial P_\beta}{\partial r_{s,\alpha}}. \tag{2.20}$$

To calculate the Born effective charge tensor, the derivative of $|u_{n\boldsymbol{k}}\rangle$ with respect to $\boldsymbol{r}_s$ is required from Eq. (2.19). It can be obtained in the density-functional perturbation theory (DFPT) [28] in which the derivative is evaluated as the first-order perturbation with respect to the atomic displacement.

The static dielectric tensor ϵ is expressed as

$$\epsilon_{\alpha\beta} = \epsilon_0 \left(\delta_{\alpha\beta} + \frac{\partial P_\alpha}{\partial \mathcal{E}_\beta} \right), \tag{2.21}$$

where ϵ_0 is the permittivity of vacuum and $\boldsymbol{\mathcal{E}}$ is the electric field. The derivative of the second term can be evaluated in the DFPT as well as the case of the Born effective charge tensor. The static dielectric tensor can also be expressed as the sum of two terms referred to as the clamped-ion and internal-strain terms [29]. The clamped-ion term is the contribution under fixed atomic positions, namely, it is the electronic contribution. The remaining term, the internal-strain term, arises from the displacement of atoms.

The piezoelectric stress tensor e is written as

$$e_{\alpha i} = \frac{\partial P_\alpha}{\partial \eta_i}, \tag{2.22}$$

where η is the strain tensor in the Voigt notation and $i = 1, \ldots, 6$ corresponds to xx, yy, zz, yz, xz, and xy, respectively. Again, it can be evaluated in the DFPT [28]. As well as the static dielectric tensor, the piezoelectric stress tensor can be divided into the clamped-ion and internal-strain terms [29, 30].

2.3 Calculation of the shielding tensor

There are two approaches to calculate the shielding tensor, which are the direct and converse approaches. In the direct approach, the higher cutoff energy required due to the magnetic vector potential of the external magnetic field, which is known as the gauge origin problem. For benefits in implementation and a cutoff energy, we develop the decomposition method (see Chap. 5) based on the converse approach. Since the shielding tensor is evaluated from the orbital magnetization within the converse approach, we firstly review the theory of the orbital magnetization, and afterward, we introduce the converse approach.

2.3.1 Orbital magnetization

For a finite system, the orbital magnetization is defined in Rydberg atomic units with Gaussian cgs units as

$$\begin{aligned}
\boldsymbol{M} &= \frac{1}{2cV} \int d^3 r \, \boldsymbol{r} \times \boldsymbol{j}(\boldsymbol{r}) \\
&= -\frac{1}{2cV} \sum_i \langle \phi_i | \, \boldsymbol{r} \times \boldsymbol{v} \, | \phi_i \rangle,
\end{aligned} \tag{2.23}$$

where V is the volume, $\boldsymbol{j}(\boldsymbol{r})$ is the current density, $|\phi_n\rangle$ is the single-electron orbital, and $\boldsymbol{v}$ is the velocity operator. In contrast, for an infinite system with periodic boundary

conditions, it is difficult to evaluate Eq. (2.23) directly because the expectation value of the position operator $\boldsymbol{r}$ is ill-defined for Bloch orbitals. However, in the last dozen years, this difficulty has been overcome by several formulations [31–34]. They are referred to as "the modern theory of orbital magnetization," and expressions for the orbital magnetization result in

$$\boldsymbol{M} = \frac{1}{2c(2\pi)^3} \operatorname{Im} \sum_{mn}^{\text{occ.}} \int_{\text{BZ}} d^3k \, \langle \partial_{\boldsymbol{k}} u_{m\boldsymbol{k}} | \times (\delta_{nm} \mathcal{H}_{\boldsymbol{k}} + E_{nm\boldsymbol{k}} - 2\mu\delta_{nm}) | \partial_{\boldsymbol{k}} u_{n\boldsymbol{k}} \rangle, \quad (2.24)$$

or equivalent ones, where $\mathcal{H}$ is the Hamiltonian, $\mathcal{H}_{\boldsymbol{k}} = e^{-i\boldsymbol{k}\cdot\boldsymbol{r}} \mathcal{H} e^{i\boldsymbol{k}\cdot\boldsymbol{r}}$, $E_{nm\boldsymbol{k}} = \langle u_{n\boldsymbol{k}} | \mathcal{H}_{\boldsymbol{k}} | u_{m\boldsymbol{k}} \rangle$, μ is the chemical potential, and $| u_{n\boldsymbol{k}} \rangle$ is the periodic part of the Bloch orbital. In the rest of this section, we introduce the modern theory of orbital magnetization briefly by following Refs. 32 and 33.

We consider an insulator with zero Chern numbers. We start from a finite system of N_{c} unit cells, and afterwards, take the thermodynamic limit by increasing N_{c}. For the finite system, the orbital magnetization in Eq. (2.23) becomes

$$\boldsymbol{M} = -\frac{1}{2c\Omega N_{\text{c}}} \sum_i \langle \phi_i | \boldsymbol{r} \times \boldsymbol{v} | \phi_i \rangle, \quad (2.25)$$

where Ω is the volume of the unit cell and $| \phi_i \rangle$ is a localized orbital. Then, we divide the system into an interior region and a surface region. Since a localized orbital $| \phi_i \rangle$ in the interior region can be taken to the bulk Wannier orbital $| w_{n\boldsymbol{R}} \rangle$, where $\boldsymbol{R}$ is the lattice vector, the orbital magnetization corresponding to the interior region can be written as

$$\boldsymbol{M}_{\text{LC}} = -\frac{1}{2c\Omega N_{\text{c}}} \sum_n \sum_{\boldsymbol{R}}^{\text{interior}} \langle w_{n\boldsymbol{R}} | (\boldsymbol{r} - \boldsymbol{R}) \times \boldsymbol{v} | w_{n\boldsymbol{R}} \rangle, \quad (2.26)$$

where the subscript "LC" denotes "local circulation" and $\sum_n \langle w_{n\boldsymbol{R}} | \boldsymbol{v} | w_{n\boldsymbol{R}} \rangle = 0$ is used. Using that $| w_{n\boldsymbol{R}} \rangle$ is obtained by translating $| w_{n\boldsymbol{0}} \rangle$, it can be rewritten as

$$\boldsymbol{M}_{\text{LC}} = -\frac{1}{2c\Omega} \sum_n \langle w_{n\boldsymbol{0}} | \boldsymbol{r} \times \boldsymbol{v} | w_{n\boldsymbol{0}} \rangle. \quad (2.27)$$

This is valid even in the thermodynamic limit because the bulk Wannier orbital is used. For the rest of the system, the surface region, the orbital magnetization can be written as

$$\boldsymbol{M}_{\text{IC}} = -\frac{1}{2c\Omega N_{\text{c}}} \sum_i^{\text{surface}} [\langle \phi_i | (\boldsymbol{r} - \boldsymbol{r}_i) \times \boldsymbol{v} | \phi_i \rangle + \boldsymbol{r}_i \times \langle \phi_i | \boldsymbol{v} | \phi_i \rangle], \quad (2.28)$$

where the subscript "IC" denotes "itinerant circulation" and $\boldsymbol{r}_i = \langle \phi_i | \boldsymbol{r} | \phi_i \rangle$ is the center of the i-th orbital in the surface region. The first term vanishes in the thermodynamic limit because it includes a relative position, while the second term looks divergent due to an absolute position. However, it is shown in Ref. 33 that the second

term can be expressed by using the bulk Wannier orbital, namely, $\boldsymbol{M}_{\mathrm{IC}}$ is a bulk property in the thermodynamic limit although it is defined as a surface contribution. The expression of $\boldsymbol{M}_{\mathrm{IC}}$ in the bulk Wannier orbital is

$$\boldsymbol{M}_{\mathrm{IC}} = -\frac{1}{2c\Omega} \operatorname{Im} \sum_{mn\boldsymbol{R}} \boldsymbol{R} \times \langle w_{n\boldsymbol{R}}| \, \boldsymbol{r} \, |w_{m\boldsymbol{0}}\rangle \, \langle w_{m\boldsymbol{0}}| \, \mathcal{H} \, |w_{n\boldsymbol{R}}\rangle . \tag{2.29}$$

The total orbital magnetization $\boldsymbol{M} = \boldsymbol{M}_{\mathrm{LC}} + \boldsymbol{M}_{\mathrm{IC}}$ can be expressed in the reciprocal space. Using

$$|w_{n\boldsymbol{R}}\rangle = \frac{\Omega}{(2\pi)^3} \int_{\mathrm{BZ}} d^3k \, e^{i\boldsymbol{k}\cdot(\boldsymbol{r}-\boldsymbol{R})} \, |u_{n\boldsymbol{k}}\rangle , \tag{2.30}$$

$$(\boldsymbol{r} - \boldsymbol{R}) |w_{n\boldsymbol{R}}\rangle = i\frac{\Omega}{(2\pi)^3} \int_{\mathrm{BZ}} e^{i\boldsymbol{k}\cdot(\boldsymbol{r}-\boldsymbol{R})} \, |\partial_{\boldsymbol{k}} u_{n\boldsymbol{k}}\rangle , \tag{2.31}$$

Eqs. (2.27) and (2.29) are rewritten as

$$\boldsymbol{M}_{\mathrm{LC}} = \frac{1}{2c\Omega} \operatorname{Im} \sum_{n}^{\mathrm{occ.}} \int_{\mathrm{BZ}} d^3k \, \langle \partial_{\boldsymbol{k}} u_{n\boldsymbol{k}}| \times \mathcal{H}_{\boldsymbol{k}} \, |\partial_{\boldsymbol{k}} u_{n\boldsymbol{k}}\rangle , \tag{2.32a}$$

$$\boldsymbol{M}_{\mathrm{IC}} = \frac{1}{2c\Omega} \operatorname{Im} \sum_{mn}^{\mathrm{occ.}} \int_{\mathrm{BZ}} d^3k \, E_{nm\boldsymbol{k}} \, \langle \partial_{\boldsymbol{k}} u_{m\boldsymbol{k}}| \times |\partial_{\boldsymbol{k}} u_{n\boldsymbol{k}}\rangle . \tag{2.32b}$$

This expression is for the periodic system of an insulator with zero Chern numbers. For a Chern insulator, an additional term is required, and the expression is generalized as Eq. (2.24). This additional term can be written by using Chern numbers (in three dimensions) $\boldsymbol{C}$ as $\mu\boldsymbol{C}/[(2\pi)^2 c]$, therefore it arises only for an insulator with non-zero Chern numbers. The origin of the term is the magnetic field dependence of the number of electrons N_{e}. Although Eq. (2.23) is derived by differentiating the total energy E by the magnetic field, the generalized expression can be obtained by differentiating the grand potential $E - \mu N_{\mathrm{e}}$ [34, 35].

The total orbital magnetization can also be divided into two terms which are individually gauge-invariant [33]. Here "gauge invariance" denotes the invariance under a unitary transformation of the Wannier orbital. We divide Eq. (2.24) into the following two terms:

$$\widetilde{\boldsymbol{M}}_{\mathrm{LC}} = \frac{1}{2c(2\pi)^3} \operatorname{Im} \sum_{mn}^{\mathrm{occ.}} \int_{\mathrm{BZ}} d^3k \, \langle \partial_{\boldsymbol{k}} u_{m\boldsymbol{k}}| \times (\delta_{nm}\mathcal{H}_{\boldsymbol{k}} + \mathcal{P}_{\boldsymbol{k}} E_{nm\boldsymbol{k}} - \mu\delta_{nm}) \, |\partial_{\boldsymbol{k}} u_{n\boldsymbol{k}}\rangle ,$$
$$\tag{2.33a}$$

$$\widetilde{\boldsymbol{M}}_{\mathrm{IC}} = \frac{1}{2c(2\pi)^3} \operatorname{Im} \sum_{mn}^{\mathrm{occ.}} \int_{\mathrm{BZ}} d^3k \, \langle \partial_{\boldsymbol{k}} u_{m\boldsymbol{k}}| \times (E_{nm\boldsymbol{k}} - \mathcal{P}_{\boldsymbol{k}} E_{nm\boldsymbol{k}} - \mu\delta_{nm}) \, |\partial_{\boldsymbol{k}} u_{n\boldsymbol{k}}\rangle , \tag{2.33b}$$

where $\mathcal{P}$ is the projector onto occupied states. The second terms of them compensate each other, resulting in $\boldsymbol{M} = \widetilde{\boldsymbol{M}}_{\mathrm{LC}} + \widetilde{\boldsymbol{M}}_{\mathrm{IC}}$. The second term of $\widetilde{\boldsymbol{M}}_{\mathrm{LC}}$ can be transformed

as

$$\sum_{mn}^{\text{occ.}} \langle \partial_{\boldsymbol{k}} u_{m\boldsymbol{k}} | \times \mathcal{P}_{\boldsymbol{k}} E_{nm\boldsymbol{k}} | \partial_{\boldsymbol{k}} u_{n\boldsymbol{k}} \rangle$$

$$= \sum_{lmn}^{\text{occ.}} \langle \partial_{\boldsymbol{k}} u_{m\boldsymbol{k}} | u_{l\boldsymbol{k}} \rangle \times E_{nm\boldsymbol{k}} \langle u_{l\boldsymbol{k}} | \partial_{\boldsymbol{k}} u_{n\boldsymbol{k}} \rangle$$

$$= - \sum_{lmn}^{\text{occ.}} \langle \partial_{\boldsymbol{k}} u_{l\boldsymbol{k}} | u_{n\boldsymbol{k}} \rangle \times E_{nm\boldsymbol{k}} \langle u_{m\boldsymbol{k}} | \partial_{\boldsymbol{k}} u_{l\boldsymbol{k}} \rangle$$

$$= - \sum_{l}^{\text{occ.}} \langle \partial_{\boldsymbol{k}} u_{l\boldsymbol{k}} | \times \mathcal{P}_{\boldsymbol{k}} \mathcal{H}_{\boldsymbol{k}} \mathcal{P}_{\boldsymbol{k}} | \partial_{\boldsymbol{k}} u_{l\boldsymbol{k}} \rangle , \qquad (2.34)$$

where $\langle u_{l\boldsymbol{k}} | \partial_{\boldsymbol{k}} u_{n\boldsymbol{k}} \rangle = - \langle \partial_{\boldsymbol{k}} u_{l\boldsymbol{k}} | u_{n\boldsymbol{k}} \rangle$ is used. Using $\sum_{n}^{\text{occ.}} \langle \partial_{\boldsymbol{k}} u_{n\boldsymbol{k}} | \times \mathcal{P}_{\boldsymbol{k}} | \partial_{\boldsymbol{k}} u_{n\boldsymbol{k}} \rangle = 0$, $\widetilde{\boldsymbol{M}}_{\text{LC}}$ and $\widetilde{\boldsymbol{M}}_{\text{IC}}$ are transformed as

$$\widetilde{\boldsymbol{M}}_{\text{LC}} = \frac{1}{2c(2\pi)^3} \text{Im} \sum_{n}^{\text{occ.}} \int_{\text{BZ}} d^3k \, \langle \partial_{\boldsymbol{k}} u_{n\boldsymbol{k}} | \times \mathcal{Q}_{\boldsymbol{k}} (\mathcal{H}_{\boldsymbol{k}} - \mu) \mathcal{Q}_{\boldsymbol{k}} | \partial_{\boldsymbol{k}} u_{n\boldsymbol{k}} \rangle$$

$$= \frac{1}{2c(2\pi)^3} \text{Im} \sum_{n}^{\text{occ.}} \int_{\text{BZ}} d^3k \, \langle \widetilde{\partial}_{\boldsymbol{k}} u_{n\boldsymbol{k}} | \times (\mathcal{H}_{\boldsymbol{k}} - \mu) | \widetilde{\partial}_{\boldsymbol{k}} u_{n\boldsymbol{k}} \rangle , \qquad (2.35\text{a})$$

$$\widetilde{\boldsymbol{M}}_{\text{IC}} = \frac{1}{2c(2\pi)^3} \text{Im} \sum_{mn}^{\text{occ.}} \int_{\text{BZ}} d^3k \, \langle \partial_{\boldsymbol{k}} u_{m\boldsymbol{k}} | \times \mathcal{Q}_{\boldsymbol{k}} (E_{nm\boldsymbol{k}} - \mu \delta_{nm}) \mathcal{Q}_{\boldsymbol{k}} | \partial_{\boldsymbol{k}} u_{n\boldsymbol{k}} \rangle$$

$$= \frac{1}{2c(2\pi)^3} \text{Im} \sum_{mn}^{\text{occ.}} \int_{\text{BZ}} d^3k \, \langle \widetilde{\partial}_{\boldsymbol{k}} u_{m\boldsymbol{k}} | \times (E_{nm\boldsymbol{k}} - \mu \delta_{nm}) | \widetilde{\partial}_{\boldsymbol{k}} u_{n\boldsymbol{k}} \rangle , \qquad (2.35\text{b})$$

where $\mathcal{Q}_{\boldsymbol{k}} = 1 - \mathcal{P}_{\boldsymbol{k}}$ and $\widetilde{\partial}_{\boldsymbol{k}}$ is the covariant derivative defined as $\mathcal{Q}_{\boldsymbol{k}} \partial_{\boldsymbol{k}}$. If a unitary transformation is applied to a set of $|u_{n\boldsymbol{k}}\rangle$ at each k, a set of the covariant derivative of $|u_{n\boldsymbol{k}}\rangle$ follows the same unitary transformation. Since $\mathcal{H}_{\boldsymbol{k}}$ and $E_{nm\boldsymbol{k}}$ are transformed accordingly, $\widetilde{\boldsymbol{M}}_{\text{LC}}$ and $\widetilde{\boldsymbol{M}}_{\text{IC}}$ are individually gauge-invariant.

2.3.2 Converse approach to the shielding tensor

For the calculation of the shielding tensor with periodic boundary conditions based on the DFT, there are broadly two approaches. One is referred to as the direct approach [36–38], in which the shielding tensor is evaluated by applying the external magnetic field as in real nuclear magnetic resonance (NMR) measurements. In the direct approach, the current induced by the uniform magnetic field $\boldsymbol{B}^{\text{ext}}$ is calculated, the induced magnetic field $\boldsymbol{B}_s^{\text{ind}}$ at the atom s is evaluated from the induced current, and then, the shielding tensor σ_s for the atom is calculated from its definition as

$$\sigma_{s,\alpha\beta} = - \frac{\partial B_{s,\alpha}^{\text{ind}}}{\partial B_{\beta}^{\text{ext}}}. \qquad (2.36)$$
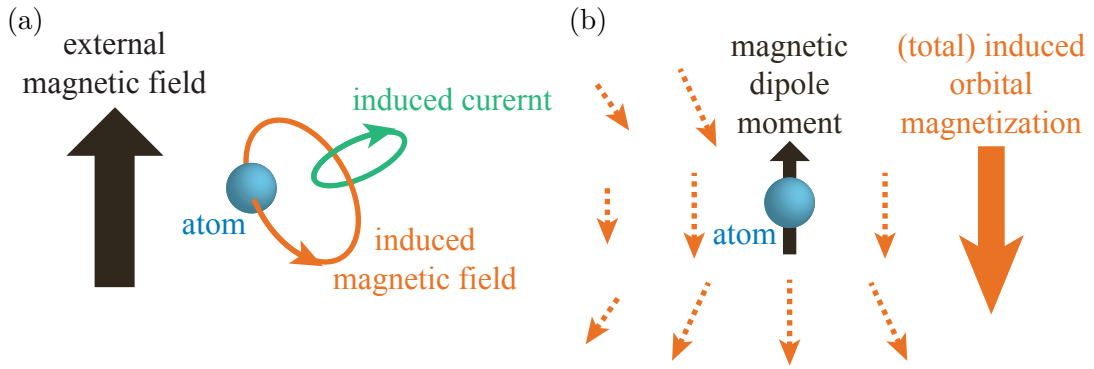
14

Figure 2.1:   Conceptual illustrations for (a) the direct approach and (b) converse approach.

The other approach is referred to as the converse approach [39,40], in which the shielding tensor is evaluated from the induced orbital magnetization $\boldsymbol{M}^{\mathrm{ind}}$ as

$$\sigma_{s,\alpha\beta} = -\Omega \frac{\partial M_\beta^{\mathrm{ind}}}{\partial m_{s,\alpha}},\tag{2.37}$$

where Ω is the volume of the unit cell and $\boldsymbol{m}_s$ is the magnetic dipole moment at the atom s. This approach utilizes the modern theory of orbital magnetization described in the previous section. The conceptual illustrations for these two approaches are shown in Fig. 2.1.

On choosing which approach should be used, there are three points to be considered [40,41]. The first point is ease of implementation. The derivative by the magnetic field in the direct approach is evaluated as a linear response coefficient from its analytical expression, while the derivative by the magnetic dipole moment in the converse approach is evaluated by the numerical differentiation. The numerical differentiation, hence the converse approach, is advantageous in implementation or generalization to methods such as that for relativistic calculations. Note that, in the direct approach, there is a method developed for molecules which uses the numerical differentiation [41]. In only this method, it has the advantage in implementation as well as the converse approach. The second point is the required number of calculations. In the direct approach, shielding tensors for all the atoms in a compound can be evaluated simultaneously. On the contrary, in the converse approach, only one shielding tensor can be evaluated per calculation, and thus, a larger number of calculations are required. It depends on a case whether this point is a crucial disadvantage of the converse approach. If shielding tensors are needed for only several atoms (of a single chemical element) as NMR measurements, only a small number of calculations are required, and it is not much crucial. The third point is the required cutoff energy. The converse approach requires a lower cutoff energy than the direct approach.

We start from deriving Eq. (2.37). Since the total magnetic field at the atom s

is written as $\boldsymbol{B}_s^{\mathrm{tot}} = \boldsymbol{B}^{\mathrm{ext}} + \boldsymbol{B}_s^{\mathrm{ind}}$, the definition of the shielding tensor, Eq. (2.36), is rewritten as

$$\sigma_{s,\alpha\beta} = \delta_{\alpha\beta} - \frac{\partial B_{s,\alpha}^{\mathrm{tot}}}{\partial B_\beta^{\mathrm{ext}}}$$

$$= \delta_{\alpha\beta} + \frac{\partial^2 E}{\partial B_\beta^{\mathrm{ext}} \partial m_{s,\alpha}}, \tag{2.38}$$

where E is the total energy and $B_{s,\alpha}^{\mathrm{tot}} = -\partial E/\partial m_{s,\alpha}$ is used. Using $m_{s,\beta} + \Omega M_\beta^{\mathrm{ind}} = -\partial E/\partial B_\beta^{\mathrm{tot}}$, where Ω is the volume of the cell and $\boldsymbol{B}^{\mathrm{tot}}$ is the macroscopic total magnetic field, it becomes

$$\sigma_{s,\alpha\beta} = \delta_{\alpha\beta} - \sum_\gamma \frac{\partial B_\gamma^{\mathrm{tot}}}{\partial B_\beta^{\mathrm{ext}}} \left(\delta_{\gamma\alpha} + \Omega \frac{\partial M_\gamma^{\mathrm{ind}}}{\partial m_{s,\alpha}} \right). \tag{2.39}$$

The macroscopic total magnetic field $\boldsymbol{B}^{\mathrm{tot}}$ depends on the shape of the macroscopic sample. For the ellipsoidal sample, it can be written as $B_\alpha^{\mathrm{tot}} = B_\alpha^{\mathrm{ext}} + 4\pi(1 - n_\alpha) \sum_\beta \chi_{\alpha\beta} B_\beta^{\mathrm{ext}}$, where χ is the magnetic susceptibility tensor, and n_α are the demagnetizing factor satisfying $\sum_\alpha n_\alpha = 1$. Therefore, the shielding tensor can be written as

$$\sigma_{s,\alpha\beta} = -\Omega \frac{\partial M_\beta^{\mathrm{ind}}}{\partial m_{s,\alpha}} - 4\pi(1 - n_\alpha)\chi_{\alpha\beta}. \tag{2.40}$$

The second term represents the effect of the shape, and evaluated out of the converse approach. The calculation of $\boldsymbol{M}^{\mathrm{ind}}$ is started from the following Hamiltonian with the external magnetic field:

$$\mathcal{H}_{\boldsymbol{B}^{\mathrm{ext}}} = \frac{1}{2} \left[\boldsymbol{p} + \frac{1}{c}\boldsymbol{A}(\boldsymbol{r}) + \frac{1}{c}\boldsymbol{A}_s(\boldsymbol{r}) \right]^2 + V(\boldsymbol{r}), \tag{2.41}$$

where $\boldsymbol{A}(\boldsymbol{r})$ is the magnetic vector potential corresponding to the static external magnetic field $\boldsymbol{B}^{\mathrm{ext}}$ and $\boldsymbol{A}_s(\boldsymbol{r})$ is the magnetic vector potential corresponding to the magnetic dipole moment $\boldsymbol{m}_s$ at the atom s. We use the symmetric gauge for $\boldsymbol{A}(\boldsymbol{r})$ as $\boldsymbol{A}(\boldsymbol{r}) = \boldsymbol{B}^{\mathrm{ext}} \times \boldsymbol{r}/2$. From the Hellmann–Feynman theorem, $\boldsymbol{M}^{\mathrm{ind}}$ can be written as

$$M_\alpha^{\mathrm{ind}} = -\frac{1}{\Omega} \left\langle \left(\frac{\partial \mathcal{H}_{\boldsymbol{B}^{\mathrm{ext}}}}{\partial B_\alpha^{\mathrm{ext}}} \right)_{\boldsymbol{B}^{\mathrm{ext}}=0} \right\rangle, \tag{2.42}$$

where $\langle \cdots \rangle$ denotes the expectation value over occupied Bloch orbitals without the external magnetic field. If this equation is evaluated with the pseudopotential method, the resulting shielding tensor is not accurate because the wavefunction is modified to be smooth around atoms. Therefore, a PAW-like reconstruction is required. In the converse approach, the gauge-including projector augmented-wave (GIPAW) transformation [36] is applied, which is the extension of the PAW transformation. Note that here we use the term "GIPAW" as the name of the transformation, and do not mention

the GIPAW *method* which is a method in the direct approach. The GIPAW transformation takes the phase factor arising from the static magnetic field into account, and the Hamiltonian $\mathcal{H}_{\boldsymbol{B}^{\text{ext}}}$ is transformed into

$$\overline{\mathcal{H}}_{\boldsymbol{B}^{\text{ext}}} = \mathcal{H}_{\boldsymbol{B}^{\text{ext}}} + \sum_s \sum_{ij} a_s(\boldsymbol{r}) |\widetilde{p}_{si}\rangle \, [\, \langle \phi_{si}| \, a_s^\dagger(\boldsymbol{r}) \mathcal{H}_{\boldsymbol{B}^{\text{ext}}} a_s(\boldsymbol{r}) |\phi_{sj}\rangle$$
$$- \langle \widetilde{\phi}_{si}| \, a_s^\dagger(\boldsymbol{r}) \mathcal{H}_{\boldsymbol{B}^{\text{ext}}} a_s(\boldsymbol{r}) |\widetilde{\phi}_{sj}\rangle \,] \, \langle \widetilde{p}_{sj}| \, a_s^\dagger(\boldsymbol{r}), \tag{2.43}$$

where $a_s(\boldsymbol{r}) = e^{i\boldsymbol{r}\cdot(\boldsymbol{r}_s \times \boldsymbol{B}^{\text{ext}})/(2c)}$. Then, $\boldsymbol{M}^{\text{ind}}$ results in

$$\boldsymbol{M}^{\text{ind}} = \boldsymbol{M}_{\text{bare}} + \boldsymbol{M}_{\text{NL}} + \boldsymbol{M}_{\text{para}} + \boldsymbol{M}_{\text{dia}}, \tag{2.44a}$$

$$\boldsymbol{M}_{\text{bare}} = -\frac{1}{2c\Omega} \langle \boldsymbol{r} \times \boldsymbol{v} \rangle, \tag{2.44b}$$

$$\boldsymbol{M}_{\text{NL}} = -\frac{i}{2c\Omega} \left\langle \sum_s (\boldsymbol{r}_s - \boldsymbol{r}) \times [\boldsymbol{r}_s - \boldsymbol{r}, V_s^{\text{NL}}] \right\rangle, \tag{2.44c}$$

$$\boldsymbol{M}_{\text{para}} = -\frac{i}{2c\Omega} \left\langle \sum_s (\boldsymbol{r}_s - \boldsymbol{r}) \times [\boldsymbol{r}_s - \boldsymbol{r}, K_s^{\text{NL}}] \right\rangle, \tag{2.44d}$$

$$\boldsymbol{M}_{\text{dia}} = -\frac{1}{2c} \left\langle \sum_s E_s^{\text{NL}} \right\rangle, \tag{2.44e}$$

where $\boldsymbol{r}_s$ is the position of the atom s, V_s^{NL} is the non-local pseudopotential,

$$\boldsymbol{v} = \frac{1}{i}[\boldsymbol{r}, \overline{\mathcal{H}}_{\boldsymbol{B}^{\text{ext}}}]_{\boldsymbol{B}^{\text{ext}}=\boldsymbol{0}}, \tag{2.45}$$

$$K_s^{\text{NL}} = \frac{1}{2c} \sum_{ij} |\widetilde{p}_{si}\rangle \{ \langle \phi_{si}| \, [\boldsymbol{p} \cdot \boldsymbol{A}_s(\boldsymbol{r}) + \boldsymbol{A}_s(\boldsymbol{r}) \cdot \boldsymbol{p}] \, |\phi_{sj}\rangle$$
$$- \langle \widetilde{\phi}_{si}| \, [\boldsymbol{p} \cdot \boldsymbol{A}_s(\boldsymbol{r}) + \boldsymbol{A}_s(\boldsymbol{r}) \cdot \boldsymbol{p}] \, |\widetilde{\phi}_{sj}\rangle \} \, \langle \widetilde{p}_{sj}|, \tag{2.46}$$

$$E_s^{\text{NL}} = \frac{1}{c} \sum_{ij} |\widetilde{p}_{si}\rangle [\langle \phi_{si}| \, (\boldsymbol{r} - \boldsymbol{r}_s) \times \boldsymbol{A}_s(\boldsymbol{r}) \, |\phi_{sj}\rangle$$
$$- \langle \widetilde{\phi}_{si}| \, (\boldsymbol{r} - \boldsymbol{r}_s) \cdot \boldsymbol{A}_s(\boldsymbol{r}) \, |\widetilde{\phi}_{sj}\rangle] \, \langle \widetilde{p}_{sj}| \tag{2.47}$$

for norm-conserving pseudopotentials. Now $\langle \cdots \rangle$ denotes the expectation value with the PS wavefunction. The first term $\boldsymbol{M}_{\text{bare}}$ can be evaluated by utilizing the modern theory of orbital magnetization described in the previous section. The second to the fourth terms $\boldsymbol{M}_{\text{NL}}$, $\boldsymbol{M}_{\text{para}}$, and $\boldsymbol{M}_{\text{dia}}$ can be evaluated by integrating only within atomic spheres. Finally, the shielding tensor is calculated from Eq. (2.37) by taking numerical differentiation.

Chapter 3

Two-dimensional electronic state in KTiO$_2$H

In this chapter, we propose an unsynthesized perovskite-type oxyhydride KTiO$_2$H from first-principles calculations [42]. This compound is an example of perovskite-type oxyhydrides with chemical compositions $A^+B^{4+}O_2^{2-}H^-$. Since the Shannon ionic radius [43] for the 12-fold coordinated K$^+$ (1.64 Å) is almost the same value as that for the 12-fold coordinated Ba^{2+} (1.61 Å), KTiO$_2$H could be crystallized into the perovskite-type structure as well as BaTiO$_3$. In Sec. 3.1, computational conditions are summarized. In Sec. 3.2, the optimized crystal structure and formation energies for KTiO$_2$H are provided, and bonding characters are discussed. In Sec. 3.3, the electronic structure is provided, which exhibits the two-dimensional state at the valence band maximum (VBM). Detailed analysis for the two-dimensional state is provided in the next section, Sec. 3.4. In the section, the crystal structure and electronic structure for KTiO$_2$F are also provided for comparison.

3.1 Computational details

The calculations are performed by using Vienna Ab initio Simulation Package (VASP) [44, 45]. The projector augmented-wave (PAW) method is used with the Perdew–Burke–Ernzerhof (PBE) [46] parameterization of the generalized gradient approximation (GGA). The numbers of valence electrons in the PAW potentials are 10 ($3s^23p^64s^2$) for K, 12 ($3s^23p^63d^24s^2$) for Ti, 6 ($2s^22p^4$) for O, 7 ($2s^22p^5$) for F, and 1 ($1s^1$) for H. The crystal structures are optimized with a Γ-centered $6 \times 6 \times 6$ k-point grid and the cutoff energies of 800 eV (KTiO$_2$H) and 900 eV (KTiO$_2$F) until all forces on atoms become smaller than 0.01 eV/Å. The electronic structures are calculated with the optimized crystal structures. Used cutoff energies and k-point grids are 800 eV and
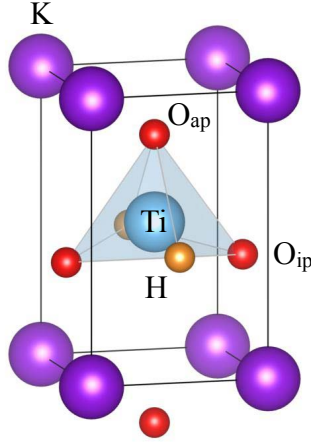
Figure 3.1: Optimized crystal structure for KTiO$_2$H.

a Γ-centered $10 \times 10 \times 6$ grid for KTiO$_2$H, and 900 eV and a Γ-centered $10 \times 8 \times 6$ grid for KTiO$_2$F. To evaluate formation energies, the total energies of K, K$_2$O, KH, TiO$_2$, H$_2$, and H$_2$O are calculated with the following cutoff energies and k-point grids: 520 eV and a Γ-centered $8 \times 8 \times 8$ grid for the primitive cell of bcc K, 800 eV and a Γ-centered $6 \times 6 \times 6$ grid for the primitive cell of antifluorite-type K$_2$O, 520 eV and a Γ-centered $6 \times 6 \times 6$ grid for the primitive cell of rock-salt-type KH, 500 eV and a Γ-centered $4 \times 4 \times 6$ grid for the conventional cell of rutile-type TiO$_2$, 500 eV and the Γ point for H$_2$, and 550 eV and the Γ point for H$_2$O.

3.2 Crystal structure and energetic stability

The optimized crystal structure for KTiO$_2$H is shown in Fig. 3.1, which is orthorhombic $Pmm2$ with lattice parameters $a = 3.51$ Å, $b = 3.75$ Å, and $c = 5.64$ Å. The Wyckoff positions of atoms are $1a$ $(0, 0, z)$ for K, $1d$ $(1/2, 1/2, z)$ for Ti, $1d$ $(1/2, 1/2, z)$ and $1b$ $(0, 1/2, z)$ for O, and $1c$ $(1/2, 0, z)$ for H. Hereafter, the oxygen atoms at the Wyckoff position $1d$ and $1b$ are referred to as the apical oxygen atom O$_{ap}$ and the in-plane oxygen atom O$_{ip}$, respectively. The fractional atomic coordinates are listed in Table 3.1. As clearly seen in Fig. 3.1, the distance between Ti at $z = 0.502$ and O$_{ap}$ at $z = 0.805$ is much smaller than that between Ti at $z = 0.502$ and O$_{ap}$ at $z = 0.805 - 1$, resulting in the 5-fold coordination of Ti atom.

The atomic distance between Ti and O$_{ip}$ is 1.90 Å, which is almost the same as the sum of the Shannon ionic radii [43] for the 5-fold coordinated Ti^{4+} (0.51 Å) and the 6-fold coordinated O^{2-} (1.40 Å). It indicates that the Ti$-$O$_{ip}$ bond is ionic. On the other hand, the atomic distance between Ti and O$_{ap}$, 1.71 Å, is shorter than the sum of the ionic radii. It shows covalent character of the Ti$-$O$_{ap}$ bond. Although an ionic radius is not given for H$^-$ in Ref. 43, it can be estimated by subtracting the Shannon

20

Table 3.1: Fractional atomic coordinates for $KTiO_2H$.

	Wyckoff	x	y	z
K	$1a$	0	0	0
Ti	$1d$	1/2	1/2	0.502
O_{ap}	$1d$	1/2	1/2	0.805
O_{ip}	$1b$	0	1/2	0.375
H	$1c$	1/2	0	0.435

ionic radius for the 5-fold coordinated Ti^{4+} from the atomic distance between Ti and H. The estimated radius of $1.40\,\text{Å}$ corresponds with that used to explain the stability of perovskite-type hydrides [47].

To confirm the energetic stability of the compound, formation energies are evaluated for three possible synthesis reactions

$$K + \frac{1}{2}H_2 + TiO_2 \longrightarrow KTiO_2H, \tag{3.1a}$$

$$\frac{1}{2}K_2O + H_2 + TiO_2 \longrightarrow KTiO_2H + \frac{1}{2}H_2O, \tag{3.1b}$$

$$KH + TiO_2 \longrightarrow KTiO_2H. \tag{3.1c}$$
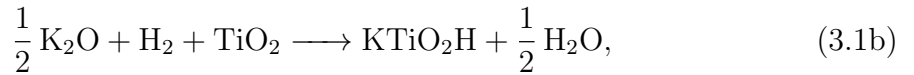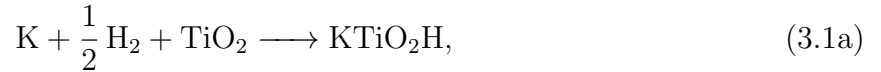
Evaluated formation energies are $-0.67\,\text{eV}$, $-0.36\,\text{eV}$, and $-0.31\,\text{eV}$, respectively. These negative formation energies imply materialization of $KTiO_2H$ by reactions in Eq. (3.1).

3.3 Electronic structure

The total and projected density of states (DOS) are illustrated in Fig. 3.2. The valence band is characterized by primarily O $2p$ orbitals, and the conduction band is characterized by Ti $3d$ orbitals. These characteristics are the same as perovskite-type oxides [48]. At the VBM, the DOS rises up and gradually increase as the energy decreases. This invokes the constant DOS of the two-dimensional system, and actually, as shown in Fig. 3.3, the dispersion of the state at the VBM (along the k-point path Y–T) is extremely small. This two-dimensional state is characterized by O_{ip} $2p_y$ and H $1s$ orbitals. The small dispersion along the k-point path Y–T originates that the path is perpendicular to the O_{ip}−H plane. Although Ti and O_{ap} characters are exhibited in the valence band, they do not contribute to the two-dimensional state, namely, the state completely distributes in the O_{ip}−H plane.
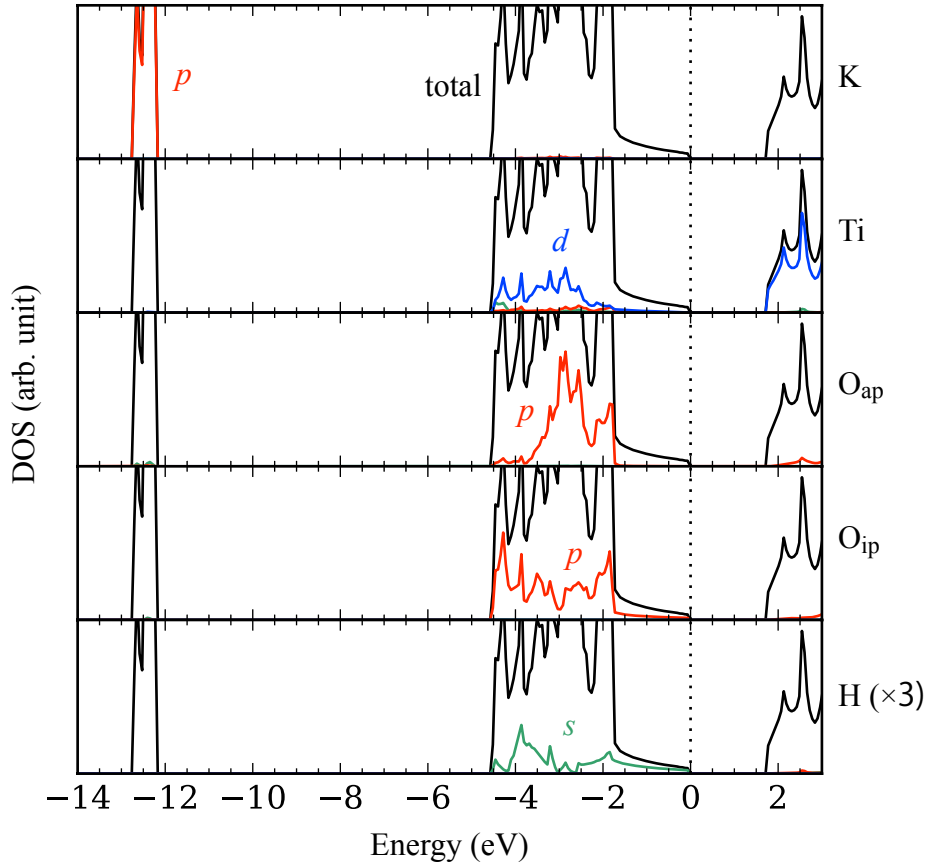
Figure 3.2: Total and projected DOS for KTiO$_2$H. The black lines correspond to the total DOS. The colored lines correspond to the projected DOS onto (green) s, (red) p, and (blue) d orbitals. The projected DOS for H is multiplied by three. The energy is measured from the VBM.

3.4 Origin of the two-dimensional state at the valence band maximum

It may be a crucial factor for the two-dimensionality that the c-axis is stretched. By the c-axis being stretched, the K$-$O$_{ap}$ plane and Ti$-$O$_{ip}-$H plane are spatially separated, resulting in two in-plane states, namely, the O$_{ap}$ state and the O$_{ip}-$H hybridized state. Actually, the O$_{ap}$ state and O$_{ip}-$H hybridized state lie in the different energy regions, the middle of the valence band and entire valence band, respectively, and the narrower energy width for the O$_{ap}$ state can be explained by the longer distance between O$_{ap}$ atoms rather than the distance between O$_{ip}$ and H atoms.

To clarify the effect of substitution with hydrogen on the two-dimensional state, we compare the electronic structure with that for KTiO$_2$F. Since fluorine anions are monovalent anions as well as hydrogen anions, KTiO$_2$F might have crystal structure

(a)

(b)
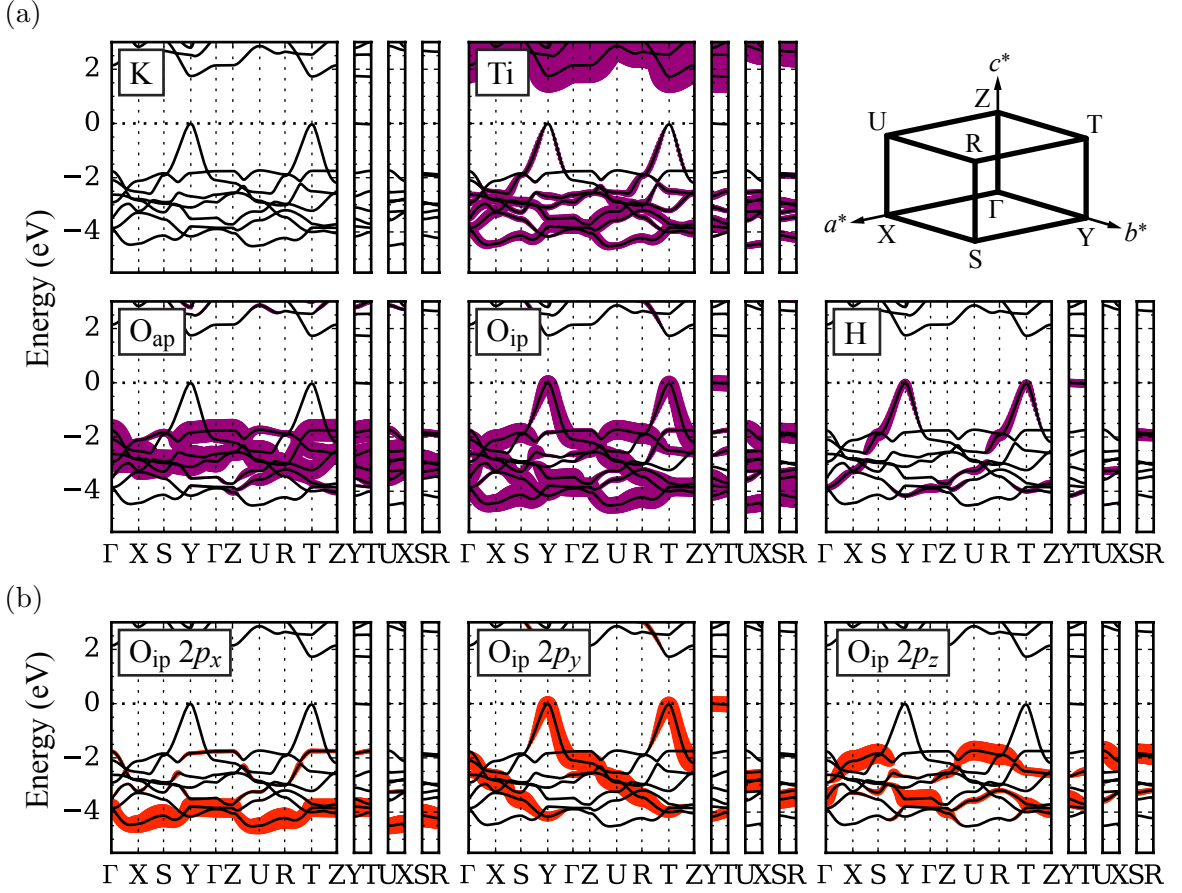
Figure 3.3: Band structure for $KTiO_2H$. Colored lines denote (a) atomic characters and (b) orbital characters for O_{ip}. The energy is measured from the VBM.

and electronic structure similar to $KTiO_2H$. In fact, the optimized crystal structure for $KTiO_2F$ is orthorhombic $Pmm2$ with lattice parameters $a = 3.54\,Å$, $b = 4.05\,Å$, and $c = 5.36\,Å$ and fractional atomic coordinates listed in Table 3.2, which is quite similar to the crystal structure of $KTiO_2H$.

Although the electronic structure is similar to that for $KTiO_2H$ as shown in Fig. 3.4, there are two different point from $KTiO_2H$. Firstly, the two-dimensional state emerges along the different k-point path. For $KTiO_2F$, the two-dimensional state emerges along the k-point path S–R, while it emerges along the path Y–T for $KTiO_2H$. This is natural because the valence orbital character of fluorine atoms is different from that of hydrogen atoms. As seen in Fig. 3.4, the two-dimensional state in $KTiO_2F$ is characterized by $O_{ip}\,2p_y$ and F $2p_x$ states, while that in $KTiO_2H$ is characterized by $O_{ip}\,2p_y$ and H $1s$ states. By considering phase factors of wavefunctions, the two-dimensional states in $KTiO_2H$ and $KTiO_2F$ are illustrated as Fig. 3.5, because the k-point path Y–T means that $(k_x, k_y) = (0, 1/2)$, which corresponds to the phase factor $\exp(i\pi y)$, and the path S–R means that $(k_x, k_y) = (1/2, 1/2)$, which corresponds

23

Table 3.2: Fractional atomic coordinates for $KTiO_2F$.

	Wyckoff	x	y	z
K	$1a$	0	0	0
Ti	$1d$	1/2	1/2	0.502
O_{ap}	$1d$	1/2	1/2	0.821
O_{ip}	$1b$	0	1/2	0.374
F	$1c$	1/2	0	0.443

to the phase factor $\exp(i\pi x)\exp(i\pi y)$. Therefore, the both two-dimensional states in $KTiO_2H$ and $KTiO_2F$ are antibonding states. Secondly, the two-dimensional state in $KTiO_2F$ does not emerge at the VBM. This can be originated from the high electron affinity of fluorine atoms, namely, the two-dimensional state is stabilized by fluorine states. In $KTiO_2H$, in contrast, the much lower electron affinity of hydrogen atoms than fluorine atoms lets the two-dimensional state emerge at the VBM.

The short $Ti-O_{ap}$ bond is also significant for the two-dimensional state to emerge at the VBM. Figure 3.6 shows the band structures for $KTiO_2H$ with artificially lengthened $Ti-O_{ap}$ bonds, where the bond lengths are taken to be about 1.13 and 1.32 times that of the optimized structure. The energy of the O_{ap} state increases as the $Ti-O_{ap}$ bond becomes long, and the two-dimensional state is no longer at the VBM for the bond length by 1.32 times.
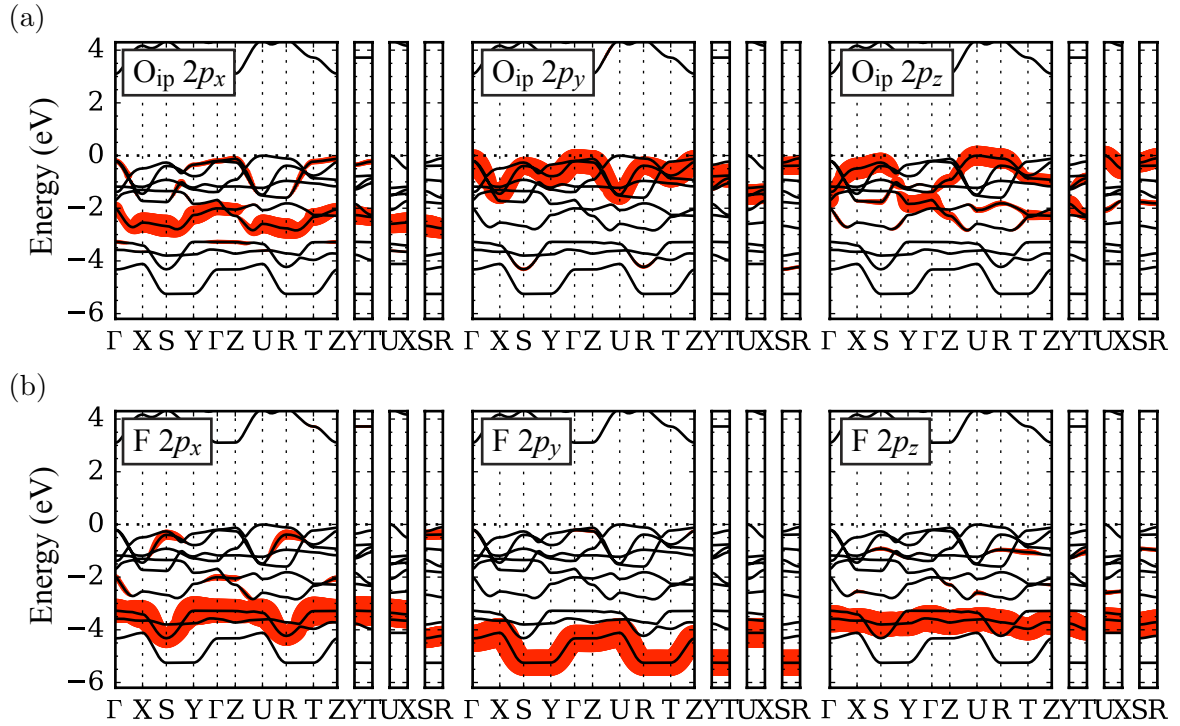
Figure 3.4: Band structure for $KTiO_2F$. Colored lines denote orbital characters for (a) O_{ip} $2p$ and (b) F $2p$ states. The energy is measured from the VBM.
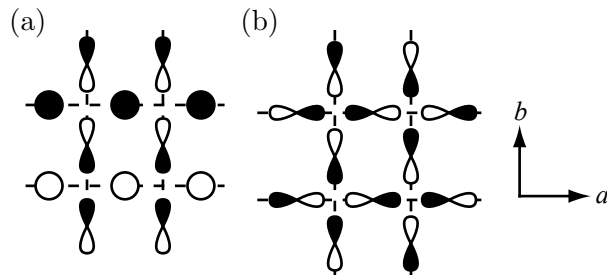
Figure 3.5: Illustrations of the two-dimensional states with phase factors in (a) $KTiO_2H$ and (b) $KTiO_2F$.

(a)   (b)
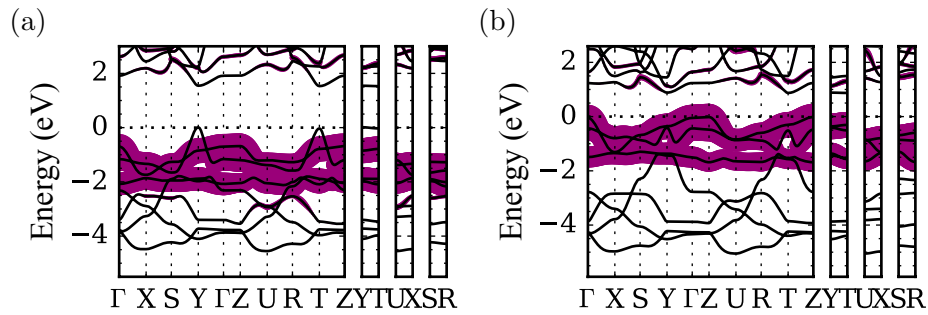
Figure 3.6:   Band structures for KTiO$_2$H with artificially lengthened Ti$-$O$_{ap}$ bonds. The bond lengths are taken to be about (a) 1.13 times and (b) 1.32 times that of the optimized structure. Colored lines denote the atomic character for O$_{ap}$. The energy is measured from the VBM. Note that shown energy ranges are different between figures so that the O$_{ip}-$H states are aligned.

Chapter 4

Alkali metal titanium oxyhydrides: Effect of A-site substitution

In the previous chapter, we reveal the crystal structure and unusual electronic state for $KTiO_2H$. In this chapter, we clarify how the A-site atom affects to them, namely, the crystal structures and electronic structures are compared between alkali metal titanium oxyhydrides $ATiO_2H$ (A = Li, Na, K, Rb, Cs). Moreover, these dielectric properties are evaluated and compared.

4.1 Computational details

The calculations are performed by Vienna Ab initio Simulation Package (VASP) with the projector augmented-wave (PAW) method and the Perdew–Burke–Ernzerhof (PBE) parameterization of the generalized gradient approximation (GGA) as well as in the previous chapter. The numbers of valence electrons are 3 ($1s^2 2s^1$) for Li, 7 ($2p^6 3s^1$) for Na, 9 ($4s^2 4p^6 5s^1$) for Rb, and 9 ($5s^2 5p^6 6s^1$) for Cs. The same potentials are used as in the previous chapter for other atoms, K, Ti, O, and H. The crystal structures are optimized with the cutoff energies of 1000 eV ($LiTiO_2H$) and 800 eV ($NaTiO_2H$, $RbTiO_2H$, and $CsTiO_2H$), and with a Γ-centered $6 \times 6 \times 6$ k-point grid until all forces on atoms become smaller than 0.01 eV/Å. The total energies and electronic structures are calculated with the optimized crystal structures. Used cutoff energies are 1000 eV ($LiTiO_2H$) and 800 eV ($NaTiO_2H$, $RbTiO_2H$, and $CsTiO_2H$), and used k-point grids are a Γ-centered $6 \times 7 \times 6$ grid ($LiTiO_2H$), a Γ-centered $10 \times 10 \times 7$ grid ($NaTiO_2H$), and a Γ-centered $10 \times 10 \times 6$ grid ($RbTiO_2H$ and $CsTiO_2H$). The conditions for $KTiO_2H$ are the same as those in the previous chapter. The dielectric properties are evaluated after the crystal structure optimizations. The cutoff energies used in those calculations are 1000 eV ($LiTiO_2H$) and 800 eV ($NaTiO_2H$, $KTiO_2H$, $RbTiO_2H$,

and CsTiO$_2$H), and the k-point grids are a Γ-point $13 \times 14 \times 11$ grid (LiTiO$_2$H), a Γ-centered $12 \times 12 \times 9$ grid (NaTiO$_2$H), and a Γ-centered $10 \times 10 \times 6$ grid (KTiO$_2$H, RbTiO$_2$H, and CsTiO$_2$H). To evaluate formation energies for LiTiO$_2$H, NaTiO$_2$H, RbTiO$_2$H, and CsTiO$_2$H, the total energies are calculated with the following cutoff energies and k-point grids: 1000 eV and a Γ-centered $6 \times 6 \times 6$ grid (the primitive cell of bcc Li), 520 eV and a Γ-centered $10 \times 10 \times 10$ grid (the primitive cell of bcc Na), 440 eV and a Γ-centered $8 \times 8 \times 8$ grid (the primitive cells of bcc Rb and bcc Cs), 1000 eV and a Γ-centered $6 \times 6 \times 6$ grid (the primitive cell of antifluorite-type Li$_2$O), 800 eV and a Γ-centered $6 \times 6 \times 6$ grid (the primitive cells of antifluorite-type Na$_2$O, antifluorite-type Rb$_2$O, and CdCl$_2$-type Cs$_2$O), 1000 eV and a Γ-centered $6 \times 6 \times 6$ grid (the primitive cell of rock-salt-type LiH), 520 eV and a Γ-centered $6 \times 6 \times 6$ grid (the primitive cell of rock-salt-type NaH), and 500 eV and a Γ-centered $6 \times 6 \times 6$ grid (the primitive cells of rock-salt-type RbH and rock-salt-type CsH). The conditions for TiO$_2$, H$_2$, and H$_2$O are stated in the previous chapter.

The spontaneous electric polarizations are calculated by using the Berry phase method. The procedure is as follows: (i) preparing the crystal structure in which atomic positions are reversed against their centrosymmetric positions, (ii) preparing crystal structures interpolating between this reversed structure and the original structure, (iii) relaxing only lattice parameters for interpolated structures, (iv) evaluating the electric polarizations with the original, reversed, and interpolated structures, and (v) dividing the cumulative difference of these polarizations by two.

The Born effective charge tensors, static dielectric tensors, and piezoelectric stress tensors are calculated based on the density-functional perturbation theory (DFPT). The static dielectric tensor and piezoelectric stress tensor are evaluated by summing up two terms, clamped-ion term and internal-strain term [29, 30]. The clamped-ion term represents the electronic contribution, and the internal-strain term arises from the displacement of atoms. Through this chapter, we use subscripts "ci" and "is" to denote the clamped-ion term and the internal-strain term, respectively.

4.2 Crystal structures and energetic stability

The optimized crystal structures for LiTiO$_2$H, NaTiO$_2$H, RbTiO$_2$H, CsTiO$_2$H are illustrated in Fig. 4.1. As well as KTiO$_2$H (see the previous chapter), their structures are orthorhombic with the space group $Pmm2$, and the Wyckoff positions of atoms are $1a$ $(0, 0, z)$ for A, $1d$ $(1/2, 1/2, z)$ for Ti, $1d$ $(1/2, 1/2, z)$ and $1b$ $(0, 1/2, z)$ for O, and $1c$ $(1/2, 0, z)$ for H. We use the notations O$_{ap}$ and O$_{ip}$ for the oxygen atoms at the Wyckoff position $1d$ and $1b$ in the same manner as the previous chapter. The lattice parameters and fractional atomic coordinates for ATiO$_2$H, including KTiO$_2$H,
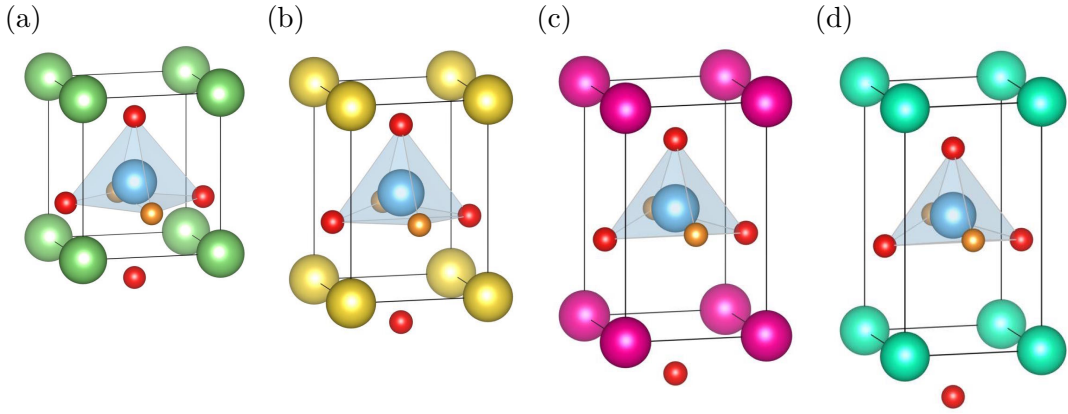
Figure 4.1: Optimized crystal structures for (a) $LiTiO_2H$, (b) $NaTiO_2H$, (c) $RbTiO_2H$, and (d) $CsTiO_2H$.

Table 4.1: Lattice parameters and fractional atomic coordinates for $ATiO_2H$ ($A = Li$, Na, K, Rb, Cs). The atomic coordinates are $(0, 0, z)$ for A, $(1/2, 1/2, z)$ for Ti, $(1/2, 1/2, z)$ for O_{ap}, $(0, 1/2, z)$ for O_{ip}, and $(1/2, 0, z)$ for H.

	$A = Li$	$A = Na$	$A = K$	$A = Rb$	$A = Cs$
a (Å)	3.70	3.54	3.51	3.55	3.56
b (Å)	3.46	3.55	3.75	3.86	3.92
c (Å)	4.24	4.99	5.64	5.79	6.34
A z	0	0	0	0	0
Ti z	0.396	0.483	0.502	0.502	0.503
O_{ap} z	0.802	0.828	0.805	0.797	0.773
O_{ip} z	0.285	0.351	0.375	0.383	0.393
H z	0.267	0.381	0.435	0.446	0.455

are summarized in Table 4.1. As the atomic number of the A-site atom increases, the c-axis becomes longer, while the lengths of the a- and b-axes vary only a little. This trend can be understood from ionic radii of the A-site atoms. As the ionic radius of the A-site atom decreases from Cs to Li, the distance between the TiO_2H layer and the A layer becomes short, namely, the c-axis becomes short. As well as in $KTiO_2H$, Ti atoms are 5-fold coordinated in all the compounds. The atomic distances between Ti and O_{ip} and between Ti and O_{ap} are almost identical to those for $KTiO_2H$ as listed in Table 4.2. It shows that the $Ti-O_{ip}$ bonds are ionic while the $Ti-O_{ap}$ bonds have covalent nature as mentioned in the previous chapter. On the other hand, the atomic distances between Ti and H differ between the compounds. Consequently, the ionic radii of H estimated from the lengths of $Ti-H$ bonds differ, which are 1.30 Å, 1.34 Å, 1.40 Å, 1.45 Å, and 1.47 Å for $A = Li$, Na, K, Rb, Cs, respectively. However, these

Table 4.2:   Atomic distances in Å for ATiO$_2$H ($A =$ Li, Na, K, Rb, Cs).

	$A =$ Li	$A =$ Na	$A =$ K	$A =$ Rb	$A =$ Cs
Ti$-$O$_{ap}$	1.72	1.72	1.71	1.71	1.71
Ti$-$O$_{ip}$	1.91	1.89	1.90	1.90	1.91
Ti$-$H	1.81	1.85	1.91	1.96	1.98

Table 4.3:   Formation energies for synthesis reactions in Eq. (4.1).

	$A =$ Li	$A =$ Na	$A =$ Rb	$A =$ Cs
Eq. (4.1a)	-0.51	-0.52	-0.59	-0.43
Eq. (4.1b)	1.06	0.06	-0.47	-0.19
Eq. (4.1c)	0.35	-0.12	-0.26	-0.11

values are still around 1.40 Å used in Ref. 47.

In order to investigate whether these compounds are energetically stable, we evaluate the formation energies for the following synthesis reactions:

$$A + \frac{1}{2}\,\text{H}_2 + \text{TiO}_2 \longrightarrow A\text{TiO}_2\text{H}, \tag{4.1a}$$

$$\frac{1}{2}\,A_2\text{O} + \text{H}_2 + \text{TiO}_2 \longrightarrow A\text{TiO}_2\text{H} + \frac{1}{2}\,\text{H}_2\text{O}, \tag{4.1b}$$

$$A\text{H} + \text{TiO}_2 \longrightarrow A\text{TiO}_2\text{H}, \tag{4.1c}$$
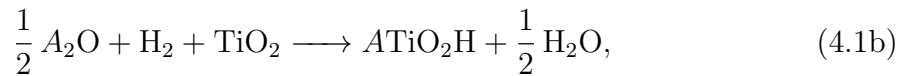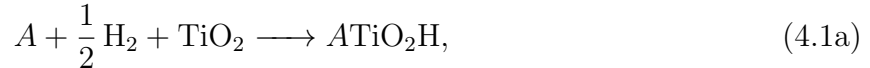
where $A =$ Li, Na, Rb, Cs. For $A =$ K, the stability is already verified in the previous section. For Rb and Cs, all the formation energies are negative as listed in Table 4.3. On the contrary, for Na and Li, the formation energies are positive for some reactions. The synthesis of LiTiO$_2$H and NaTiO$_2$H might be more difficult than the other three compounds.

4.3   Electronic structures

The total and projected density of states (DOS) for ATiO$_2$H ($A =$ Li, Na, Rb, Cs) are illustrated in Fig. 4.2. The nearly constant DOS distributions are exhibited at the valence band maximum (VBM) like KTiO$_2$H. In LiTiO$_2$H, it is exhibited above -0.25 eV. For all $A =$ Li, Na, Rb, Cs, the distributions of the projected DOS in the valence band are quite similar to that for KTiO$_2$H. Additionally, as shown in Fig. 4.3, the band structures for NaTiO$_2$H, RbTiO$_2$H, and CsTiO$_2$H are extremely similar to that for KTiO$_2$H, hence the two-dimensional states at the VBM. For LiTiO$_2$H, however, the state at the VBM is dispersive. The energy of the state in the k-point path U–R is higher clearly for LiTiO$_2$H and slightly for NaTiO$_2$H than those for RbTiO$_2$H and
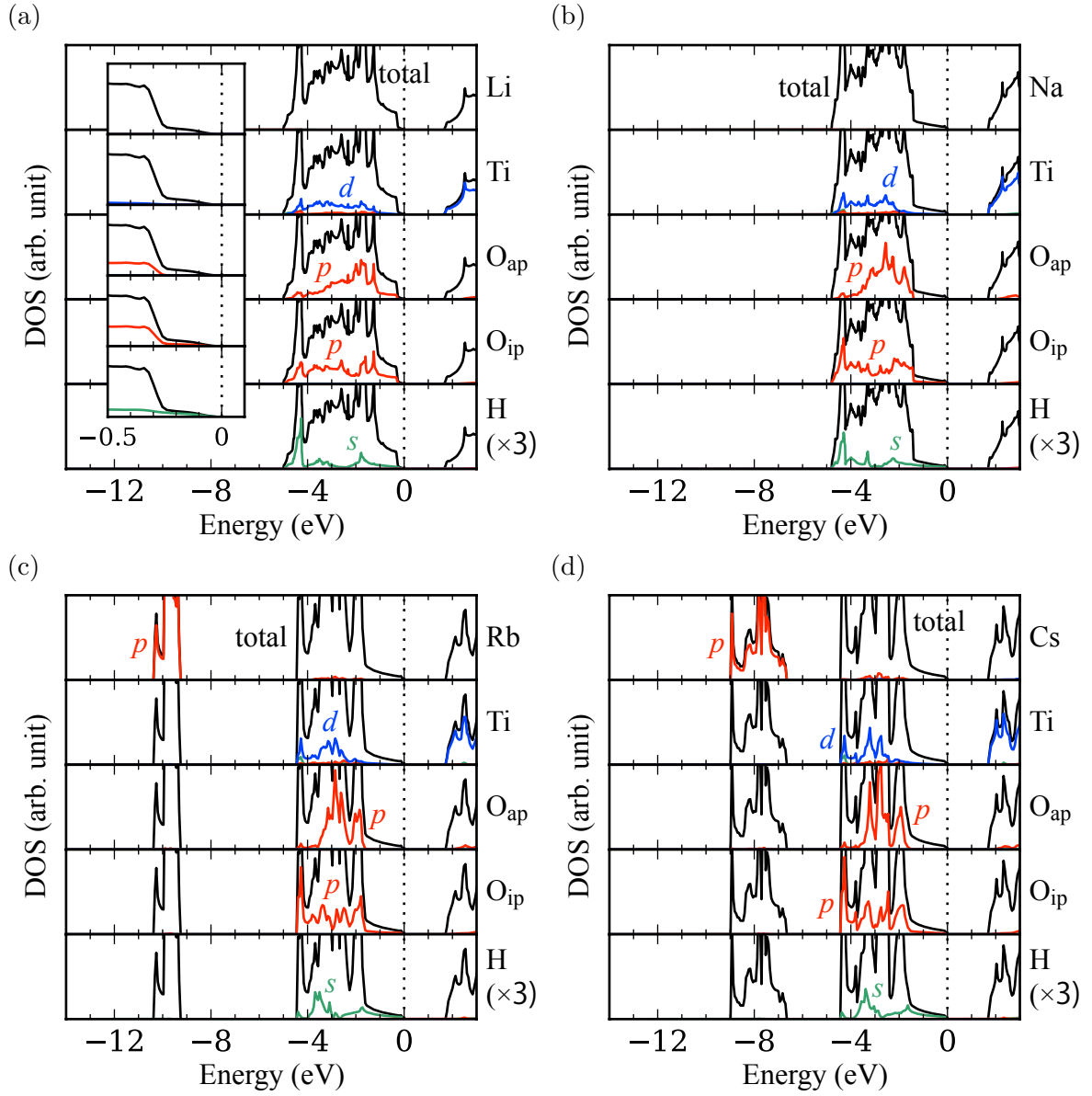
Figure 4.2: Total and projected DOS for (a) LiTiO$_2$H, (b) NaTiO$_2$H, (c) RbTiO$_2$H, and (d) CsTiO$_2$H. The inset of (a) shows the magnified figure around the VBM. The black lines correspond to the total DOS. The colored lines correspond to the projected DOS onto (green) s, (red) p, and (blue) d orbitals. The projected DOS for H is multiplied by three. The energy is measured from the VBM.
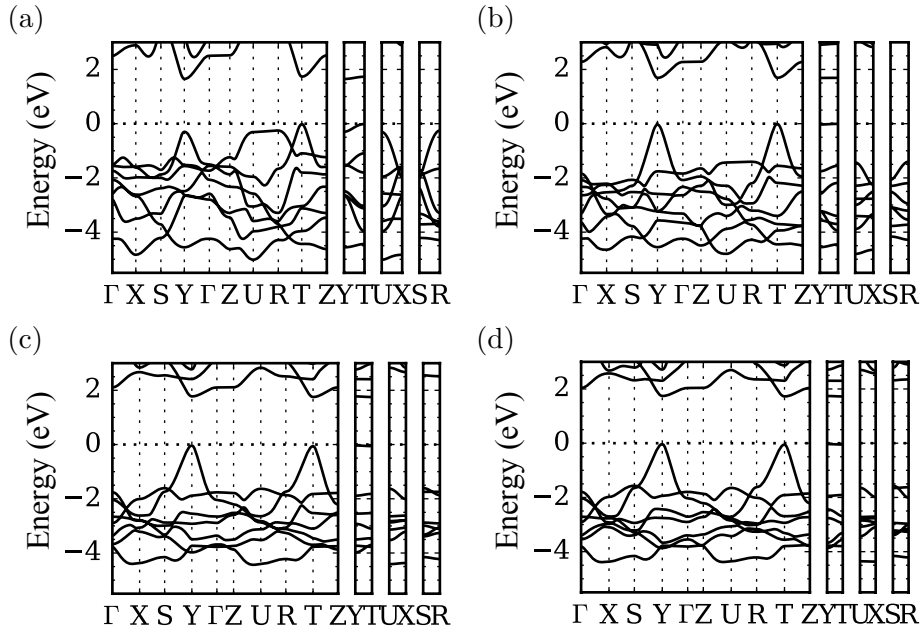
Figure 4.3:   Band structures for (a) LiTiO$_2$H, (b) NaTiO$_2$H, (c) RbTiO$_2$H, and (d) CsTiO$_2$H. The energy is measured from the VBM.

CsTiO$_2$H. It indicates that the two-dimensional character is weakened as $A = $ Cs to Li. This trend can be understood as the result of decreasing in the length of the c-axis, hence the result of decreasing in the ionic radius of the A-site atom.

4.4   Dielectric properties

The Born effective charge tensors are listed in Table 4.4. For all the compounds, the H atoms are negatively charged. The Born effective charge tensors for these compounds hardly vary except that for Ti and the zz component of that for O$_{\mathrm{ap}}$. The variation in the yy component for Ti go along with that in the length of b-axis.

The z components of the spontaneous electric polarizations are $102\,\mu\mathrm{C/cm}^2$, $105\,\mu\mathrm{C/cm}^2$, $102\,\mu\mathrm{C/cm}^2$, $98\,\mu\mathrm{C/cm}^2$, and $97\,\mu\mathrm{C/cm}^2$ for $A = $ Li, Na, K, Rb, Cs, respectively. It is obvious from the atomic displacements from the centrosymmetric structures that the x and y components are zero. Their spontaneous electric polarizations are much larger than the calculated value of $25\,\mu\mathrm{C/cm}^2$ for tetragonal BaTiO$_3$ [49]. The variation of the spontaneous electric polarizations between these compounds is small, namely, it is not affected by the A-site atom.

The static dielectric tensors are listed in Table 4.5. Comparing the values with those for tetragonal BaTiO$_3$ [49], the clamped-ion terms for ATiO$_2$H are slightly smaller. For the internal-strain terms, the xx and yy components are comparable or larger than the xx component for tetragonal BaTiO$_3$, while the zz components are only several percent

Table 4.4: Born effective charge tensors for $A\mathrm{TiO_2H}$ ($A = \mathrm{Li, Na, K, Rb, Cs}$). Only symmetrically independent components are listed.

		$A = \mathrm{Li}$	$A = \mathrm{Na}$	$A = \mathrm{K}$	$A = \mathrm{Rb}$	$A = \mathrm{Cs}$
A	xx	1.18	1.05	1.06	1.09	1.16
	yy	1.18	1.10	1.19	1.26	1.36
	zz	1.33	1.40	1.47	1.52	1.73
Ti	xx	6.71	6.30	5.91	5.89	5.84
	yy	2.83	3.08	3.53	3.67	3.82
	zz	3.93	2.60	2.32	2.39	2.48
$\mathrm{O_{ap}}$	xx	−1.12	−0.93	−0.91	−0.92	−0.99
	yy	−1.04	−0.99	−1.09	−1.16	−1.27
	zz	−3.59	−2.48	−2.26	−2.30	−2.48
$\mathrm{O_{ip}}$	xx	−6.05	−5.78	−5.46	−5.48	−5.44
	yy	−1.34	−1.33	−1.42	−1.47	−1.50
	zz	−1.33	−1.17	−1.18	−1.22	−1.33
H	xx	−0.72	−0.63	−0.60	−0.58	−0.57
	yy	−1.64	−1.87	−2.20	−2.30	−2.41
	zz	−0.33	−0.33	−0.34	−0.37	−0.40

of that for tetragonal $\mathrm{BaTiO_3}$. Although the clamped-ion terms are fairly isotropic, that for $\mathrm{CsTiO_2H}$ is slightly anisotropic in the z direction, and that for $\mathrm{LiTiO_2H}$ is anisotropic in the x direction. These anisotropy could be originated from the electronic state near the VBM. For $\mathrm{CsTiO_2H}$, the state at the VBM is distributed in the plane perpendicular to the z direction. The state is hard to be polarized in the z direction by the electric field, resulting in the small value of the zz component. For $\mathrm{LiTiO_2H}$, the state below the VBM, which is perpendicular to the y direction (the k-point path U–R), affects to the xx component in the same manner. In the internal-strain terms, the xx components are largest for all the compounds, and become small as $A = \mathrm{Li}$ to Cs. This trend is the same as that in the xx components of the Born effective charge tensor for Ti. Since the xx components for Ti are largest within all the components of the Born effective charge tensor, it could cause the large xx components of the internal-strain terms.

The piezoelectric stress tensors are listed in Table 4.6. For all the compounds, the total piezoelectric tensors are smaller than that for tetragonal $\mathrm{BaTiO_3}$ which are $-0.70\,\mathrm{C/m^2}$ for the $z1$ component, $6.7\,\mathrm{C/m^2}$ for the $z3$ component, and $34.19\,\mathrm{C/m^2}$ for the $x5$ component [50]. While the $x5$ component is largest for tetragonal $\mathrm{BaTiO_3}$, the $z3$ component is largest for these oxyhydrides. Although the $x5$ components of

Table 4.5: Static dielectric tensors in units of the permittivity of vacuum for ATiO$_2$H ($A =$ Li, Na, K, Rb, Cs). Only symmetrically independent components are listed.

		$A =$ Li	$A =$ Na	$A =$ K	$A =$ Rb	$A =$ Cs	tetragonal BaTiO$_3$[*]
ci	xx	6.26	5.44	4.70	4.62	4.61	6.7
	yy	4.47	4.31	4.39	4.50	4.64	
	zz	4.42	3.29	3.04	3.14	3.35	6.1
is	xx	22.89	12.36	8.07	7.64	7.55	7.0
	yy	4.28	2.97	4.49	6.07	7.52	
	zz	2.31	0.83	0.63	0.61	0.67	43.1
total	xx	29.15	17.80	12.77	12.26	12.16	13.7
	yy	8.74	7.27	8.88	10.57	12.16	
	zz	6.73	4.12	3.67	3.75	4.02	49.2

[*] Ref. 49.

the clamped-ion terms for these compounds are largest, they are compensated by the internal-strain terms. The compensation between the two terms also emerges in other materials [29, 30]. The trend in the $z3$ components of the internal-strain terms, which decrease as $A =$ Li to Cs, might be explained by the length of the c-axis. For LiTiO$_2$H, since the space around the TiO$_3$H$_2$ hexahedron is extended by stretching of the c-axis, the displacement of atoms, hence the electric polarization, is encouraged. While for CsTiO$_2$H, there is enough space before the stretching of the c-axis, resulting in the small enhancement of the electric polarization.

As discussed above, the trends in the dielectric properties can be typically understood by those in the crystal structure and electronic structure. It is mentioned in the previous sections that the trends in the crystal structure and electronic structure result in the trend in the ionic radius of the A-site atom. Therefore, the trends in the dielectric properties can also be understood as the difference of the ionic radii.

Table 4.6: Piezoelectric stress tensors in C/m^2 for ATiO$_2$H (A = Li, Na, K, Rb, Cs). Only symmetrically independent components are listed. The second indices 1 to 5 denote the Voigt indices xx, yy, zz, yz, and xz, respectively.

		A = Li	A = Na	A = K	A = Rb	A = Cs
ci	$z1$	0.29	0.22	0.22	0.25	0.30
	$z2$	0.00	0.03	0.06	0.09	0.14
	$z3$	0.62	0.42	0.26	0.21	0.11
	$y4$	0.13	0.15	0.15	0.15	0.17
	$x5$	0.63	0.71	0.61	0.58	0.57
is	$z1$	−0.58	−0.53	−0.47	−0.46	−0.43
	$z2$	0.13	0.19	0.14	0.11	0.10
	$z3$	2.12	0.94	0.63	0.60	0.54
	$y4$	−0.22	−0.16	0.04	0.15	0.22
	$x5$	−0.40	−0.49	−0.39	−0.34	−0.31
total	$z1$	−0.29	−0.31	−0.26	−0.21	−0.13
	$z2$	0.14	0.22	0.20	0.19	0.24
	$z3$	2.74	1.36	0.89	0.81	0.64
	$y4$	−0.08	−0.01	0.19	0.30	0.39
	$x5$	0.23	0.22	0.22	0.24	0.26

Chapter 5

Development of decomposition methods for the shielding tensor

In this chapter, decomposition methods of the shielding tensor are formulated. Through this chapter, we use the Hartree atomic units with Gaussian cgs units, namely, the speed of light c is equal to the inverse of the fine-structure constant.

We decompose the shielding tensor based on the converse approach. In the converse approach, the shielding tensor for the atom s is calculated from the orbital magnetization:

$$\sigma_{s,\alpha\beta} = -\Omega \frac{\partial M_\beta}{\partial m_{s,\alpha}}, \tag{2.37}$$

where Ω is the volume of the cell, $\boldsymbol{m}_s$ is the magnetic dipole moment at the position of the atom s, $\boldsymbol{M}$ is the orbital magnetization induced by $\boldsymbol{m}_s$, and α and β indicates Cartesian directions. The decomposition of the shielding tensor can be achieved by decomposing the orbital magnetization $\boldsymbol{M}$.

The total orbital magnetization is given by the differentiation of the grand potential $E - \mu N_{\mathrm{e}}$ as mentioned in Sec. 2.3, where E is the total energy, μ is the chemical potential, and N_{e} is the number of electrons. Since $\partial N_{\mathrm{e}}/\partial \boldsymbol{B}^{\mathrm{ext}}$ is related to Chern numbers (in three dimensions) $\boldsymbol{C}$, the total orbital magnetization can be written as

$$
\begin{aligned}
M_\alpha &= -\frac{1}{\Omega} \operatorname{tr}\left[\mathcal{P}\left(\frac{\partial \mathcal{H}_{\boldsymbol{B}^{\mathrm{ext}}}}{\partial B_\alpha^{\mathrm{ext}}}\right)_{\boldsymbol{B}^{\mathrm{ext}}=\boldsymbol{0}}\right] + \frac{1}{\Omega}\mu\left(\frac{\partial N_{\mathrm{e}}}{\partial B_\alpha^{\mathrm{ext}}}\right)_{\boldsymbol{B}^{\mathrm{ext}}=\boldsymbol{0}} \\
&= -\frac{1}{2c\Omega} \operatorname{tr}(\mathcal{P}\boldsymbol{r} \times \boldsymbol{v}) + \frac{\mu}{(2\pi)^2 c}C_\alpha \\
&= \frac{1}{2c\Omega} \operatorname{Im}\operatorname{tr}(\mathcal{P}\boldsymbol{r} \times \mathcal{Q}\mathcal{H}\mathcal{Q}\boldsymbol{r}\mathcal{P} - \mathcal{Q}\boldsymbol{r} \times \mathcal{P}\mathcal{H}\mathcal{P}\boldsymbol{r}\mathcal{Q} - 2\mu\mathcal{P}\boldsymbol{r} \times \mathcal{Q}\boldsymbol{r}\mathcal{P}), \tag{5.1}
\end{aligned}
$$

where $\mathcal{H}_{\boldsymbol{B}^{\mathrm{ext}}}$ is the Hamiltonian with the external magnetic field given in Eq. (2.41), $\mathcal{H}$ is the Hamiltonian without the external magnetic field, $\mathcal{P}$ is the projector onto occupied states, $\mathcal{Q} = 1 - \mathcal{P}$, $\boldsymbol{v} = [\boldsymbol{r}, \mathcal{H}]/i$, and the symmetric gauge $\boldsymbol{A}(\boldsymbol{r}) = \boldsymbol{B}^{\mathrm{ext}} \times \boldsymbol{r}/2$

is taken. This expression is well-defined although the position operator $\boldsymbol{r}$ is included, because $\boldsymbol{r}$ appears in the form of $\mathcal{P}\boldsymbol{r}\mathcal{Q}$ which is well-defined even in periodic boundary conditions.

We derive three types of the decomposition by transforming Eq. (5.1) as

$$\boldsymbol{M} = \frac{1}{2c\Omega} \operatorname{Im} \operatorname{tr}(\mathcal{P}\boldsymbol{r} \times \mathcal{Q}\mathcal{H}\mathcal{Q}\boldsymbol{r}\mathcal{P} + \mathcal{P}\mathcal{H}\mathcal{P}\boldsymbol{r} \times \mathcal{Q}\boldsymbol{r}\mathcal{P} - 2\mu\mathcal{P}\boldsymbol{r} \times \mathcal{Q}\boldsymbol{r}\mathcal{P}), \qquad (5.2)$$

and then taking the trace operation as different forms. The reason for this transformation is mentioned in Sec. 5.5. Since all the position operators in Eq. (5.2) appear in the form of $\mathcal{P}\boldsymbol{r}\mathcal{Q}$, decomposed orbital magnetizations are well-defined even after decomposing the trace operation. In Sec. 5.1, we review previous studies about the decomposition. In Sec. 5.2, the decomposition into contributions of Wannier orbitals is provided. In Sec. 5.3, as a special case of Sec. 5.2, we derive the decomposition into contributions of energy bands. In Sec. 5.4, the spatial decomposition is provided. In Sec. 5.5, reciprocal-space expressions for these decompositions are derived, and relation to the modern theory of orbital magnetization is clarified. In Sec. 5.6, we prove the translational invariance of the decomposed shielding tensors. It is an advantage of the present decompositions because the translational invariance is not held in the decomposition into paramagnetic and diamagnetic terms mentioned in Sec. 2.3. In Sec. 5.7, gauge dependences of the decomposed orbital magnetizations on magnetic vector potentials are discussed. Finally, in Sec. 5.8, we verify the computation in the presented method numerically.

5.1   Previous decompositions

In this section, we introduce the following three ways of decompositions for the shielding tensor: (i) the traditional decomposition into the paramagnetic and diamagnetic terms [51], (ii) the decomposition into contribution from the induced current at each spatial point [38], (iii) the decomposition into the "local marker" which is formulated in recent years based on the modern theory of orbital magnetization [35,52]. Reference 38 presents the calculation method for the shielding tensor based on the augmented plane wave + local orbital (APW+lo) method, and does not intend to decompose the shielding tensor. However, since the decomposed value is mentioned to verify the necessity of an integration out of atomic spheres, we introduce this decomposition. Although the decomposition (iii) is a way of decomposition for the orbital magnetization, it is equivalent to decomposing the shielding tensor within the converse approach.

The first way is the decomposition into the paramagnetic and diamagnetic terms. The shielding tensor is determined by the induced magnetic field from its definition in Eq. (2.36). The induced magnetic field $\boldsymbol{B}_s^{\mathrm{ind}}$ at the atom s can be written by using the

Biot–Savart law as

$$\boldsymbol{B}_s^{\text{ind}} = \frac{1}{c} \int d^3r \, \boldsymbol{j}^{\text{ind}}(\boldsymbol{r}) \times \frac{\boldsymbol{r} - \boldsymbol{r}_s}{|\boldsymbol{r} - \boldsymbol{r}_s|^3}, \tag{5.3}$$

where $\boldsymbol{j}^{\text{ind}}(\boldsymbol{r})$ is the induced current and $\boldsymbol{r}_s$ is the position of the atom s. Since $\boldsymbol{j}^{\text{ind}}(\boldsymbol{r})$ can be decomposed into the paramagnetic and diamagnetic current as

$$\boldsymbol{j}^{\text{ind}}(\boldsymbol{r}) = \boldsymbol{j}_{\text{para}}^{\text{ind}}(\boldsymbol{r}) + \boldsymbol{j}_{\text{dia}}^{\text{ind}}(\boldsymbol{r}), \tag{5.4a}$$

$$\boldsymbol{j}_{\text{para}}^{\text{ind}}(\boldsymbol{r}) = \frac{1}{2}[\Psi^{(1)*}(\boldsymbol{r})\boldsymbol{\nabla}\Psi^{(0)}(\boldsymbol{r}) - \Psi^{(0)}(\boldsymbol{r})\boldsymbol{\nabla}\Psi^{(1)*}(\boldsymbol{r})] + \text{c.c.}, \tag{5.4b}$$

$$\boldsymbol{j}_{\text{dia}}^{\text{ind}}(\boldsymbol{r}) = -\frac{1}{c}\boldsymbol{A}(\boldsymbol{r})|\Psi^{(0)}(\boldsymbol{r})|^2, \tag{5.4c}$$

where $\Psi^{(0)}(\boldsymbol{r})$ is the unperturbed ground state wavefunction, $\Psi^{(1)}(\boldsymbol{r})$ is the first-order perturbation of $\Psi^{(0)}(\boldsymbol{r})$ with respect to the external magnetic field, and $\boldsymbol{A}(\boldsymbol{r})$ is the magnetic vector potential corresponding to the external magnetic field. The induced magnetic field can be decomposed into the paramagnetic and magnetic terms accordingly, and hence the shielding tensor. However, this decomposition is not unique. It is obvious from Eq. (5.4c) that this decomposition depends on the gauge of the magnetic vector potential.

The second way is the decomposition into contribution from the induced current at each spatial point. It is achieved by decomposing the integral of Eq. (5.3) for each $\boldsymbol{r}$ as

$$\sigma_s = \int d^3r \, \sigma_{\text{I}s}(\boldsymbol{r}), \tag{5.5}$$

$$\sigma_{\text{I}s,\alpha\beta}(\boldsymbol{r}) = -\frac{1}{c}\frac{\partial}{\partial B_\beta^{\text{ext}}} j_\alpha^{\text{ind}}(\boldsymbol{r}) \times \frac{\boldsymbol{r} - \boldsymbol{r}_s}{|\boldsymbol{r} - \boldsymbol{r}_s|^3}. \tag{5.6}$$

The direct approach should be taken to calculate decomposed values because the induced current is necessary.

The third way is the decomposition of the orbital magnetization into spatial contributions. This can be utilized to decompose the shielding tensor calculated by the converse approach. This decomposition of the orbital magnetization is performed by taking the trace operation in Eq. (5.1) as an integration with respect to $\boldsymbol{r}$ as

$$\boldsymbol{M} = \frac{1}{\Omega} \int d^3r \, \mathfrak{M}(\boldsymbol{r}), \tag{5.7a}$$

$$\mathfrak{M}(\boldsymbol{r}) = \frac{1}{2c} \text{Im} \langle \boldsymbol{r} | \left(\mathcal{P}\boldsymbol{r} \times \mathcal{Q}\mathcal{H}\mathcal{Q}\boldsymbol{r}\mathcal{P} - \mathcal{Q}\boldsymbol{r} \times \mathcal{P}\mathcal{H}\mathcal{P}\boldsymbol{r}\mathcal{Q} - 2\mu\mathcal{P}\boldsymbol{r} \times \mathcal{Q}\boldsymbol{r}\mathcal{P} \right) | \boldsymbol{r} \rangle. \tag{5.7b}$$

Note that $\mathfrak{M}(\boldsymbol{r})$ is not invariant to the gauge of the magnetic vector potential.

5.2 Decomposition into contributions of Wannier orbitals

In this section, we provide the decomposition into contributions of Wannier orbitals. The Wannier orbital $|w_{n\boldsymbol{R}}\rangle$ is defined as

$$|w_{n\boldsymbol{R}}\rangle = \frac{\Omega}{(2\pi)^3} \int_{\text{BZ}} d^3k \, e^{-i\boldsymbol{k}\cdot\boldsymbol{R}} |\psi_{n\boldsymbol{k}}\rangle, \tag{5.8}$$

where $|\psi_{n\boldsymbol{k}}\rangle$ is the Bloch orbital and $\boldsymbol{R}$ is a lattice vector. Since the trace operation is taken within a single cell, Eq. (5.2) is transformed as

$$\boldsymbol{M} = \frac{1}{2c\Omega} \text{Im} \sum_n^{\text{occ.}} \langle w_{n\boldsymbol{0}} | \left(\boldsymbol{r} \times \mathcal{Q}\mathcal{H}\mathcal{Q}\boldsymbol{r} + \mathcal{H}\mathcal{P}\boldsymbol{r} \times \mathcal{Q}\boldsymbol{r} - 2\mu\boldsymbol{r} \times \mathcal{Q}\boldsymbol{r} \right) |w_{n\boldsymbol{0}}\rangle \tag{5.9}$$

by using $\mathcal{P} = \sum_{n\boldsymbol{R}}^{\text{occ.}} |w_{n\boldsymbol{R}}\rangle \langle w_{n\boldsymbol{R}}|$. Then, $\boldsymbol{M}$ can be decomposed into contributions labeled by indices of Wannier orbitals as

$$\boldsymbol{M} = \sum_n^{\text{occ.}} \boldsymbol{m}_n^{\text{Wannier}}, \tag{5.10a}$$

$$\boldsymbol{m}_n^{\text{Wannier}} = \frac{1}{2c\Omega} \text{Im} \langle w_{n\boldsymbol{0}} | \left(\boldsymbol{r} \times \mathcal{Q}\mathcal{H}\mathcal{Q}\boldsymbol{r} + \mathcal{H}\mathcal{P}\boldsymbol{r} \times \mathcal{Q}\boldsymbol{r} - 2\mu\boldsymbol{r} \times \mathcal{Q}\boldsymbol{r} \right) |w_{n\boldsymbol{0}}\rangle. \tag{5.10b}$$

From Eq. (2.37), the Wannier-decomposed shielding tensor is defined as

$$\sigma_s = \sum_n^{\text{occ.}} \sigma_{sn}^{\text{Wannier}}, \tag{5.11a}$$

$$\sigma_{sn,\alpha\beta}^{\text{Wannier}} = -\Omega \frac{\partial m_{n,\beta}^{\text{Wannier}}}{\partial m_{s,\alpha}}. \tag{5.11b}$$

Equation (5.11b) represents the shielding by the n-th Wannier orbital.

5.3 Decomposition into contributions of energy bands

As a special case of the Wannier decomposition, we can consider the decomposition with Wannier orbitals which are constructed from energy eigenstates. The definition of the Wannier orbital in Eq. (5.8) can be rewritten as

$$|w_{n\boldsymbol{R}}\rangle = \frac{\Omega}{(2\pi)^3} \int_{\text{BZ}} d^3k \, e^{-i\boldsymbol{k}\cdot\boldsymbol{R}} \sum_m |\psi_{m\boldsymbol{k}}^{\text{H}}\rangle U_{mn}^{(\boldsymbol{k})}, \tag{5.12}$$

where $|\psi_{n\boldsymbol{k}}^{\text{H}}\rangle$ is the energy eigenstate and $U^{(\boldsymbol{k})}$ is a unitary matrix. The superscript "H" indicates the Hamiltonian gauge. The unitary matrix comes from a gauge freedom for

a set of Bloch orbitals. If unitary matrices are set to identities, the Wannier orbital becomes

$$|w_{n\boldsymbol{R}}^{\mathrm{H}}\rangle = \frac{\Omega}{(2\pi)^3} \int_{\mathrm{BZ}} d^3k\, e^{-i\boldsymbol{k}\cdot\boldsymbol{R}} |\psi_{n\boldsymbol{k}}^{\mathrm{H}}\rangle. \tag{5.13}$$

In this case, one Wannier orbital corresponds to one energy eigenstate, and thus, the index of the Wannier orbital can be regarded as the band index. In other words, the orbital magnetization and shielding tensor can be decomposed into contributions of energy bands. Thus, the band-decomposed orbital magnetization is defined as

$$\boldsymbol{M} = \sum_{n}^{\mathrm{occ.}} \boldsymbol{m}_n^{\mathrm{band}}, \tag{5.14a}$$

$$\boldsymbol{m}_n^{\mathrm{band}} = \frac{1}{2c\Omega} \operatorname{Im} \langle w_{n\boldsymbol{0}}^{\mathrm{H}}| \left(\boldsymbol{r} \times \mathcal{Q}\mathcal{H}\mathcal{Q}\boldsymbol{r} + \mathcal{H}\mathcal{P}\boldsymbol{r} \times \mathcal{Q}\boldsymbol{r} - 2\mu\boldsymbol{r} \times \mathcal{Q}\boldsymbol{r}\right) |w_{n\boldsymbol{0}}^{\mathrm{H}}\rangle. \tag{5.14b}$$

The band-decomposed shielding tensor is accordingly defined as

$$\sigma_s = \sum_{n}^{\mathrm{occ.}} \sigma_{sn}^{\mathrm{band}}, \tag{5.15a}$$

$$\sigma_{sn,\alpha\beta}^{\mathrm{band}} = -\Omega \frac{\partial m_{n,\beta}^{\mathrm{band}}}{\partial m_{s,\alpha}}. \tag{5.15b}$$

Additionally, by summing band contributions over bands in a bunch, the total orbital magnetization can be decomposed into bunch contributions as

$$\boldsymbol{M} = \sum_{b}^{\mathrm{occ.\ bunch}} \boldsymbol{m}_b^{\mathrm{bunch}}, \tag{5.16a}$$

$$\boldsymbol{m}_b^{\mathrm{bunch}} = \sum_{n}^{\mathrm{bunch}\ b} \boldsymbol{m}_n^{\mathrm{band}}. \tag{5.16b}$$

Consequently, the bunch-decomposed shielding tensor is defined as

$$\sigma_s = \sum_{b}^{\mathrm{occ.\ bunch}} \sigma_{sb}^{\mathrm{bunch}}, \tag{5.17a}$$

$$\sigma_{sb,\alpha\beta}^{\mathrm{bunch}} = -\Omega \frac{\partial m_{b,\beta}^{\mathrm{bunch}}}{\partial m_{s,\alpha}}. \tag{5.17b}$$

The bunch decomposition can also be defined as the summation of the Wannier-decomposed contributions within each bunch if the unitary transformation is applied within each bunch. However, this bunch decomposition based on the Wannier decomposition is identical to that based on the band decomposition. When the unitary transformation is applied within each bunch, the whole unitary matrix $U^{(\boldsymbol{k})}$ is block-diagonal and each block is a unitary matrix. Therefore, the whole unitary matrix satisfies

$$\sum_{n}^{\mathrm{bunch}\ b} U_{m'n}^{(\boldsymbol{k})*} U_{mn}^{(\boldsymbol{k})} = \begin{cases} \delta_{m'm}, & \text{if both } m' \text{ and } m \text{ are in the bunch } b \\ 0, & \text{otherwise} \end{cases} \tag{5.18}$$

which indicates unitarity in each bunch. If we refer to the bunch decomposition based on the Wannier decomposition as

$$\boldsymbol{m}_b^{\text{Wannier,bunch}} = \sum_n^{\text{bunch } b} \boldsymbol{m}_n^{\text{Wannier}}, \tag{5.19}$$

it can be transformed as

$$
\begin{aligned}
\boldsymbol{m}_b^{\text{Wannier,bunch}} =& \sum_n^{\text{bunch } b} \frac{1}{2c\Omega} \, \text{Im} \, \frac{\Omega}{(2\pi)^3} \int_{\text{BZ}} d^3k' \, \frac{\Omega}{(2\pi)^3} \int_{\text{BZ}} d^3k \sum_{m'm}^{\text{occ.}} \\
& U_{m'n}^{(\boldsymbol{k}')*} \, \langle \psi_{m'\boldsymbol{k}'}^{\text{H}} | \, (\boldsymbol{r} \times \mathcal{Q}\mathcal{H}\mathcal{Q}\boldsymbol{r} + \mathcal{H}\mathcal{P}\boldsymbol{r} \times \mathcal{Q}\boldsymbol{r} - 2\mu\boldsymbol{r} \times \mathcal{Q}\boldsymbol{r}) \, | \psi_{m\boldsymbol{k}}^{\text{H}} \rangle \, U_{mn}^{(\boldsymbol{k})} \\
=& \frac{1}{2c\Omega} \, \text{Im} \, \frac{\Omega}{(2\pi)^3} \int_{\text{BZ}} d^3k' \, \frac{\Omega}{(2\pi)^3} \int_{\text{BZ}} d^3k \sum_m^{\text{bunch } b} \\
& \langle \psi_{m\boldsymbol{k}'}^{\text{H}} | \, (\boldsymbol{r} \times \mathcal{Q}\mathcal{H}\mathcal{Q}\boldsymbol{r} + \mathcal{H}\mathcal{P}\boldsymbol{r} \times \mathcal{Q}\boldsymbol{r} - 2\mu\boldsymbol{r} \times \mathcal{Q}\boldsymbol{r}) \, | \psi_{m\boldsymbol{k}}^{\text{H}} \rangle \\
=& \, \boldsymbol{m}_b^{\text{band}}.
\end{aligned}
\tag{5.20}
$$

The bunch decomposed shielding tensors based on the Wannier and band decompositions are accordingly identical.

5.4   Decomposition into spatial contributions

In this section, we decompose the shielding tensor into spatial contributions, namely, expressing the shielding tensor as a function of the position $\boldsymbol{r}$. In contrast to the Wannier decomposition and band decomposition, we take the trace operation in Eq. (5.2) as the integration in $\boldsymbol{r}$:

$$\boldsymbol{M} = \frac{1}{2c\Omega} \, \text{Im} \int d^3r \, \langle \boldsymbol{r} | \, (\mathcal{P}\boldsymbol{r} \times \mathcal{Q}\mathcal{H}\mathcal{Q}\boldsymbol{r}\mathcal{P} + \mathcal{P}\mathcal{H}\mathcal{P}\boldsymbol{r} \times \mathcal{Q}\boldsymbol{r}\mathcal{P} - 2\mu\mathcal{P}\boldsymbol{r} \times \mathcal{Q}\boldsymbol{r}\mathcal{P}) \, | \boldsymbol{r} \rangle. \tag{5.21}$$

By decomposing into contributions of $\boldsymbol{r}$, we obtain the spatially decomposed orbital magnetization as

$$\boldsymbol{M} = \frac{1}{\Omega} \int d^3r \, \boldsymbol{m}(\boldsymbol{r}), \tag{5.22a}$$

$$\boldsymbol{m}(\boldsymbol{r}) = \frac{1}{2c} \, \text{Im} \, \langle \boldsymbol{r} | \, (\mathcal{P}\boldsymbol{r} \times \mathcal{Q}\mathcal{H}\mathcal{Q}\boldsymbol{r}\mathcal{P} + \mathcal{P}\mathcal{H}\mathcal{P}\boldsymbol{r} \times \mathcal{Q}\boldsymbol{r}\mathcal{P} - 2\mu\mathcal{P}\boldsymbol{r} \times \mathcal{Q}\boldsymbol{r}\mathcal{P}) \, | \boldsymbol{r} \rangle. \tag{5.22b}$$

Although this derivation is in the same manner as Ref. 35, the order of operators in the second term of Eq. (5.22b) is altered from Eq. (8) in Ref. 35. The reason is mentioned in Sec. 5.5. As a consequence of Eq. (5.22b), the spatially decomposed shielding tensor is defined as

$$\sigma_s = \frac{1}{\Omega} \int d^3r \, \sigma_s(\boldsymbol{r}), \tag{5.23a}$$

$$\sigma_{s,\alpha\beta}(\boldsymbol{r}) = -\Omega \frac{\partial m_\beta(\boldsymbol{r})}{\partial m_{s,\alpha}}. \tag{5.23b}$$

The spatially decomposed shielding tensor indicates which region in the space contributes to the shielding.

Basing on the spatial decomposition, we can formulate a further decomposition into atomic contributions by utilizing the Bader analysis [53]. The Bader analysis is the method to assign charges to atoms. A charge density is divided in regions on which surfaces the gradient of the charge density is parallel to the surface. Since the charge density generally has maxima at atoms, each region contains one atom. Then, charges or the charge density in the region is assigned to the corresponding atom. If the spatially decomposed isotropic shielding $\sigma_s^{\mathrm{iso}}(\boldsymbol{r}) = \operatorname{tr} \sigma_s(\boldsymbol{r})/3$ is divided instead of the charge density, it can be assigned to each atoms. A difference from the original method of the charge density is that $\sigma_s^{\mathrm{iso}}(\boldsymbol{r})$ is allowed to be both positive and negative. In order to apply the Bader analysis to such a function, we divide $\sigma_s^{\mathrm{iso}}(\boldsymbol{r})$ into the positive function $\sigma_s^{\mathrm{iso},+}(\boldsymbol{r})$ and the negative function $\sigma_s^{\mathrm{iso},-}(\boldsymbol{r})$ as

$$\sigma_s^{\mathrm{iso},+}(\boldsymbol{r}) = \begin{cases} \sigma_s^{\mathrm{iso}}(\boldsymbol{r}), & \text{if } \sigma_s^{\mathrm{iso}}(\boldsymbol{r}) > 0 \\ 0, & \text{otherwise} \end{cases}, \ \sigma_s^{\mathrm{iso},-}(\boldsymbol{r}) = \begin{cases} 0, & \text{if } \sigma_s^{\mathrm{iso}}(\boldsymbol{r}) > 0 \\ \sigma_s^{\mathrm{iso}}(\boldsymbol{r}), & \text{otherwise} \end{cases}. \quad (5.24)$$

The Bader analysis can be performed for $\sigma_s^{\mathrm{iso},+}(\boldsymbol{r})$ and $-\sigma_s^{\mathrm{iso},-}(\boldsymbol{r})$, and thus, we can obtain the atomic contributions of the spatially decomposed isotropic shielding.

5.5 Reciprocal-space expression

The Wannier-decomposed, band-decomposed, and spatially decomposed orbital magnetizations can be expressed in the reciprocal space. Firstly, we derive the reciprocal-space expression for the Wannier-decomposed orbital magnetization. Using the relation between the Wannier orbital and $|\partial_{\boldsymbol{k}} u_{n\boldsymbol{k}}\rangle$ in Eq. (2.31), where $|u_{n\boldsymbol{k}}\rangle$ is the periodic part of the Bloch orbital, the reciprocal-space expression is derived from Eq. (5.10b) as

$$\begin{aligned} \boldsymbol{m}_n^{\mathrm{Wannier}} =& \frac{1}{2c\Omega} \operatorname{Im} \frac{\Omega}{(2\pi)^3} \int_{\mathrm{BZ}} d^3k \sum_m^{\mathrm{occ.}} \\ & \langle \partial_{\boldsymbol{k}} u_{m\boldsymbol{k}}| \times \mathcal{Q}_{\boldsymbol{k}} (\delta_{nm}\mathcal{H}_{\boldsymbol{k}} + E_{nm\boldsymbol{k}} - 2\mu\delta_{nm}) \mathcal{Q}_{\boldsymbol{k}} |\partial_{\boldsymbol{k}} u_{n\boldsymbol{k}}\rangle \\ =& \frac{1}{2c\Omega} \operatorname{Im} \frac{\Omega}{(2\pi)^3} \int_{\mathrm{BZ}} d^3k \sum_m^{\mathrm{occ.}} \langle \widetilde{\partial}_{\boldsymbol{k}} u_{m\boldsymbol{k}}| \times (\delta_{nm}\mathcal{H}_{\boldsymbol{k}} + E_{nm\boldsymbol{k}} - 2\mu\delta_{nm}) |\widetilde{\partial}_{\boldsymbol{k}} u_{n\boldsymbol{k}}\rangle, \end{aligned}$$

$$(5.25)$$

where $\mathcal{Q}_{\boldsymbol{k}} = e^{-i\boldsymbol{k}\cdot\boldsymbol{r}} \mathcal{Q} e^{i\boldsymbol{k}\cdot\boldsymbol{r}}$, $\mathcal{H}_{\boldsymbol{k}} = e^{-i\boldsymbol{k}\cdot\boldsymbol{r}} \mathcal{H} e^{i\boldsymbol{k}\cdot\boldsymbol{r}}$, $E_{mn\boldsymbol{k}} = \langle u_{m\boldsymbol{k}}| \mathcal{H}_{\boldsymbol{k}} |u_{n\boldsymbol{k}}\rangle$, and $|\widetilde{\partial}_{\boldsymbol{k}} u_{n\boldsymbol{k}}\rangle$ is the covariant derivative of $|u_{n\boldsymbol{k}}\rangle$ defined as $\mathcal{Q}_{\boldsymbol{k}} |\partial_{\boldsymbol{k}} u_{n\boldsymbol{k}}\rangle$. Secondly, we derive the reciprocal-space expression for the band-decomposed orbital magnetization. It can be achieved by setting the Bloch orbital to the energy eigenstate in the same manner as Sec. 5.3,

resulting in

$$\boldsymbol{m}_n^{\text{band}} = \frac{1}{2c\Omega} \operatorname{Im} \frac{\Omega}{(2\pi)^3} \int_{\text{BZ}} d^3k \, \langle \widetilde{\partial}_{\boldsymbol{k}} u_{n\boldsymbol{k}}^{\text{H}} | \times (\mathcal{H}_{\boldsymbol{k}} + \varepsilon_{n\boldsymbol{k}} - 2\mu) | \widetilde{\partial}_{\boldsymbol{k}} u_{n\boldsymbol{k}}^{\text{H}} \rangle, \qquad (5.26)$$

where $\varepsilon_{n\boldsymbol{k}}$ is the eigenenergy. Finally, we derive the reciprocal-space expression for the spatially decomposed orbital magnetization. From Eqs. (5.22b) and (2.31), it is derived as

$$\begin{aligned}
\boldsymbol{m}(\boldsymbol{r}) =& \frac{1}{2c} \operatorname{Im} \sum_{l'\boldsymbol{R}'}^{\text{occ.}} \sum_{l\boldsymbol{R}}^{\text{occ.}} \\
& \langle \boldsymbol{r} | w_{l'\boldsymbol{R}'} \rangle \langle w_{l'\boldsymbol{R}'} | (\boldsymbol{r} \times \mathcal{Q}\mathcal{H}\mathcal{Q}\boldsymbol{r} + \mathcal{H}\mathcal{P}\boldsymbol{r} \times \mathcal{Q}\boldsymbol{r} - 2\mu\boldsymbol{r} \times \mathcal{Q}\boldsymbol{r}) | w_{l\boldsymbol{R}} \rangle \langle w_{l\boldsymbol{R}} | \boldsymbol{r} \rangle \\
=& \frac{1}{2c} \operatorname{Im} \sum_{l'\boldsymbol{R}'}^{\text{occ.}} \sum_{l\boldsymbol{R}}^{\text{occ.}} \frac{\Omega}{(2\pi)^3} \int_{\text{BZ}} d^3k \sum_m^{\text{occ.}} \\
& \langle \boldsymbol{r} | w_{l'\boldsymbol{R}'} \rangle e^{i\boldsymbol{k}\cdot\boldsymbol{R}'} \langle \widetilde{\partial}_{\boldsymbol{k}} u_{m\boldsymbol{k}} | \times (\delta_{l'm}\mathcal{H}_{\boldsymbol{k}} + E_{l'm\boldsymbol{k}} - 2\mu\delta_{l'm}) | \widetilde{\partial}_{\boldsymbol{k}} u_{l\boldsymbol{k}} \rangle e^{-i\boldsymbol{k}\cdot\boldsymbol{R}} \langle w_{l\boldsymbol{R}} | \boldsymbol{r} \rangle \\
=& \frac{1}{2c} \operatorname{Im} \sum_{l'l}^{\text{occ.}} \frac{\Omega}{(2\pi)^3} \int_{\text{BZ}} d^3k \sum_m^{\text{occ.}} \\
& \langle \boldsymbol{r} | u_{l'\boldsymbol{k}} \rangle \langle \widetilde{\partial}_{\boldsymbol{k}} u_{m\boldsymbol{k}} | \times (\delta_{l'm}\mathcal{H}_{\boldsymbol{k}} + E_{l'm\boldsymbol{k}} - 2\mu\delta_{l'm}) | \widetilde{\partial}_{\boldsymbol{k}} u_{l\boldsymbol{k}} \rangle \langle u_{l\boldsymbol{k}} | \boldsymbol{r} \rangle.
\end{aligned} \qquad (5.27)$$

Now, we can unify the expressions for the Wannier, band, and spatial decompositions. We define the quantity $\boldsymbol{m}_{l'l\boldsymbol{k}}$ as

$$\boldsymbol{m}_{l'l\boldsymbol{k}} = \frac{1}{2c\Omega} \sum_m^{\text{occ.}} \langle \widetilde{\partial}_{\boldsymbol{k}} u_{m\boldsymbol{k}} | \times (\delta_{l'm}\mathcal{H}_{\boldsymbol{k}} + E_{l'm\boldsymbol{k}} - 2\mu\delta_{l'm}) | \widetilde{\partial}_{\boldsymbol{k}} u_{l\boldsymbol{k}} \rangle, \qquad (5.28)$$

and refer to as "orbital magnetization matrix." The orbital magnetization matrix is transformed by the unitary transformation in Eq. (5.12) as

$$\begin{aligned}
\boldsymbol{m}_{l'l\boldsymbol{k}} &= \sum_{n'n}^{\text{occ.}} U_{n'l'}^{(\boldsymbol{k})*} \frac{1}{2c\Omega} \langle \widetilde{\partial}_{\boldsymbol{k}} u_{n'\boldsymbol{k}}^{\text{H}} | \times (\mathcal{H}_{\boldsymbol{k}} + \varepsilon_{n'\boldsymbol{k}} - 2\mu) | \widetilde{\partial}_{\boldsymbol{k}} u_{n\boldsymbol{k}}^{\text{H}} \rangle U_{nl}^{(\boldsymbol{k})} \\
&= \sum_{n'n}^{\text{occ.}} U_{n'l'}^{(\boldsymbol{k})*} \boldsymbol{m}_{n'n\boldsymbol{k}}^{\text{H}} U_{nl}^{(\boldsymbol{k})},
\end{aligned} \qquad (5.29)$$

where we use that the covariant derivative $|\widetilde{\partial}_{\boldsymbol{k}} u_{n\boldsymbol{k}}\rangle$ follows the same unitary transformation as $|u_{n\boldsymbol{k}}\rangle$. Then, the reciprocal-space expressions for the decomposed orbital magnetizations can be rewritten by using the orbital magnetization matrix. From Eq. (5.25), the Wannier-decomposed orbital magnetization becomes

$$\boldsymbol{m}_n^{\text{Wannier}} = \operatorname{Im} \frac{\Omega}{(2\pi)^3} \int_{\text{BZ}} d^3k \, \boldsymbol{m}_{nn\boldsymbol{k}} \qquad (5.30a)$$

$$= \operatorname{Im} \frac{\Omega}{(2\pi)^3} \int_{\text{BZ}} d^3k \sum_{l'l}^{\text{occ.}} U_{l'n}^{(\boldsymbol{k})*} \boldsymbol{m}_{l'l\boldsymbol{k}}^{\text{H}} U_{ln}^{(\boldsymbol{k})}. \qquad (5.30b)$$
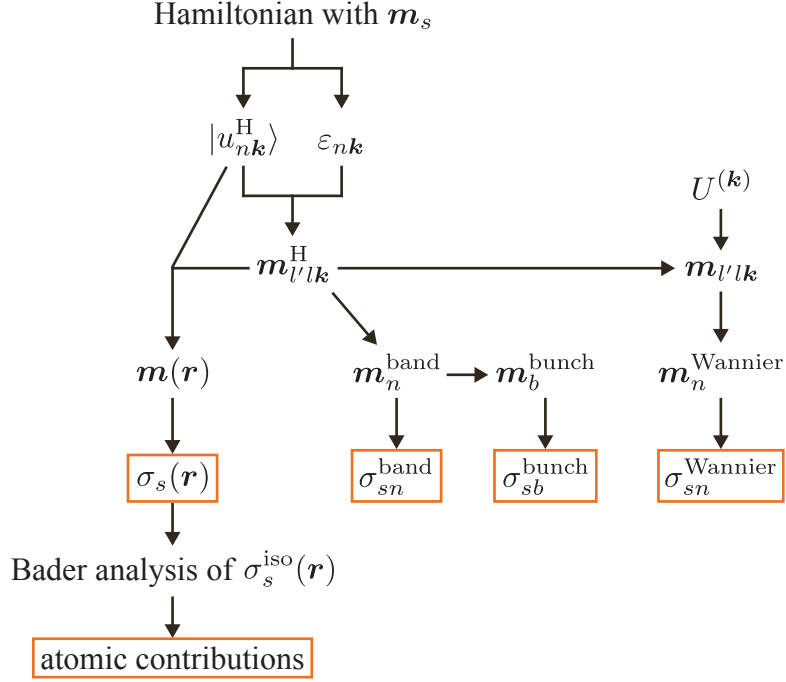
Hamiltonian with $\boldsymbol{m}_s$

Figure 5.1: Procedure for calculating the decomposed shielding tensors.

From Eq. (5.26), the band-decomposed orbital magnetization becomes

$$\boldsymbol{m}_n^{\text{band}} = \text{Im} \frac{\Omega}{(2\pi)^3} \int_{\text{BZ}} d^3k \, \boldsymbol{m}_{nn\boldsymbol{k}}^{\text{H}}. \tag{5.31}$$

From Eq. (5.27), the spatially decomposed orbital magnetization becomes

$$\boldsymbol{m}(\boldsymbol{r}) = \Omega \, \text{Im} \frac{\Omega}{(2\pi)^3} \int_{\text{BZ}} d^3k \sum_{l'l}^{\text{occ.}} \langle \boldsymbol{r} | u_{l'\boldsymbol{k}} \rangle \, \boldsymbol{m}_{l'l\boldsymbol{k}} \, \langle u_{l\boldsymbol{k}} | \boldsymbol{r} \rangle \tag{5.32a}$$

$$= \Omega \, \text{Im} \frac{\Omega}{(2\pi)^3} \int_{\text{BZ}} d^3k \sum_{l'l}^{\text{occ.}} \langle \boldsymbol{r} | u_{l'\boldsymbol{k}}^{\text{H}} \rangle \, \boldsymbol{m}_{l'l\boldsymbol{k}}^{\text{H}} \, \langle u_{l\boldsymbol{k}}^{\text{H}} | \boldsymbol{r} \rangle . \tag{5.32b}$$

As long as the orbital magnetization matrix is obtained within the Hamiltonian gauge, the band-decomposed orbital magnetization can be evaluated from only the matrix, the spatially decomposed orbital magnetization can be evaluated from the corresponding energy eigenfunctions, and the Wannier-decomposed orbital magnetization can be evaluated for a desired set of Wannier orbitals from a corresponding unitary matrix. The procedure for calculating the decomposed shielding tensors is summarized in Fig. 5.1.

The orbital magnetization matrix is closely related to the modern theory of orbital magnetization. The orbital magnetization matrix in Eq. (5.28) can be simply obtained as a component for each m, n and $\boldsymbol{k}$ of the gauge-invariant form of the orbital magnetization in Eq. (2.35). This is why we rearrange operators as Eq. (5.2). Unless the operators are rearranged, the resulting expressions for decompositions do not coincide with that of the modern theory of orbital magnetization. Although the definition of the

45

spatial decomposition differ from that in Ref. 35, the present definition is advantageous in the systematic decomposition and implementation of the code.

5.6   Translational invariance

In this section, we prove the translational invariance of the decomposed orbital magnetizations, hence the decomposed shielding tensors. The translational invariance is an advantage of the present decompositions against the decomposition into paramagnetic and diamagnetic terms mentioned in Sec. 2.3. When the system is translated by $\boldsymbol{a}$, quantities $\mathcal{H}$, $\mathcal{Q}$, and $|u_{n\boldsymbol{k}}\rangle$ are transformed as

$$\mathcal{H} \longrightarrow T^{\dagger}(\boldsymbol{a})\mathcal{H}T(\boldsymbol{a}), \tag{5.33}$$

$$\mathcal{Q} \longrightarrow T^{\dagger}(\boldsymbol{a})\mathcal{Q}T(\boldsymbol{a}), \tag{5.34}$$

$$|u_{n\boldsymbol{k}}\rangle \longrightarrow T^{\dagger}(\boldsymbol{a}) |u_{n\boldsymbol{k}}\rangle , \tag{5.35}$$

where $T(\boldsymbol{a})$ is the translation operator by $\boldsymbol{a}$, satisfying $T(\boldsymbol{a})|\boldsymbol{r}\rangle = |\boldsymbol{r} + \boldsymbol{a}\rangle$. By using them and $T^{\dagger}(\boldsymbol{a})T(\boldsymbol{a}) = 1$, the orbital magnetization matrix in Eq. (5.28) is invariant under the translation. Therefore, the Wannier- and band-decomposed orbital magnetizations are translationally invariant from Eqs. (5.30) and (5.31). The spatially decomposed orbital magnetization in Eq. (5.32) is invariant as well, because $|\boldsymbol{r}\rangle$ is transformed into $|\boldsymbol{r} - \boldsymbol{a}\rangle$.

5.7   Gauge dependence on magnetic vector potentials

In the converse approach, there are two magnetic vector potentials corresponding to the magnetic dipole moment and external magnetic field. In this section, we show how the decomposed orbital magnetizations depend on the gauge of these vector potentials. In conclusion, the decompositions are invariant against the gauge for the magnetic dipole moment, while the gauge invariance corresponding to the external magnetic field is not proved up to this point. For the latter case, we provide proofs of the invariance for specific gauge transformations.

Firstly, we show the gauge invariance for the magnetic vector potential corresponding to the magnetic dipole moment $\boldsymbol{m}_s$. The corresponding magnetic vector potential $\boldsymbol{A}_s(\boldsymbol{r})$ is contained in the Hamiltonian $\mathcal{H}$ as follows:

$$\mathcal{H} = \frac{1}{2} \left[\boldsymbol{p} + \frac{1}{c}\boldsymbol{A}_s(\boldsymbol{r}) \right]^2 + V(\boldsymbol{r}). \tag{5.36}$$

If $\boldsymbol{A}_s(\boldsymbol{r})$ is gauge-transformed into $\boldsymbol{A}_s(\boldsymbol{r}) + \boldsymbol{\nabla}\chi_s(\boldsymbol{r})$, where $\chi_s(\boldsymbol{r})$ is a real function, $\mathcal{H}$, $\mathcal{Q}$, and $|u_{n\boldsymbol{k}}\rangle$ are transformed as

$$\mathcal{H} \longrightarrow e^{-i\chi_s(\boldsymbol{r})/c}\mathcal{H}e^{i\chi_s(\boldsymbol{r})/c}, \tag{5.37}$$

$$\mathcal{Q} \longrightarrow e^{-i\chi_s(\boldsymbol{r})/c}\mathcal{Q}e^{i\chi_s(\boldsymbol{r})/c}, \tag{5.38}$$

$$|u_{n\boldsymbol{k}}\rangle \longrightarrow e^{-i\chi_s(\boldsymbol{r})/c}|u_{n\boldsymbol{k}}\rangle. \tag{5.39}$$

Therefore, the orbital magnetization matrix in Eq. (5.28) is invariant under the gauge transformation, which leads to the gauge invariance of the Wannier-decomposed, band-decomposed, and spatially decomposed orbital magnetizations from Eqs. (5.30), (5.31), and (5.32).

Secondly, we provide proofs of the gauge invariance corresponding to the external magnetic field in specific cases. Since the total orbital magnetization in the form of Eq. (5.1) is derived by using the symmetric gauge, we begin from derivation of the total orbital magnetization in an arbitrary magnetic vector potential. The procedure of the derivation is similar to that for the symmetric gauge in Ref. 35. The Hamiltonian with the external magnetic field $\boldsymbol{B}$ is

$$\mathcal{H}_{\boldsymbol{B}} = \frac{1}{2}\left[\boldsymbol{p} + \frac{1}{c}\boldsymbol{A}_s(\boldsymbol{r}) + \frac{1}{c}\boldsymbol{A}(\boldsymbol{r})\right]^2 + V(\boldsymbol{r}), \tag{5.40}$$

where $\boldsymbol{A}(\boldsymbol{r})$ is the magnetic vector potential corresponding to $\boldsymbol{B}$. The orbital magnetization $\boldsymbol{M}$ is obtained by differentiating the grand potential $\operatorname{tr}(\mathcal{P}\mathcal{H}_{\boldsymbol{B}}) - \mu N_{\mathrm{e}}$ by $\boldsymbol{B}$ as

$$M_\alpha = -\frac{1}{\Omega}\operatorname{tr}\left[\mathcal{P}\left(\frac{\partial}{\partial B_\alpha}\mathcal{H}_{\boldsymbol{B}}\right)_{\boldsymbol{B}=\boldsymbol{0}}\mathcal{P}\right] + \frac{1}{\Omega}\mu\left(\frac{\partial N_{\mathrm{e}}}{\partial B_\alpha}\right)_{\boldsymbol{B}=\boldsymbol{0}}, \tag{5.41}$$

where μ is the chemical potential, N_{e} is the number of electrons, and the Hellmann–Feynman theorem is used. From the Středa formula [54], the Hall conductivity is expressed as $c(\partial N_{\mathrm{e}}/\partial \boldsymbol{B})/\Omega$, and the Hall conductivity can also be expressed as $\boldsymbol{C}/(2\pi)^2$, where $\boldsymbol{C}$ is the Chern number (in three dimensions). By using these relations, we can proceed as

$$M_\alpha = -\frac{1}{c\Omega}\operatorname{Re}\operatorname{tr}\left\{\mathcal{P}\sum_\beta\left[\frac{\partial}{\partial B_\alpha}A_\beta(\boldsymbol{r})\right]_{\boldsymbol{B}=\boldsymbol{0}}v_\beta\mathcal{P}\right\} + \frac{\mu}{(2\pi)^2 c}C_\alpha, \tag{5.42}$$

where $\boldsymbol{v} = -i[\boldsymbol{r}, \mathcal{H}]$ is the velocity operator for the zero external magnetic field. Substituting $\mathcal{H} = \mathcal{P}\mathcal{H}\mathcal{P} + \mathcal{Q}\mathcal{H}\mathcal{Q}$ and $\boldsymbol{C} = -(2\pi)^2\operatorname{Im}\operatorname{tr}(\mathcal{P}\boldsymbol{r}\times\mathcal{Q}\boldsymbol{r}\mathcal{P})/\Omega$, and then, rearranging

operators, it is rewritten as

$$
M_\alpha = \frac{1}{c\Omega} \operatorname{Im} \operatorname{tr} \Biggl\{ \mathcal{P} \sum_\beta \left[\frac{\partial}{\partial B_\alpha} A_\beta(\boldsymbol{r}) \right]_{\boldsymbol{B}=\boldsymbol{0}} [(\mathcal{PHP} + \mathcal{QHQ})r_\beta - r_\beta \mathcal{PHP}]\mathcal{P}
$$

$$
- \mu \mathcal{P}\boldsymbol{r} \times \mathcal{Q}\boldsymbol{r}\mathcal{P} \Biggr\}
$$

$$
= \frac{1}{c\Omega} \operatorname{Im} \operatorname{tr} \Biggl\{ \sum_\beta \mathcal{P} \left[\frac{\partial}{\partial B_\alpha} A_\beta(\boldsymbol{r}) \right]_{\boldsymbol{B}=\boldsymbol{0}} \mathcal{QHQ}r_\beta \mathcal{P}
$$

$$
- \sum_\beta \mathcal{PHP}r_\beta \mathcal{Q} \left[\frac{\partial}{\partial B_\alpha} A_\beta(\boldsymbol{r}) \right]_{\boldsymbol{B}=\boldsymbol{0}} \mathcal{P} - \mu \mathcal{P}\boldsymbol{r} \times \mathcal{Q}\boldsymbol{r}\mathcal{P} \Biggr\}. \tag{5.43}
$$

This is identical to Eq. (5.2) if the symmetric gauge $\boldsymbol{A}(\boldsymbol{r}) = \boldsymbol{B} \times \boldsymbol{r}/2$ is taken. Then, we can define the Wannier, band, and spatial decomposition for an arbitrary magnetic vector potential as

$$
m_{n,\alpha}^{\text{Wannier}} = \frac{1}{c\Omega} \operatorname{Im} \sum_{\boldsymbol{R}}^{\text{occ.}} \langle w_{n\boldsymbol{R}}| \Biggl\{ \sum_\beta \left[\frac{\partial}{\partial B_\alpha} A_\beta(\boldsymbol{r}) \right]_{\boldsymbol{B}=\boldsymbol{0}} \mathcal{QHQ}r_\beta
$$

$$
- \sum_\beta \mathcal{HP}r_\beta \mathcal{Q} \left[\frac{\partial}{\partial B_\alpha} A_\beta(\boldsymbol{r}) \right]_{\boldsymbol{B}=\boldsymbol{0}} - \mu \boldsymbol{r} \times \mathcal{Q}\boldsymbol{r} \Biggr\} |w_{n\boldsymbol{R}}\rangle, \tag{5.44}
$$

$$
m_{n,\alpha}^{\text{band}} = \frac{1}{c\Omega} \operatorname{Im} \sum_{\boldsymbol{R}}^{\text{occ.}} \langle w_{n\boldsymbol{R}}^{\text{H}}| \Biggl\{ \sum_\beta \left[\frac{\partial}{\partial B_\alpha} A_\beta(\boldsymbol{r}) \right]_{\boldsymbol{B}=\boldsymbol{0}} \mathcal{QHQ}r_\beta
$$

$$
- \sum_\beta \mathcal{HP}r_\beta \mathcal{Q} \left[\frac{\partial}{\partial B_\alpha} A_\beta(\boldsymbol{r}) \right]_{\boldsymbol{B}=\boldsymbol{0}} - \mu \boldsymbol{r} \times \mathcal{Q}\boldsymbol{r} \Biggr\} |w_{n\boldsymbol{R}}^{\text{H}}\rangle, \tag{5.45}
$$

$$
m_\alpha(\boldsymbol{r}) = \frac{1}{c\Omega} \operatorname{Im} \langle \boldsymbol{r}| \Biggl\{ \sum_\beta \mathcal{P} \left[\frac{\partial}{\partial B_\alpha} A_\beta(\boldsymbol{r}) \right]_{\boldsymbol{B}=\boldsymbol{0}} \mathcal{QHQ}r_\beta \mathcal{P}
$$

$$
- \sum_\beta \mathcal{PHP}r_\beta \mathcal{Q} \left[\frac{\partial}{\partial B_\alpha} A_\beta(\boldsymbol{r}) \right]_{\boldsymbol{B}=\boldsymbol{0}} \mathcal{P} - \mu \mathcal{P}\boldsymbol{r} \times \mathcal{Q}\boldsymbol{r}\mathcal{P} \Biggr\} |\boldsymbol{r}\rangle. \tag{5.46}
$$

If $\boldsymbol{A}(\boldsymbol{r})$ is gauge-transformed from the symmetric gauge to $\boldsymbol{B} \times \boldsymbol{r}/2 + \boldsymbol{\nabla}\chi(\boldsymbol{r})$, gauge-dependent terms emerge in addition to Eqs. (5.10b), (5.14b), and (5.22b). These

gauge-dependent terms are

$$
\begin{aligned}
m_{n,\alpha}^{\text{Wannier,gauge}} = \frac{1}{c\Omega} \operatorname{Im} \sum_{\boldsymbol{R}}^{\text{occ.}} \langle w_{n\boldsymbol{R}}| \Bigg\{ \sum_{\beta} \left[\frac{\partial}{\partial B_\alpha} \nabla_\beta \chi(\boldsymbol{r}) \right]_{\boldsymbol{B}=\boldsymbol{0}} \mathcal{Q}\mathcal{H}\mathcal{Q}r_\beta \\
- \sum_{\beta} \mathcal{H}\mathcal{P}r_\beta \mathcal{Q} \left[\frac{\partial}{\partial B_\alpha} \nabla_\beta \chi(\boldsymbol{r}) \right]_{\boldsymbol{B}=\boldsymbol{0}} \Bigg\} |w_{n\boldsymbol{R}}\rangle,
\end{aligned}
\tag{5.47}
$$

$$
\begin{aligned}
m_{n,\alpha}^{\text{band,gauge}} = \frac{1}{c\Omega} \operatorname{Im} \sum_{\boldsymbol{R}}^{\text{occ.}} \langle w_{n\boldsymbol{R}}^{\text{H}}| \Bigg\{ \sum_{\beta} \left[\frac{\partial}{\partial B_\alpha} \nabla_\beta \chi(\boldsymbol{r}) \right]_{\boldsymbol{B}=\boldsymbol{0}} \mathcal{Q}\mathcal{H}\mathcal{Q}r_\beta \\
- \sum_{\beta} \mathcal{H}\mathcal{P}r_\beta \mathcal{Q} \left[\frac{\partial}{\partial B_\alpha} \nabla_\beta \chi(\boldsymbol{r}) \right]_{\boldsymbol{B}=\boldsymbol{0}} \Bigg\} |w_{n\boldsymbol{R}}^{\text{H}}\rangle,
\end{aligned}
\tag{5.48}
$$

$$
\begin{aligned}
m_{\alpha}^{\text{gauge}}(\boldsymbol{r}) = \frac{1}{c\Omega} \operatorname{Im} \langle \boldsymbol{r}| \Bigg\{ \sum_{\beta} \mathcal{P} \left[\frac{\partial}{\partial B_\alpha} \nabla_\beta \chi(\boldsymbol{r}) \right]_{\boldsymbol{B}=\boldsymbol{0}} \mathcal{Q}\mathcal{H}\mathcal{Q}r_\beta \mathcal{P} \\
- \sum_{\beta} \mathcal{P}\mathcal{H}\mathcal{P}r_\beta \mathcal{Q} \left[\frac{\partial}{\partial B_\alpha} \nabla_\beta \chi(\boldsymbol{r}) \right]_{\boldsymbol{B}=\boldsymbol{0}} \mathcal{P} \Bigg\} |\boldsymbol{r}\rangle.
\end{aligned}
\tag{5.49}
$$

In the case that $\chi(\boldsymbol{r})$ is a first-order polynomial of $\boldsymbol{r}$, $\nabla\chi(\boldsymbol{r})$ does not depend on $\boldsymbol{r}$. Therefore, the gauge-dependent terms vanish because $\mathcal{Q}|w_{n\boldsymbol{R}}\rangle = 0$ and $\mathcal{P}\mathcal{Q} = 0$, and the decomposed orbital magnetizations are gauge-invariant in this case. In the case that $\chi(\boldsymbol{r})$ is a second-order polynomial of $\boldsymbol{r}$, $\nabla\chi(\boldsymbol{r})$ can be written as $\nabla\chi(\boldsymbol{r}) = S\boldsymbol{r} + \text{const.}$, where S is a symmetric matrix. Substituting this into Eq. (5.48), it is transformed as

$$
\begin{aligned}
m_{n,\alpha}^{\text{band,gauge}} &= \frac{1}{c\Omega} \operatorname{Im} \sum_{\boldsymbol{R}}^{\text{occ.}} \sum_{\beta} \left(\frac{\partial S_{\beta\gamma}}{\partial B_\alpha} \right)_{\boldsymbol{B}=\boldsymbol{0}} \langle w_{n\boldsymbol{R}}^{\text{H}}| \left(r_\gamma \mathcal{Q}\mathcal{H}\mathcal{Q}r_\beta - \mathcal{H}\mathcal{P}r_\beta \mathcal{Q}r_\gamma \right) |w_{n\boldsymbol{R}}^{\text{H}}\rangle \\
&= -\frac{1}{c\Omega} \operatorname{Im} \sum_{\boldsymbol{R}}^{\text{occ.}} \sum_{\beta} \left(\frac{\partial S_{\beta\gamma}}{\partial B_\alpha} \right)_{\boldsymbol{B}=\boldsymbol{0}} \langle w_{n\boldsymbol{R}}^{\text{H}}| \mathcal{H}\mathcal{P}r_\beta \mathcal{Q}r_\gamma |w_{n\boldsymbol{R}}^{\text{H}}\rangle \\
&= -\frac{1}{c\Omega} \operatorname{Im} \sum_{\beta} \left(\frac{\partial S_{\beta\gamma}}{\partial B_\alpha} \right)_{\boldsymbol{B}=\boldsymbol{0}} \frac{\Omega}{(2\pi)^3} \int_{\text{BZ}} d^3k \, \varepsilon_{n\boldsymbol{k}} \langle \widetilde{\partial}_{k_\beta} u_{n\boldsymbol{k}}| \widetilde{\partial}_{k_\gamma} u_{n\boldsymbol{k}}\rangle \\
&= 0.
\end{aligned}
\tag{5.50}
$$

Thus, the band-decomposed orbital magnetization is gauge-invariant in this case.

5.8 Numerical verification

In order to verify the computation in the presented method, we compare the sum of the decomposed isotropic shieldings with the experimental chemical shift for the hydrogen atoms in hydroxides and hydrides. The sum of the decomposed isotropic shieldings cannot be compared directly with the experimental chemical shift, because the macroscopic shape contribution of the shielding tensor is not evaluated within the converse

approach as mentioned in Sec. 2.3.2. Therefore, we firstly verify the correspondence between the experimental chemical shift and isotropic shielding with the macroscopic contribution calculated by the gauge-including projector augmented-wave (GIPAW) method [36], and afterward, we compare the sum of the decomposed isotropic shieldings and the isotropic shielding *without* the macroscopic contribution calculated by the GIPAW method. We implement the decomposition method on top of the converse-nmr code [55] which is developed based on the Quantum ESPRESSO code [56]. The total isotropic shielding is evaluated by the GIPAW method implemented in the Quantum ESPRESSO code. All the calculations are performed with the Perdew–Burke–Ernzerhof (PBE) functional [46] of the generalized gradient approximation (GGA) [24] and the norm-conserving pseudopotential [57, 58]. The cutoff energy and number of k-points are increased until the total isotropic shielding is converged within 0.1 ppm.

The relation between the experimental chemical shift and isotropic shielding with the macroscopic contribution calculated by the GIPAW method is depicted in Fig. 5.2a. The linear fitting for data in Fig. 5.2a other than BaH_2 gives

$$\delta_{\text{expt}} = -0.96\,\sigma_{\text{GIPAW}}^{\text{iso,w/ macro}} + 28.94\,\text{ppm} \tag{5.51}$$

with $R^2 = 0.92$ and the root mean square error of 0.56 ppm, where δ_{expt} is the experimental chemical shift and $\sigma_{\text{GIPAW}}^{\text{iso,w/ macro}}$ is the isotropic shielding with the macroscopic contribution calculated by the GIPAW method. The isotropic shielding calculated by the GIPAW method is in good agreement with the experimental chemical shift except for BaH_2. Then, we show the relation between the sum of the decomposed isotropic shieldings and isotropic shielding without the macroscopic contribution calculated by the GIPAW method in Fig. 5.2b. They are in excellent agreement, confirming the computation in the presented decomposition method.
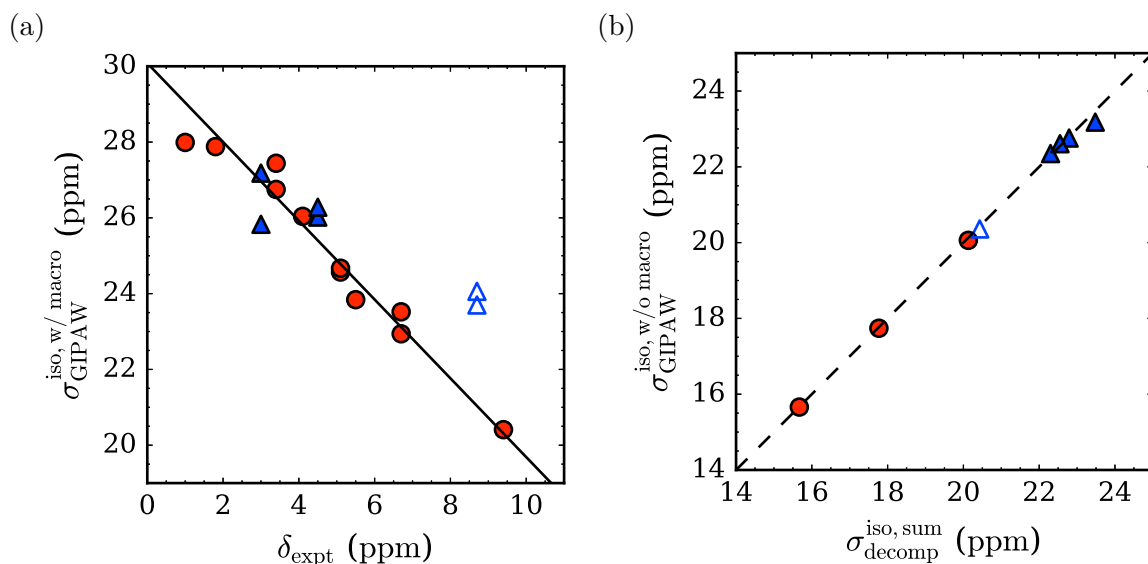
(a)

(b)

Figure 5.2: (a) Relation between the experimental chemical shift δ_{expt} and isotropic shielding with the macroscopic contribution calculated by the GIPAW method $\sigma_{\mathrm{GIPAW}}^{\mathrm{iso,w/\ macro}}$ for the hydrogen atoms in hydroxides and hydrides. The red circles are data for $Ca(OH)_2$, α-AlOOH, γ-Al(OH)$_3$, and δ-Al(OH)$_3$. The blue filled triangles are data for CaH_2, LiH, and β-MgH$_2$. The blue open triangles are data for BaH$_2$. The experimental chemical shifts are taken from Refs. 15–17,59. The solid line is obtained by the linear fitting for data other than BaH$_2$. (b) Relation between the sum of the decomposed isotropic shieldings $\sigma_{\mathrm{decomp}}^{\mathrm{iso,sum}}$ and isotropic shielding without the macroscopic contribution in the GIPAW method $\sigma_{\mathrm{GIPAW}}^{\mathrm{iso,w/o\ macro}}$ for the hydrogen atoms in hydroxides and hydrides. The dashed line denotes the exact match between them. The red circles are data for $Ca(OH)_2$, α-AlOOH, and two of the six inequivalent hydrogen atoms in γ-Al(OH)$_3$. The blue filled triangles are data for CaH_2, LiH, and β-MgH$_2$. The blue open triangle is data for one of the two inequivalent hydrogen atoms in BaH$_2$.

Chapter 6

Analysis of the shielding tensor by the decomposition

In this chapter, we apply the method of decomposing the shielding tensor introduced in the previous chapter to reveal microscopic mechanism of the shielding and clarify the difference between hydroxides and hydrides. Additionally, the dependence of the chemical shift on the atomic distance is investigated based on the speculation proposed from analysis of the decomposed shielding.

6.1   Computational details

We implement the methods of the decompositions on top of the converse-nmr code [55]. The converse-nmr code enables calculations of the shielding tensor in the converse approach, which is developed based on the Quantum ESPRESSO code [56]. For the Wannier decomposition, we use the maximally-localized Wannier function (MLWF) [60]. A set of unitary matrices transforming energy eigenstates into MLWFs is obtained by the wannier90 code [61].

The calculations are performed by using the PBE functional [46] of the generalized gradient approximation (GGA) and the norm-conserving pseudopotential [57, 58]. The cutoff energy and number of k-points are increased until the total isotropic shielding is converged within $0.1\,\mathrm{ppm}$.

In addition to calculations of the decomposed shielding tensors, we evaluate the shielding tensor corresponding to the macroscopic shape of the sample. It can be calculated through the gauge-including projector augmented-wave (GIPAW) method, and we carry out this as implemented in the Quantum ESPRESSO code.

6.2   Band, Wannier, and bunch decompositions

We confirm that the sum of the band-decomposed isotropic shieldings is in good agreement with the total isotropic shielding of the conventional calculation. However, the band-decomposed values are anomalously large compared to the total isotropic shielding. For instance, in $Ca(OH)_2$, the minimum and maximum value of the band-decomposed isotropic shieldings are -1042692.9 ppm and 1043264.0 ppm, respectively. Although some bands have contributions of extremely large magnitudes, these positive and negative contributions are compensated with each other, resulting in the total value of 21.2 ppm. These anomalous values of the band-decomposed isotropic shieldings is not suitable for analysis. We tried to solve the problem by using appropriate orbitals instead of energy eigenstates, namely, by the Wannier decomposition. Again, the sum of the Wannier-decomposed values is approximately the same as the total isotropic shielding of the conventional calculation. However, at least by the maximally-localized Wannier orbital, some decomposed isotropic shieldings are still in extremely large magnitude, which are between -2015040.1 ppm and 1510837.4 ppm for $Ca(OH)_2$. Therefore, the Wannier decomposition by the MLWF is also useless.

The extremely large contributions arising in the band and Wannier decompositions are due to the gauge freedom for a set of orbitals discussed in Sec. 5.3 and are suppressed when summed within the respective bunches of bands separated energetically. For $Ca(OH)_2$, there are five bunch of bands in the valence state, and the contributions of them are 3.9 ppm, 17.0 ppm, 2.3 ppm, -2.0 ppm, and 0.0 ppm in order from the highest bunch in the energy. The second highest bunch in the energy, which has the largest contribution, is characterized by O $2p$ and H $1s$ states. Although it is reasonable that the largest contribution relates to the hydrogen state, it cannot be determined whether the hydrogen state gives a primary contribution, because the bunch with the largest contribution is formed by the hybridization of the oxygen and hydrogen states. For CaH_2, the decomposed isotropic shieldings are 26.5 ppm, -4.1 ppm, and -0.1 ppm in order from the highest bunch in the energy. The bunch giving the largest contribution is the hybridized state similarly to $Ca(OH)_2$, which is characterized by Ca $3d$ and H $1s$ states. Although further analysis is difficult for the bunch decomposition, it can be claimed that the hydrogen state is at least related to the bunch giving the largest contribution.

6.3   Spatial decomposition

Next we move on to the spatial decomposition, which is free from the problem of selecting appropriate gauge for the Wannier decomposition. We define the cumulative

radial isotropic shielding for analysis as

$$\sigma_{\mathrm{cum,H}}^{\mathrm{iso}}(r) = \frac{1}{\Omega} \int_{|\boldsymbol{r}' - \boldsymbol{r}_{\mathrm{H}}| < r} d^3 r' \, \sigma^{\mathrm{iso}}(\boldsymbol{r}'), \tag{6.1}$$

where Ω is the volume of the supercell and $\boldsymbol{r}_{\mathrm{H}}$ is the position of the hydrogen atom at which the magnetic dipole moment is located. In Fig. 6.1, the cumulative radial isotropic shieldings are shown for various sizes of the supercell. The total isotropic shieldings, which are the values at the rightmost point of each plotted line, scarcely depend on the size of the supercell. Although the radial distribution varies with respect to the size of the supercell, its maximum point converges.

The difference between the maximum value and the total value represents the macroscopic effect of the sample, namely, the deshielding by the demagnetizing field. In principle, the magnetic dipole moment at the hydrogen atom feels only the external magnetic field. However, if we cut out the system around the magnetic dipole moment within some radius, the demagnetizing field is induced by the boundary of the cut-out region. Therefore, the magnetic dipole moment feels both the external magnetic field and demagnetizing field, resulting in the shielding including the macroscopic effect. If the cut-out region is enlarged up to the size of the supercell, the boundaries of the cut-out regions in the periodic cells touch each other, and the demagnetizing field is canceled out. Finally, at the farthest distance, the macroscopic effect completely disappears, resulting in the shielding without the macroscopic effect. The difference of the cumulative radial isotropic shieldings between the maximum point and the farthest point are 7.2 ppm, 9.5 ppm, 3.0 ppm, and 3.9 ppm for the largest supercells of $Ca(OH)_2$, α-AlOOH, CaH_2, and LiH, respectively. They actually correspond to the isotropic shieldings by the macroscopic effect of 7.5 ppm, 10.2 ppm, 3.7 ppm, and 4.0 ppm for $Ca(OH)_2$, α-AlOOH, CaH_2, and LiH, respectively. This point allows us to focus on the region inside the maximum point in further analysis.

Hereafter, we show the results for the largest supercells. The distribution of the spatially decomposed isotropic shieldings exhibits a qualitative difference between hydroxides and hydrides as shown in Fig. 6.2. In hydrides CaH_2 and LiH, the shielding is large around the hydrogen atom, while in hydroxides $Ca(OH)_2$ and α-AlOOH, the shielding is large around the oxygen atom nearest to the hydrogen atom. Additionally, in α-AlOOH, the deshielding region emerges in the second nearest oxygen atom O2. This difference can be clearly seen in the cumulative radial isotropic shieldings decomposed into atomic contributions, Fig. 6.3. In hydrides, the shielding is dominated by the contribution around the hydrogen atom with the magnetic dipole moment, which agrees with the conventional view that the chemical shift reflects the electronic charge state of the hydrogen atom. Therefore, the shielding is expected to become strong for shorter hydrogen-hydrogen distance, in other words, for shorter metal-hydrogen
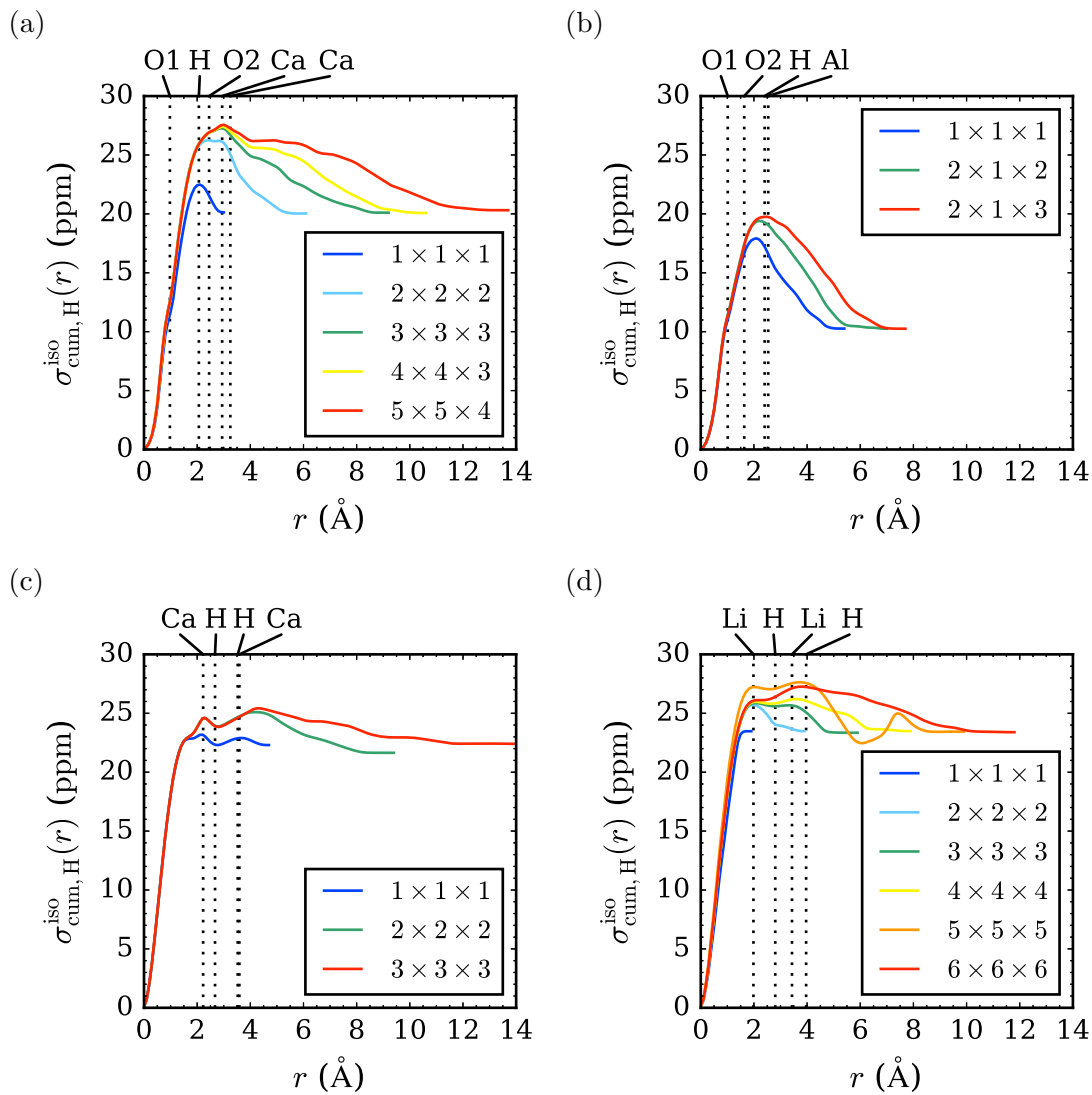
Figure 6.1: Cumulative radial isotropic shieldings for various sizes of the supercell of (a) Ca(OH)$_2$, (b) α-AlOOH, (c) CaH$_2$, and (d) LiH. The values are plotted in every 0.1 Å.
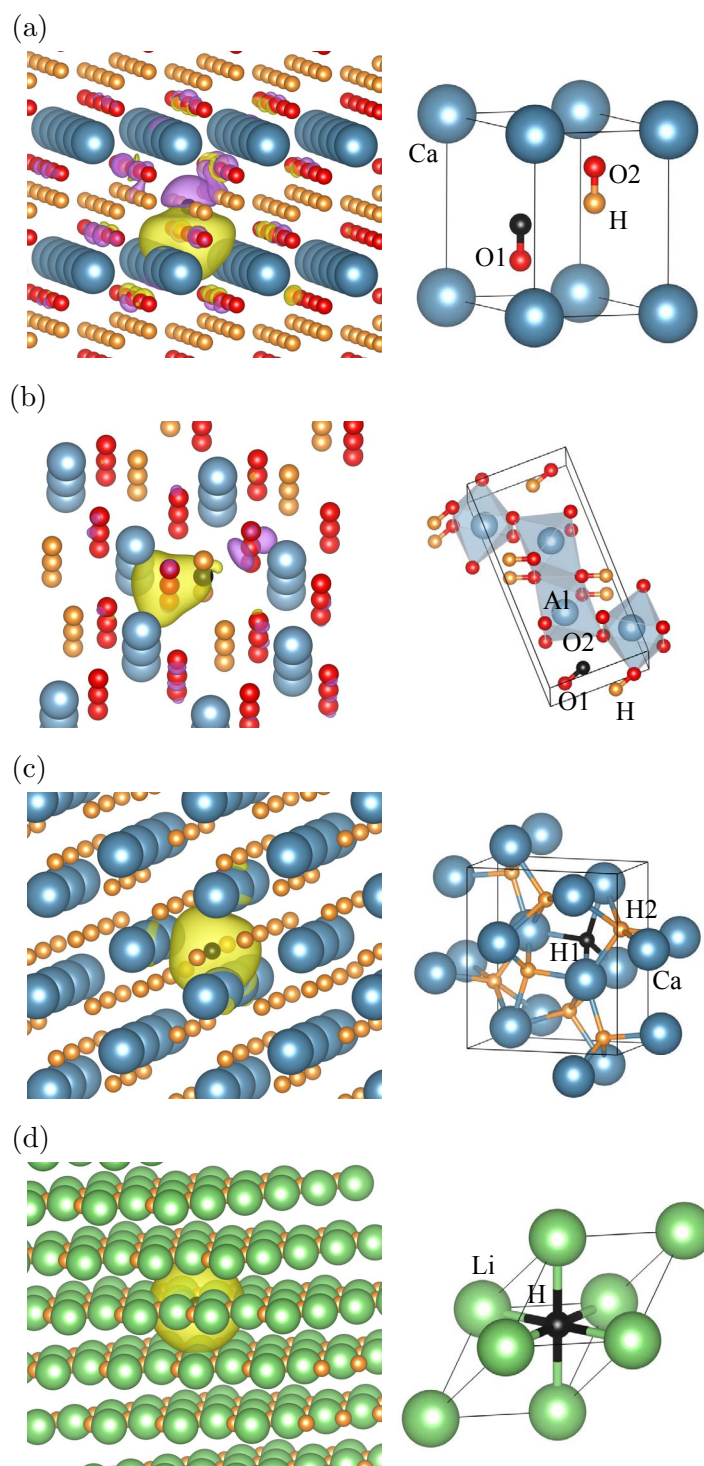
Figure 6.2: Spatially decomposed isotropic shieldings $\sigma^{\mathrm{iso}}(\boldsymbol{r})$ for (a) Ca(OH)$_2$, (b) α-AlOOH, (c) CaH$_2$, and (d) LiH. The black atom denotes the hydrogen atom at which the magnetic dipole moment is located. The yellow and purple isosurfaces correspond to $+500\,\mathrm{ppm}$ and $-500\,\mathrm{ppm}$, respectively. In (c) and (d), the values of $\sigma^{\mathrm{iso}}(\boldsymbol{r})$ at $1.6\,\text{Å}$ and $1.7\,\text{Å}$ from the target hydrogen atoms, respectively, are approximately $+500\,\mathrm{ppm}$.

57
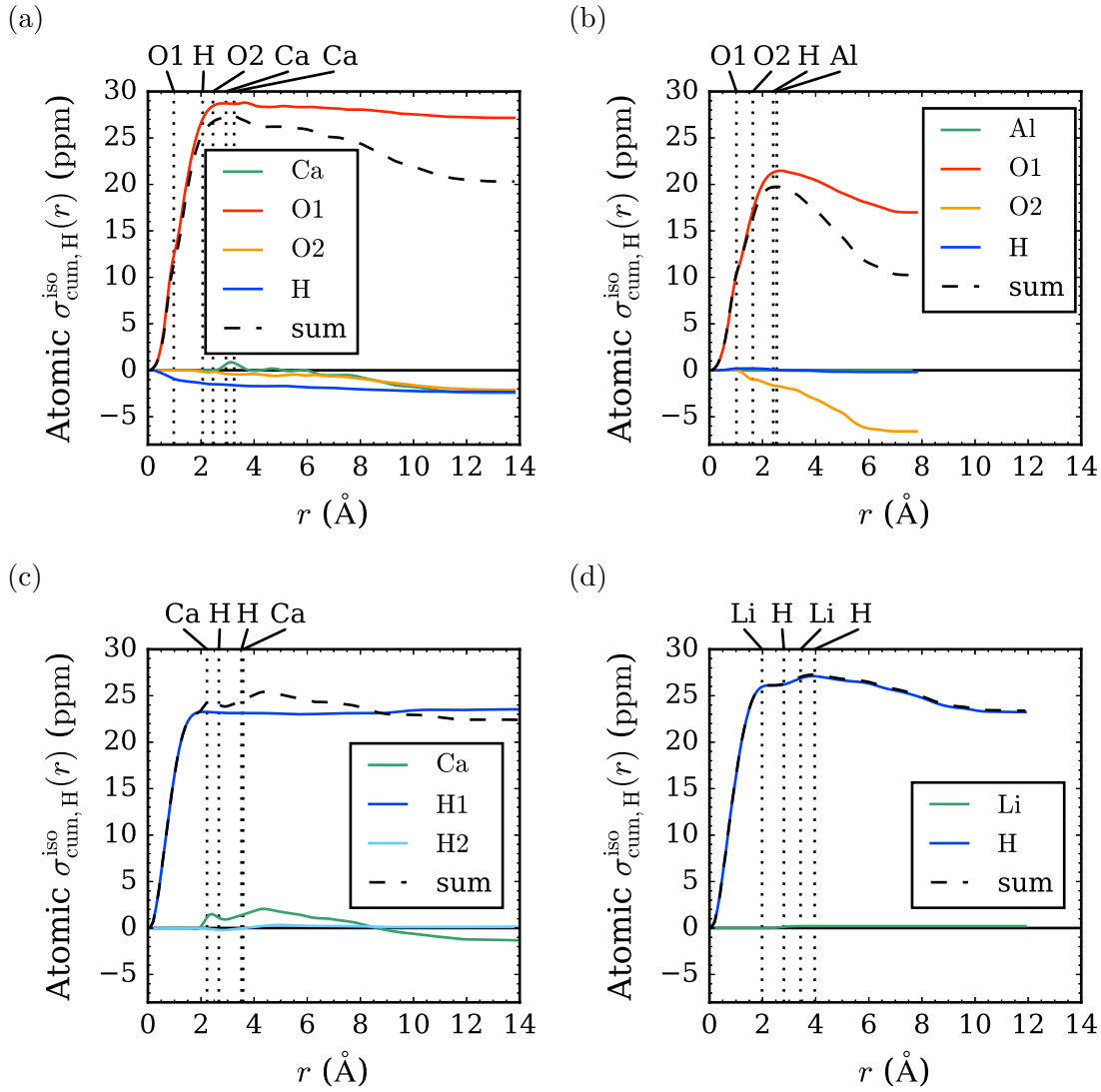
Figure 6.3: Cumulative radial isotropic shieldings decomposed into atomic contributions for (a) $Ca(OH)_2$, (b) α-AlOOH, (c) CaH_2, and (d) LiH.

distance. In contrast, the primary contribution in hydroxides comes from around the nearest oxygen atom, which suggests that the chemical shifts for these hydroxides do not reflect the state of the hydrogen atom directly. Thus, the shielding is expected to be affected by the distance between the nearest oxygen atom and hydrogen atom $d(O-H)$. Furthermore, since the secondary contribution is given by the second nearest oxygen atom in α-AlOOH, the distance between the first and second nearest oxygen atom $d(O\cdots O)$ is also expected to affect the shielding. Considering the positive contribution from the nearest oxygen atom and negative contribution from the second nearest oxygen atom, short $d(O-H)$ and long $d(O\cdots O)$ are thought to yield strong shielding.
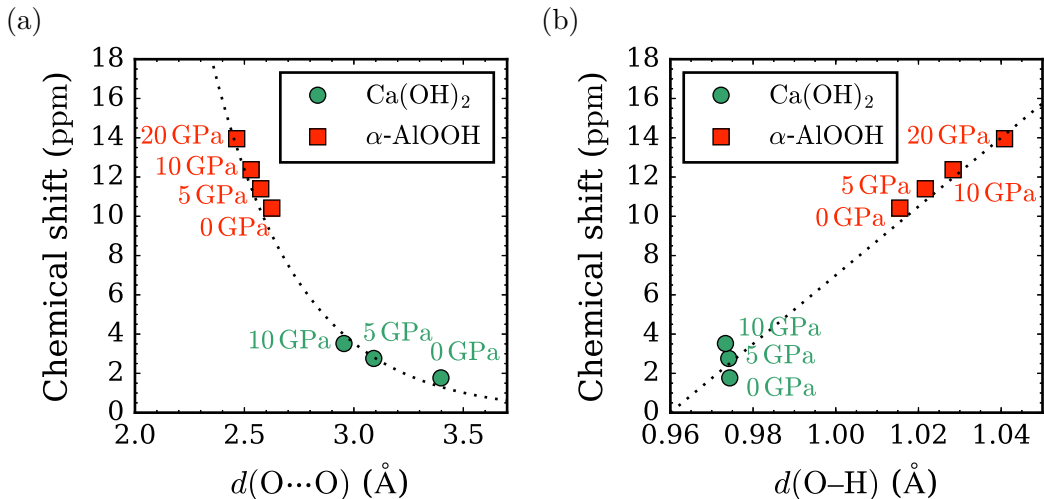
Figure 6.4: The chemical shift for pressured hydroxides with respect to (a) the distance between the first and second nearest oxygen atoms and (b) the O−H bond length. The dotted lines are guides for the eyes.

6.4 Dependence on the atomic distance

In order to verify the speculation about the atomic distance dependence for hydroxides proposed in the previous section, we vary the atomic distance for $Ca(OH)_2$ and α-AlOOH by applying the pressure. The chemical shift with respect to the distance between the first and second nearest oxygen atom $d(O\cdots O)$ and between the nearest oxygen atom and hydrogen atom $d(O-H)$ is shown in Fig. 6.4. As expected from the spatial decomposition, the chemical shift is smaller (the shielding is stronger) for longer $d(O\cdots O)$ and for shorter $d(O-H)$. Remarkably, these trends are accidentally consistent with the previous study [21] in which the charge density at the hydrogen site was thought to be the origin of the shielding. Note that the microscopic origin of the shielding is the oxygen electronic state, according to our calculation.

For the hydrides, the larger chemical shift is assumed for the longer metal-hydrogen distance $d(M-H)$. This relation is suggested as an empirical linear correlation [21], and has been verified for LiH [21]. However, for CaH_2, the chemical shift scarcely depends on the Ca−H distance as shown in Fig. 6.5. Although the correlation for LiH is explained by the Coulomb repulsion between electrons of the hydrogen atom and surrounding electrons, the pressure dependence for CaH_2 implies that other factors should be also relevant.
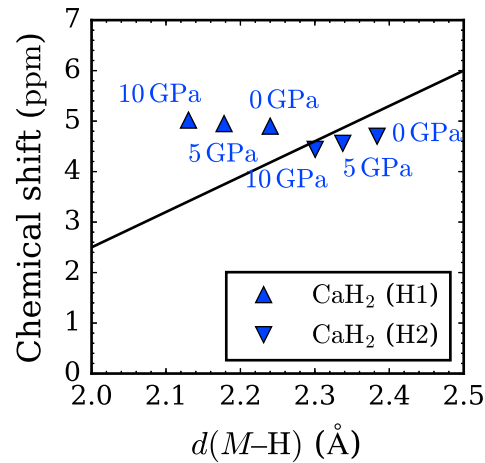
Figure 6.5: The chemical shift for pressured CaH_2 with respect to the distance between the metallic atom (Ca) and the hydrogen atom. The black line denotes the empirical linear correlation in Ref. 21.

6.5 Discussion

For hydroxides, we found that the shielding is dominated by the electronic states around nearby oxygen atoms, which renews the conventional view on the relation between the shielding and electronic state around the target hydrogen atom. For hydrides, we confirm the conventional view that the shielding reflects the hydrogen charge state. On the other hand, we found that the material dependence of shielding is not well explained by the simple scenario related to the distance to the nearest metallic atom.

Chapter 7

Application to $KTiO_2H$

The analysis in the previous chapter has revealed the general importance of the electronic states of atoms around the target hydrogen atom. Since oxyhydride $KTiO_2H$ contains both the oxygen anion and the hydrogen anion, it is not clear whether the hydrogen shielding for $KTiO_2H$ behaves like hydroxides containing the oxygen anion or hydrides containing the hydrogen anion. Actually, we evaluated the chemical shift for $KTiO_2H$ as 2.3 ppm, surprisingly, which is positive like the chemical shifts of H^+. In this chapter, we apply the analysis presented in the previous chapter to $KTiO_2H$; namely, the analysis by the spatial decomposition of the shielding tensor and its pressure dependence.

7.1 Spatial decomposition

The cumulative radial isotropic shieldings for various sizes of the supercell are shown in Fig. 7.1. The total isotropic shielding does not depend on the size of the supercell, and the maximum point is almost converged. The isotropic shielding by the macroscopic effect is estimated to be 1.0 ppm for the $3 \times 3 \times 2$ supercell, which corresponds to that of 1.1 ppm calculated by a part of the gauge-including projector augmented-wave (GIPAW) method.

   The distribution of the isotropic shielding for the $3 \times 3 \times 2$ supercell is depicted in Fig. 7.2. While the shielding is large around the hydrogen atom, the neighboring titanium atoms also have sizable contribution. The atomic contributions of the cumulative radial isotropic shielding in Fig. 7.3 shows the primary contribution from the hydrogen atom and the secondary contribution from the titanium atoms. It is the same as the typical hydrides that the hydrogen atom exhibits largest contribution. On the other hands, it is different from hydroxides that the contribution of the nearest oxygen atom (O_{ip}) is almost zero. On this point, the chemical shift for $KTiO_2H$ is basically similar
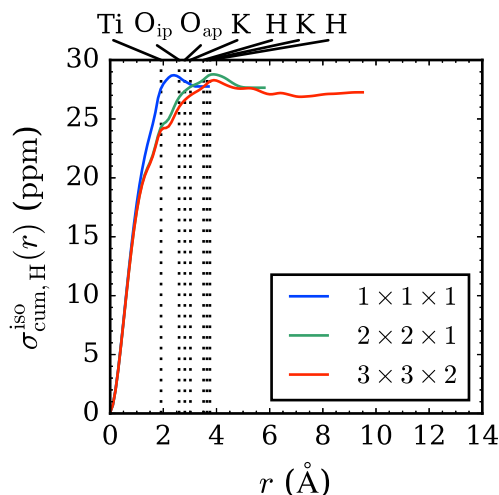
Figure 7.1: Cumulative radial isotropic shieldings for various sizes of the supercell of KTiO$_2$H. The values are plotted in every 0.1 Å.

to that for the typical hydrides.

7.2 Pressure dependence

Since the cumulative radial isotropic shielding exhibits the similar feature to that for hydrides, the chemical shift for KTiO$_2$H might be correlated with the Ti−H distance. As in the previous chapter, we apply the pressure to evaluate the relation between the chemical shift and the atomic distance. The chemical shift with respect to the Ti−H distance is shown in Fig. 7.4. The chemical shift become small as the Ti−H distance is shortened, which is the same tendency as the empirical correlation proposed in Ref. 21 or the case of LiH. Meanwhile, the slope of the linear relation for KTiO$_2$H is larger than that for the empirical correlation. This large slope probably originates from the electronic states around the titanium atoms, which has the secondarily large positive shielding as shown in Fig. 7.2.

7.3 Summary of the atomic contributions

We summarize the atomic contributions for the hydroxides, typical hydrides, and oxyhydride in Table 7.1.
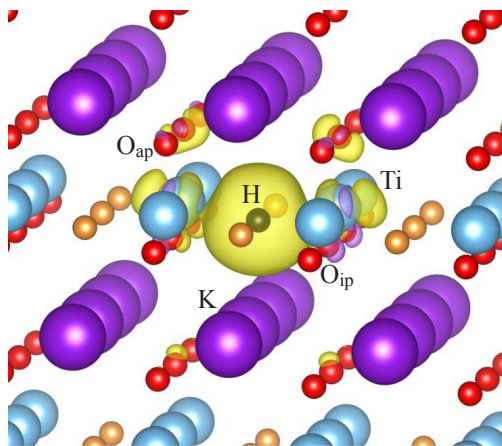
Figure 7.2: Spatially decomposed isotropic shieldings for KTiO$_2$H. The black atom denotes the hydrogen atom at which the magnetic dipole moment is located. The yellow and purple isosurfaces correspond to $+500$ ppm and -500 ppm, respectively.
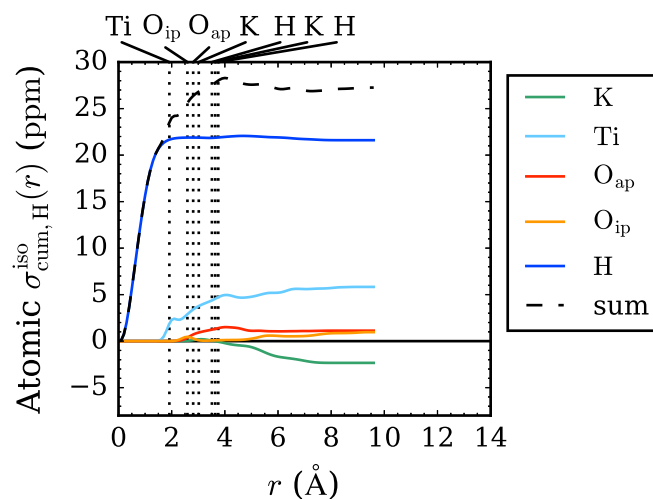

Figure 7.3: Cumulative radial isotropic shieldings decomposed into atomic contributions for KTiO$_2$H.
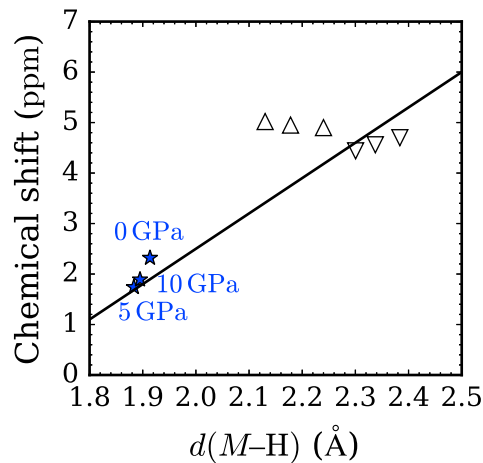
Figure 7.4:   The chemical shift for pressured KTiO$_2$H with respect to the distance between the metal atom (Ti) and the hydrogen atom. The black line denotes the empirical linear correlation in Ref. 21. The open triangles are data for pressured CaH$_2$ plotted in Fig. 6.5. The distance under 10 GPa is shorter than that under 5 GPa because the c-axis is much shortened under 10 GPa and the crystal structure becomes close to a cubic structure.

Table 7.1: Atoms exhibiting a large shielding contribution.

		target hydrogen atom	metallic atom	oxygen atom nerest	oxygen atom next-nearest
Hydroxides	Ca(OH)$_2$			✓	
	α-AlOOH			✓	✓
Metallic hydrides	MH$_x$	✓		−	−
Oxyhydride	KTiO$_2$H	✓	✓		

64

Chapter 8

Conclusion

In this thesis, we have investigated a series of unsynthesized perovskite-type oxyhydrides $A\mathrm{TiO_2H}$ ($A = \mathrm{Li}$, Na, K, Rb, Cs) and their novel electronic structures and dielectric/piezoelectric properties by using density functional calculations. To seek for the way to confirm the synthesis of the predicted oxyhydrides, we have also studied the $^1\mathrm{H}$ nuclear magnetic resonance (NMR) shielding in the representative system $\mathrm{KTiO_2H}$. For this purpose, we have developed a microscopic theory on the shielding and numerical scheme on top of it.

In Chap. 3, the crystal structure, energetic stability, and electronic structure have been investigated for $\mathrm{KTiO_2H}$. It is crystallized in the orthorhombic structure which is stretched in the c-axis, and the titanium atom is 5-fold coordinated. The formation energies are evaluated for three possible synthesis reactions, resulting in the negative values, namely, it is energetically stable. As for the electronic structure, $\mathrm{KTiO_2H}$ exhibits the two-dimensional electronic state at the valence band maximum. The two-dimensional state has been revealed to be an antibonding state formed by in-plane oxygen $2p$ orbital and hydrogen $1s$ orbital. From a comparison with the electronic structure for $\mathrm{KTiO_2F}$, the origin of the emergent two-dimensional state at the valence top is low electron affinity of the hydrogen atom compared with the halogen atoms. Due to the symmetry of the $1s$ orbital, this state appears along the Y–T k-point path in the orthorhombic Brillouin zone.

In Chap. 4, the A-site dependence of $A\mathrm{TiO_2H}$ ($A = \mathrm{Li}$, Na, K, Rb, Cs) is investigated. For $A = \mathrm{Rb}$, Cs, energetic stabilities are verified from formation energies, while formation energies become positive in some reactions for $A = \mathrm{Li}$, Na. It implies the difficulty of synthesis for $A = \mathrm{Li}$, Na. The crystal structures for $A = \mathrm{Li}$, Na, Rb, Cs are similar to that for $A = \mathrm{K}$, and vary with respect to the ionic radii of the A-site atom. The two-dimensional electronic state exhibits at the valence band maximum also in these oxyhydrides, although the two-dimensional character is weakened as $A = \mathrm{Cs}$ to

Li. This trend can be originated in the length of the c-axis. Additionally, the Born effective charge tensors, spontaneous electric polarizations, static dielectric tensors, and piezoelectric tensors are evaluated for $A =$ Li, Na, K, Rb, Cs. The variation of these properties with respect to the A-site atoms are typically explained by the variation in the crystal structures and electronic structures, hence the ionic radii of the A-site atoms.

In Chap. 5, we pursued possible microscopic description of the shielding by decomposing the shielding tensor in various ways. The chemical shift in ^{1}H NMR is thought to reflect the charge state of the hydrogen atoms in the compounds. In the previously discovered oxyhydrides, however, the ^{1}H NMR chemical shift shows counterintuitive behavior, which motivates us to examination of the NMR shielding phenomenon in the perovskite oxyhydride. The fundamental difficulty for microscopic formulation of the shielding tensor is the ill-defined character of the "microscopic" orbital magnetization. We have proposed five ways of decompositions: namely, decompositions into contributions of (i) the Wannier orbitals, (ii) energy bands, (iii) bunches of bands, (iv) spatial regions, and (v) atoms. We have extensively discussed the origins of the indeterminacy in the respective decompositions and proved that the major problems are overcome with the spatially decomposed formulation. On top of this, we have implemented a first-principles scheme to calculate the spatially decomposed shielding contribution, as well as the Bader analysis method for that. The relations of our formulations to the modern theory of orbital magnetization has also been discussed.

In Chap. 6, we have analyzed the decomposed shielding tensors in typical hydrides and hydroxides to establish the general picture on the microscopic shielding phenomenon in prior to the study on the oxyhydride. Although the band- and Wannier-decomposed isotropic shieldings suffer from the anomalous values originating from the orbital-gauge dependence, the bunch decomposition suggests appreciable contribution from the target hydrogen state, which is in accord with the conventional view. However, with the spatial decomposition scheme, we have found that view is actually inapplicable straightforwardly. For hydrides, the shielding is dominated by the contribution around the target hydrogen atom, which is consistent with the conventional view. On the other hand, in hydroxides, the primary contribution comes from the neighboring oxygen atoms, not around the target hydrogen atom: The electronic states around the nearest oxygen atom yields large positive contributions, whereas those around the second-nearest oxygen atoms in the hydrogen-bonded system α-AlOOH give appreciable negative contribution. From the atomic contributions in hydroxides, the chemical shift is expected to increase as the distance between first and second nearest oxygen atoms decreases and the distance between the nearest oxygen atom and hydrogen atom increases, which is verified by applying the pressure. We have found that these trends are accidentally consistent with the correlation suggested in Ref. 21 based on the

conventional view, although the origin is different from that proposed from our calculation. For hydrides, however, the correlation between the shielding and the interatomic distances are not as simple as anticipated from the above result.

Finally, in Chap. 7, the analysis established in the previous chapter is applied to $KTiO_2H$. The cumulative radial isotropic shielding for $KTiO_2H$ reveals that the primary contribution is from the target hydrogen atom, which is the same feature as the above-mentioned hydrides. Meanwhile, the titanium atoms also exhibit sizable positive contribution to the shielding. The pressure dependence shows that the chemical shift increases with respect to stretching of the Ti−H distance more drastically than expected from the empirical linear correlation proposed previously. This difference from the typical hydrides probably originates from the contribution of the titanium atoms. We have thus revealed the peculiar features of the ^{1}H NMR shielding in the perovskite oxyhydride.

The study of oxyhydrides is not yet a long-standing research field, especially for the perovskite-type structure. In the situation that new oxyhydrides are synthesizing, it is helpful to predict the crystal structure and electronic properties for oxyhydrides by first-principles calculations. An interesting future issue in the study of $ATiO_2H$ is applications of the two-dimensional electronic state. The realization of superconductivity is one of possibilities. If hole doping is available for these oxyhydrides, the two-dimensional state should contribute to superconductivity. Since the two-dimensional state has the hydrogen $1s$ character, it is expected to realize high-temperature superconductivity based on the Bardeen–Cooper–Schrieffer (BCS) theory [62].

An important remaining issue is how to distinguish the charge state of the hydrogen atoms in the compounds of multiple kinds of ions with the ^{1}H NMR. Our newly developed theory and method on the spatial decomposition of the shielding tensor establishes a basis for analyzing microscopic origins of the shielding. Although only the radial distribution of the isotropic shielding has been studied in this thesis, more detailed analyses are also possible, such as an angular decomposition and xyz-component analysis of the shielding tensor. By applying them to various types of compounds, the causal relation between the shielding and the charge states under the influence of the surrounding crystal potential will be further understood in the future.

Appendix A

Computational costs of the decomposed shielding tensors

The calculations of the decomposed shielding tensors are performed with the generalized gradient approximation (GGA) functional parameterized by Perdew–Burke–Ernzerhof (PBE) and the norm-conserving pseudopotential as mentioned in Chap. 6. The valence electrons of the pseudopotentials are $1s^1$ for H, $2s^1$ for Li, $2s^22p^4$ for O, $3s^23p^1$ for Al, $3s^23p^64s^1$ for K, $3s^23p^64s^2$ for Ca, and $3s^23p^64s^23d^2$ for Ti. The calculations are performed with cutoff energies of $84\,\mathrm{Ry}$ for $Ca(OH)_2$, $76\,\mathrm{Ry}$ for α-AlOOH, $60\,\mathrm{Ry}$ for CaH_2, $76\,\mathrm{Ry}$ for LiH, and $268\,\mathrm{Ry}$ for $KTiO_2H$. The Γ-centered k-point grid is employed for all the calculations. For the unit cells, used k-point grids are a $6 \times 6 \times 4$ grid for $Ca(OH)_2$, a $6 \times 3 \times 9$ grid for α-AlOOH, a $4 \times 6 \times 3$ grid for CaH_2, a $8 \times 8 \times 8$ grid for LiH, and a $16 \times 15 \times 10$ grid for $KTiO_2H$. For the supercells, the k-point spacings corresponding to those for the unit cells are employed.

Within our implementation, the orbital magnetization matrix in Eq. (5.28) is calculated firstly, and afterward, the band-decomposed and spatially decomposed orbital magnetizations are evaluated from the orbital magnetization matrix simultaneously. Additionally, six independent computations of the decomposed orbital magnetizations are necessary to evaluate one decomposed shielding tensor, namely, the computations for the magnetic dipole moments $\boldsymbol{m}_s$ directing $\pm x$, $\pm y$, and $\pm z$. The number of cores and required times for computations of the orbital magnetization matrices and decomposed orbital magnetizations are listed in Table. A.1. The evaluation of the decomposed shielding tensor from the decomposed orbital magnetizations takes only a few minutes by using one core.

Table A.1: Number of cores and required time to calculate the orbital magnetization matrix and the decomposed orbital magnetizations. All the cores participate in the Message Passing Interface (MPI) parallelization unless otherwise noted.

	cell	orbital magnetization matrix		decomposed orbital magnetization	
		cores	time (hour)	cores	time (hour)
$Ca(OH)_2$	$1 \times 1 \times 1$	16	0.06	16	0.01
	$2 \times 2 \times 2$	16	1.76	16^*	0.15
	$3 \times 3 \times 3$	96	0.54	24	0.24
	$4 \times 4 \times 3$	96	2.39	96	0.28
	$5 \times 5 \times 4$	96	4.63	384	0.32
α-AlOOH	$1 \times 1 \times 1$	16	0.13	16	0.02
	$2 \times 1 \times 2$	16	0.81	16	0.07
	$2 \times 1 \times 3$	16	1.60	16	0.28
CaH_2	$1 \times 1 \times 1$	16	0.15	16	0.01
	$2 \times 2 \times 2$	16	1.77	16	0.28
	$3 \times 3 \times 3$	96	5.73	24	2.66
LiH	$1 \times 1 \times 1$	16	0.10	16	0.08
	$2 \times 2 \times 2$	16	0.06	16	0.01
	$3 \times 3 \times 3$	16	0.30	16	0.02
	$4 \times 4 \times 4$	16	1.30	16	0.07
	$5 \times 5 \times 5$	16	9.55	16	0.71
	$6 \times 6 \times 6$	16	52.71	16	3.13
$KTiO_2H$	$1 \times 1 \times 1$	24	3.16	24	0.10
	$2 \times 2 \times 1$	16	124.00	16	7.70
	$3 \times 3 \times 2$	48	86.56	96	15.28

* OpenMP parallelization.

Bibliography

[1] V. M. Goldschmidt. *Die Naturwissenschaften*, 14:477, 1926.

[2] U. Müller. In *Inorganic Structural Chemistry*, page 203. John Wiley & Sons, Ltd, New York, 2006.

[3] Y. I. Kim, P. M. Woodward, K. Z. Baba-Kishi, and C. W. Tai. *Chem. Mater.*, 16:1267, 2004.

[4] B. L. Chamberland. *Mater. Res. Bull.*, 6:311, 1971.

[5] T. Katsumata, H. Umemoto, Y. Inaguma, D. Fu, and M. Itoh. *J. Appl. Phys.*, 104:044101, 2008.

[6] T. Katusmata, M. Nakashima, H. Umemoto, and Y. Inaguma. *J. Solid State Chem.*, 181:2737, 2008.

[7] Y. Akishige. *Ferroelectrics*, 369:91, 2008.

[8] Y. Kobayashi, O. J. Hernandez, T. Sakaguchi, T. Yajima, T. Roisnel, Y. Tsujimoto, M. Morita, Y. Noda, Y. Mogami, A. Kitada, M. Ohkura, S. Hosokawa, Z. Li, K. Hayashi, Y. Kusano, J. eun Kim, N. Tsuji, A. Fujiwara, Y. Matsushita, K. Yoshimura, K. Takegoshi, M. Inoue, M. Takano, and H. Kageyama. *Nature Mater.*, 11:507, 2012.

[9] T. Yajima, A. Kitada, Y. Kobayashi, T. Sakaguchi, G. Bouilly, S. Kasahara, T. Terashima, M. Takano, and H. Kageyama. *J. Am. Chem. Soc*, 134:8782, 2012.

[10] F. D. Romero, A. Leach, J. S. Möller, F. Foronda, S. J. Blundell, and M. A. Hayward. *Angew. Chem.*, 126:7686, 2014.

[11] C. Tassel, Y. Goto, Y. Kuno, J. Hester, M. Green, Y. Kobayashi, and H. Kageyama. *Angew. Chem. Int. Ed.*, 53:10377, 2014.

[12] M. A. Hayward, E. J. Cussen, J. B. Claridge, M. Bieringer, M. J. Rosseinsky, C. J. Kiely, S. J. Blundell, I. M. Marshall, and F. L. Pratt. *Science*, 295:1882, 2002.

[13] C. A. Bridges, G. R. Darling, M. A. Hayward, and M. J. Rosseinsky. *J. Am. Chem. Soc.*, 127:5996, 2005.

[14] S. Iimura, S. Matsuishi, H. Sato, T. Hanna, Y. Muraba, S. W. Kim, J. E. Kim, M. Takata, and H. Hosono. *Nature Commun.*, 3:943, 2012.

[15] X. Xue and M. Kanzaki. *J. Am. Ceram. Soc.*, 92:2803, 2009.

[16] A. T. Nicol and R. W. Vaughan. *J. Chem. Phys.*, 69:5211, 1978.

[17] Jr. R. C. Bowman, S.-J. Hwang, C. C. Ahn, and J. J. Vajo. *MRS Proc.*, 837:N3.6, 2004.

[18] M. J. Evans, G. P. Holland, F. J. Garcia-Garcia, and U. Häussermann. *J. Am. Chem. Soc.*, 130:12139, 2008.

[19] J. Clayden, N. Greeves, and S. Warren. In *Organic Chemistry*, chapter 13. Oxford University Press, Oxford, 2 edition, 2012.

[20] H. Eckert, J. P. Yesinowski, L. A. Silver, and E. M. Stolper. *J. Phys. Chem.*, 92:2055, 1988.

[21] K. Hayashi, P. V. Sushko, Y. Hashimoto, A. L. Shluger, and H. Hosono. *Nature Commun.*, 5:3515, 2014.

[22] P. Hohenberg and W. Kohn. *Phys. Rev.*, 136:B864, 1964.

[23] W. Kohn and L. J. Sham. *Phys. Rev.*, 140:A1133, 1965.

[24] J. P. Perdew. *Phys. Rev. Lett.*, 55:1665, 1985.

[25] P. E. Blöchl. *Phys. Rev. B*, 50:17953, 1994.

[26] G. Kresse and D. Joubert. *Phys. Rev. B*, 59:1758, 1999.

[27] R. D. King-Smith and D. Vanderbilt. *Phys. Rev. B*, 47:1651, 1993.

[28] X. Gonze and C. Lee. *Phys. Rev. B*, 55:10355, 1997.

[29] X. Wu, D. Vanderbilt, and D. R. Hamann. *Phys. Rev. B*, 72:035105, 2005.

[30] A. D. Corso, M. Posternak, R. Resta, and A. Baldereschi. *Phys. Rev. B*, 50:10715, 1994.

[31] D. Xiao, J. Shi, and Q. Niu. *Phys. Rev. Lett.*, 95:137204, 2005.

[32] T. Thonhauser, D. Ceresoli, D. Vanderbilt, and R. Resta. *Phys. Rev. Lett.*, 95:137205, 2005.

[33] D. Ceresoli, T. Thonhauser, D. Vanderbilt, and R. Resta. *Phys. Rev. B*, 74:024408, 2006.

[34] J. Shi, G. Vignale, D. Xiao, and Q. Niu. *Phys. Rev. Lett.*, 99:197202, 2007.

[35] R. Bianco and R. Resta. *Phys. Rev. Lett.*, 110:087202, 2013.

[36] C. J. Pickard and F. Mauri. *Phys. Rev. B*, 63:245101, 2001.

[37] D. Skachkov, M. Krykunov, E. Kadantsev, and T. Ziegler. *J. Chem. Theory Comput.*, 6:1650, 2010.

[38] R. Laskowski and P. Blaha. *Phys. Rev. B*, 85:035132, 2012.

[39] T. Thonhauser, D. Ceresoli, A. A. Mostofi, N. Marzari, R. Resta, and D. Vanderbilt. *J. Chem. Phys.*, 131:101101, 2009.

[40] D. Ceresoli, N. Marzari, M. G. Lopez, and T. Thonhauser. *Phys. Rev. B*, 81:184424, 2010.

[41] F. Vasconcelos, G. A. de Wijs, R. W. A. Havenith, M. Marsman, and G. Kresse. *J. Chem. Phys.*, 139:014109, 2013.

[42] N. Sato and S. Tsuneyuki. *Appl. Phys. Lett.*, 109:172903, 2016.

[43] R. D. Shannon. *Acta. Cryst.*, A32:751, 1976.

[44] G. Kresse and J. Hafner. *Phys. Rev. B*, 47:558, 1993.

[45] G. Kresse and J. Furthmüller. *Phys. Rev. B*, 54:11169, 1996.

[46] J. P. Perdew, K. Burke, and M. Ernzerhof. *Phys. Rev. Lett.*, 77:3865, 1996.

[47] K. Ikeda, T. Sato, and S. Orimo. *Int. J. Mat. Res.*, 99:471, 2008.

[48] S. Piskunov, E. Heifets, R. I. Eglitis, and G. Borstel. *Comput. Mater. Sci.*, 29:165, 2004.

[49] H. Moriwake, C. A. J. Fisher, A. Kuwabara, and T. Hashimoto. *Jpn. J. Appl. Phys.*, 50:09NE02, 2011.

[50] X. Meng, X. Wen, and G. Qin. *Comput. Mater. Sci.*, 49:S372, 2010.

[51] N. F. Ramsey. *Phys. Rev.*, 78:699, 1950.

[52] R. Bianco and R. Resta. *Phys. Rev. B*, 93:174417, 2016.

[53] R. F. W. Bader. *Acc. Chem. Res.*, 18:9, 1985.

[54] P. Středa. *J. Phys. C: Solid State Phys.*, 15:L717, 1982.

[55] `http://code.google.com/archive/p/converse-nmr`.

[56] P. Giannozzi, S. Baroni, N. Bonini, M. Calandra, R. Car, C. Cavazzoni, D. Ceresoli, G. L. Chiarotti, M. Cococcioni, I Dabo, A. Dal Corso, S. de Gironcoli, S. Fabris, G. Fratesi, R. Gebauer, U. Gerstmann, C. Gougoussis, A. Kokalj, M. Lazzeri, L. Martin-Samos, N. Marzari, F. Mauri, R. Mazzarello, S. Paolini, A. Pasquarello, L. Paulatto, C. Sbraccia, S. Scandolo, G. Sclauzero, A. P. Seitsonen, A. Smogunov, P. Umari, and R. M. Wentzcovitch. *J. Phys.: Condens. Matter*, 21:395502, 2009.

[57] N. Troullier and J. L. Martins. *Phys. Rev. B*, 43:1993, 1991.

[58] Pseudopotentials are taken from `http://sites.google.com/site/dceresoli/pseudopotentials` except for Ti.

[59] P. C. M. M. Magusin, W. P. Kalisvaart, P. H. L. Notten, and R. A. van Santen. *Chem. Phys. Lett.*, 456:55, 2008.

[60] N. Marzari and D. Vanderbilt. *Phys. Rev. B*, 56:12847, 1997.

[61] A. A. Mostofi, J. R. Yates, G. Pizzi, Y.-S. Lee, I. Souza, D. Vanderbilt, and N. Marzari. *Comput. Phys. Commun.*, 185:2309, 2014.

[62] J. Bardeen, L. N. Cooper, and J. R. Schrieffer. *Phys. Rev.*, 108:1175, 1957.